Materials Advances

ROYAL SOCIETY OF CHEMISTRY

REVIEW

View Article Online
View Journal | View Issue

Cite this: *Mater. Adv.*, 2022, 3, 7773

Hydroxyapatite coatings: a critical review on electrodeposition parametric variations influencing crystal facet orientation towards enhanced electrochemical sensing

Priya Ranjan Dev, [a] Chekkottu Parambil Anand, †[ab] David Samuvel Michael †[a] and P. Wilson *[a]

Electrochemical deposition presents a promising route toward the fabrication of hydroxyapatite (HAp) coatings attributed to its simplistic approach in the preparation of coatings over complex substrates with control over coating thickness and crystal orientation through variations in electrodeposition parameters. This article aims to consolidate and review the influence of reported parametric determinants associated with electrodeposition thereby providing insight into the outcome of HAp microstructures in terms of Ca/P ratio, crystal growth, and facet orientation of the HAp hexagonal crystal system. Additionally, a discussion on HAp and its composites as viable sensor materials for a myriad of aqueous-based analytes and gaseous molecules is presented. A survey into the application of HAp as a sensor is elaborated, emphasizing the level of sensitivity, selectivity, and sensor response characteristics regarding optimum performance at maximum % sensitivity. Mechanistic insights into the interaction of HAp with analyte species are discussed. Finally, the parameters that include both current density and pH are correlated to determine their synergistic effect as a deciding factor in the growth and preferential orientation of aligned hexagonal HAp crystal domains.

Received 1st June 2022,
Accepted 1st September 2022

DOI: 10.1039/d2ma00620k

rsc.li/materials-advances

[a] *Department of Chemistry, Madras Christian College (Autonomous), University of Madras, Chennai-600 059, India. E-mail: wilson@mcc.edu.in*
[b] *NMR Research Unit, University of Oulu, Oulu-90014, Finland*
† Equal contributing authors.

Priya Ranjan Dev

Priya Ranjan Dev has completed his Masters in Chemistry and Bachelors in Education and is currently pursuing PhD at Madras Christian College, India. He has worked as a research fellow under the SERB-EMR project funded by DST, India (2016–2019). His research interests include the experimental synthesis of metal oxide based microstructures, their functionalization and the determination of the role of defects towards applications relating to energy materials, sensors, photocatalysis, and electrochemical applications. His research interests further extend to DFT studies and materials modelling.

Chekkottu Parambil Anand

Chekkottu Parambil Anand is presently a first year doctoral student at the NMR Research Unit of University of Oulu, Finland. He completed graduation from the University of Eastern Finland in 2020 and undergraduate degree from Madras Christian College, India, in 2018, both majoring in Chemistry. Currently he is interested in conducting theoretical and quantum-chemical studies on organometallic complexes of lanthanide and actinide ions which can be constructed as potential Single Molecular Magnets (SMM). This makes it possible to code information into individual molecules and has possible applications in quantum information processing.

1. Introduction

Hydroxyapatite (HAp), a biomaterial composed of hydroxylated calcium phosphate ($Ca_{10}(PO_4)_6(OH)_2$), is an extensively studied calcium phosphate polymorph whose excellent biocompatibility finds predominant application in bone cement, implants with antibacterial properties,[1,2] as well as in the fields of drug delivery[3,4] and catalytic applications.[5] Additionally, HAp exhibits ferro, pyro, and piezoelectric properties with practical application in bone regeneration and growth and as an immunosensor.[6–8] Extensive applicatory studies have been carried out concerning its inherent physical and chemical properties. The versatility of HAp is mainly due to the possibilities arising from the modification of stoichiometric composition as a result of substitution of Ca^{2+} with divalent cations and replacement of the PO_4^{3-} anionic tetrahedron and the OH^- group with carbonate and halide anions. As a standalone material, HAp micro and macrostructures are inherently brittle with low orders of tensile strength making them impractical in load-bearing applications. Furthermore, they are incapable of exhibiting long-range electric properties. To mitigate these mechanical and electrical restrictions, HAp is generally coupled as a composite with metallic and metal oxide substrates of Ti, Mg, and carbon-based composites to act as a backbone of sorts in enhancing its mechanical properties[9] and in providing a point of electrical contact and conduction. Nanocomposite coatings are considered an effective strategy in the fabrication of heterogeneous materials[10,11] resulting in improvement in physico-chemical properties,[12–18] mitigating detrimental degradation,[19–21] and in enhancing its applicative aspects towards increased efficacy,[22–25] in reinforcement,[26–29] and sustainability.[30]

The fabrication of these nanocomposites offers a certain degree of flexibility in their respective field of application. Among both wet and dry preparatory methods, HAp-based composites are preferably fabricated *via* the thermal spray deposition technique owing to its convenient industrial scalability.[31,32] However, this technique does not necessarily yield robust HAp/metal coated biocomposites as the applied thermal effects result in the formation of cracks, defects, and mixed phases over the superficial macrostructure. This may result in increased susceptibility towards varying rates of biocorrosion. Other techniques include sol–gel[33,34] and hydrothermal[35,36] processes with each technique entailing its limitations concerning scalability, tunability of coating characteristics, and phase purity. However, the technique of electrochemical deposition presents a viable possibility of adjustment of coating thickness with control over the degree of crystallinity, grain size, and morphology. Additionally, electrochemical deposition offers growth on complex shaped substrates with relative ease and topographical uniformity.[37] Furthermore, the coating characteristics can be modified by alteration of deposition parameters such as current density, applied potential, loading time, electrolytic pH, presence of additives, and external treatments like ultrasonication among many other factors. These variations significantly reflect in

David Samuvel Michael

David Samuvel Michael completed his graduate studies in Chemistry from Madras Christian College, India, in 2021. His research interests include computational chemistry and quantum mechanics. Presently he is working in the field of theoretical spectroscopy and fundamental quantum mechanics to understand electronic spectroscopy using TDDFT calculations and basic quantum mechanical models.

P. Wilson

P. Wilson received his PhD from Indian Institute of Technology, Madras, in 2000 and later worked as a postdoctoral fellow at Ben-Gurion University of the Negev in 2003. He worked as a lecturer in chemistry in Hindustan University, Chennai (1992–93), Bishop Heber College, Trichy (1993–94), and St. Joseph's College of Engineering, Chennai (2000–2002) prior to serving as an associate professor (2004–2015) and head (2015–2020) of Department of Chemistry, Madras Christian College, India. He currently serves as the Principal and Secretary, Madras Christian College. He has supervised research projects funded under DST, India, UGC, India and UBCHEA, USA. Moreover, he is a member of various research and academic bodies. His research publications and interests encompass the fabrication of biomaterials and metal oxide microstructural nanocomposites and their application in fields relating to photocatalysis towards water splitting and dye degradation, coating and corrosion science, biosensors, gas sensors and energy materials. Additionally, he has authored book chapters and continues to serve as a reviewer in ACS, Elsevier and Springer publications. He continues to publish in esteemed international publications.

coating microstructure, porosity, and adhesion to the substrate.[38] It is well known that control over crystal orientation influences the applicability of the material. This specificity in HAp crystal orientation may be a deciding factor in enhancing selectivity towards ionic and neutral species. Therefore, optimization of parametric variations encompassing electrochemical deposition and controlling preferentiality in HAp crystal orientation can lead to enhancement in properties.

Relevant HAp reviews have been published discussing the myriad synthetic and coating routes,[9,39,40] and the fabrication of deformable ultralong HAp nanowires,[41] along the line of application in the biomedical[42–44] and pharmaceutical fields,[4] and in the adsorptive removal of lead[45] and dyes.[46] Additionally, comprehensive reviews have been reported on adhesion quality towards bio-metallic substrates,[47] electrical nature of HAp,[48–50] heterogeneous organocatalytic aspects of HAp with emphasis on stability and reusability,[51] and specifically on cationic, anionic, and multi-ionic substitutions of the lattice atoms of HAp.[52] In the field of electrodeposition, a general review of electrodeposited biocoatings[53] and a review focusing on the influence of applied current have been reported.[54] However, there has not been any comprehensive publication exploring the myriad of driving and assisting electrochemical deposition parameters influencing nucleation and crystal orientation with a specific applicative focus on the influence of hexagonal HAp crystal systems towards sensing of various electrolytic and gaseous species.

This review aims to consolidate and disseminate the technique of electrochemical deposition of HAp with a focus on the classification of deposition parameters that determine and influence the dynamics of HAp coating performance reported in line with this preparatory route. This review will strive to hopefully enable any newcomer to grasp the nuances involved in the fabrication of specifically tuned HAp crystals *via* parametric modification during electrochemical deposition. Therefore, this review will begin firstly by elucidating the crystal facets of HAp to comprehend the significance of the surface properties of each facet. Secondly, a discussion entailing the effects of all significantly reported parametric modifications on nucleation, crystal growth, and microstructure of HAp coatings is presented. Next, a survey into the application of HAp and its composites towards electrochemical sensing is discussed emphasizing the level of sensitivity and selectivity of the crystal towards the sensing of gaseous and electrolytic species. Finally, a correlation between applied current density and pH is discussed, modeling the possible microstructural outcomes of HAp electrodeposits *via* variations of these two electrolytic parameters.

2. Crystal structure of HAp

The potency of HAp in fields such as ion exchange resin, drug/protein carriers, catalysts, and sensing can be related to the anisotropic properties exhibited by the crystal. HAp exists in two crystalline structures: monoclinic and hexagonal. Monoclinic HAp is thermodynamically stable in relation to the

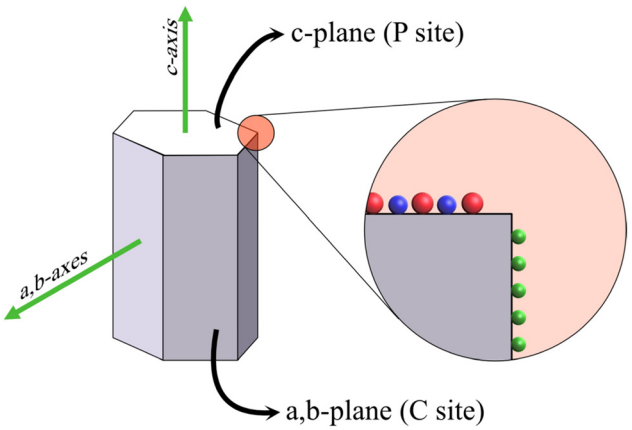

Fig. 1 Schematic illustration of the hexagonal HAp crystal system with the PO_4^{3-} and OH^- groups (in red and blue respectively) occupying the *c*-plane and Ca^{2+} (green sphere) populating the *a*,*b*-plane.

hexagonal system wherein the major difference between the two lies in the orientation of the columnar hydroxyl groups present within the crystal lattice.[55] The hexagonal crystal system, illustrated in Fig. 1, belongs to the $P6_3/m$ space group while maintaining a stoichiometric Ca/P ratio at 1.67. The framework of hexagonal HAp conforms to two crystal facets: the *a*,*b*-plane and *c*-plane.[56] The *c*-plane (or P site) exposes both PO_4^{3-} and OH^- ions predominantly whereas a higher density of surface Ca^{2+} occupies the *a*,*b*-plane (or C site). Consequently, a net negative charge on the *c*-plane and a net positive charge on the *a*,*b*-plane persist due to the system being anionically and cationically richer respectively.[57] This enables the system to exhibit anisotropic properties due to its differently charged facets making HAp an ideal candidate for the aforementioned applications. For instance, the possibility of exchange of Ca^{2+} and PO_4^{3-} lattice ions makes HAp a versatile material for the selective removal of anionic and cationic species from the external environment.[58] The proper utilization of this aspect can be related to the controlled growth of crystals along a specific orientation. The key to bringing out the efficacy of the hexagonal crystal system lies in controlling growth along either the *c*-plane or *a*,*b*-plane, which may be witnessed in terms of the overall Ca/P ratio and microstructural variations. The increase in exposed surface area of a target plane maximizes the capability of the crystal towards adsorption and exchange of ionic species.

The *a*,*b*-plane and *c*-plane can be matched with the XRD peak profile of phase-pure HAp. The diffraction peak identified at $\sim 26^\circ$ belongs to the (002) plane, *i.e.*, the *c*-plane.[59] The peaks profiled at 21.8° and 32.9° correspond to the (200) and (300) planes respectively, *i.e.*, the *a*,*b*-plane.[60] When the nucleation and growth predominate along the *a*,*b*-axis, the resultant microstructure is flake-like, whereas crystal growth along the *c*-axis witnesses the formation of hexagonal rods and acicular fibers. Additionally, during electrochemical deposition, the directional growth of crystals is generally perpendicular to the electrode surface. However, the variation in deposition parameters may better align the growth orientation either along the *a*,*b*-axes or

along the *c*-axis as the predominantly exposed facet that can be typically identified from the XRD profiles.

3. Electrochemical deposition of HAp

3.1. Deposition techniques of HAp coatings

The control of microstructure, coating thickness and nucleation rate of HAp can be related to the migration and ionic concentration of Ca^{2+}, PO_4^{3-} and OH^- near the vicinity of the cathode, which is dependent on the applied potential and current density over the working electrode. HAp can be electrochemically deposited *via* electrocathodic and electrophoretic deposition techniques. Both techniques can be performed in a two- or three-electrode electrolytic cell. The substrates employed in both electrochemical techniques are generally conductive metals and alloys, with a few exceptions like bioglass and conductive glass.[61,62] Electrocathodic deposition is a popular coating technique comprising ionic species as the electrolyte, wherein fabrication of multi-component and multi-layered coatings can be achieved. Conversely, electrophoretic deposition is mainly a colloidal approach to electrodeposition as it involves employing non-dissociable electrolytic species, such as polymers[61] and dispersed HAp nanoparticulate powders in the form of suspended colloids.

Electrophoresis boasts of its capability as a technique with a high deposition rate, producing coating thickness ranging from 0.1 to 2.0 mm.[63] Electrophoretic deposition emphasizes employing high voltages with very short deposition time. Additional factors influencing coating characteristics under electrophoretic deposition are suspension related factors such as particle size distribution, suspension viscosity and particle charging.[64] To minimize viscosity effects, HAp powders are usually dispersed in organic solvents such as ethanol, isopropanol or LiCl-organic electrolytic HAp suspensions.[64–66] Furthermore, the dispersed particles must remain in a colloidal suspension comprised of a liquid medium with an effective dielectric constant. Based on a relative comparison between isopropyl alcohol and ethanol, an effective electrophoretic efficiency was witnessed in the case of ethanol. Additionally, a high charge to mass ratio favors rapid deposition.[67] The difference between electrocathodic and electrophoretic deposition is that the latter employs a low ionic strength solvent whereas the former employs a solution of ionic salts with high ionic strength. Additionally, electrophoretic deposition requires high electric fields to facilitate the migration of low ionic strength species from the bulk towards the electrode surface.

Irrespective of the technique employed, the coatings fabricated *via* both techniques are predetermined by a common primary set of deposition parameters such as current, potential, pH, loading time, and deposition temperature. The dissemination within this review will focus on elucidating the parameters reported under electrocathodic deposition, hereafter termed electrodeposition, and their effects on the growth and morphological outcome of HAp crystals along either the *a*,*b*-axes or *c*-axis.

3.2. Electrolytic cell setup and mode of fabrication

3.2.1. Two-electrode and three-electrode setup. As a prerequisite, the electrolytic cell setup can be assumed to be a technical determinant, wherein electrodeposition of HAp can be carried out in either a two-electrode or a three-electrode electrochemical cell setup.[68] During electrodeposition, the cathodic surface charge changes with the accumulation of new nucleation and growth sites. The accumulation of HAp tends to passivate the cathode thereby altering the overall potential or charge density on the exposed surface of the working electrode. As a result, in the two-electrode setup, the cumulative charge density over the working electrode deviates as the coated layer increases in thickness.[69,70] This charge variation, if not maintained, may result in a lowered deposition rate over increased loading time. Although the applied potential and current are maintained between the anode and cathode *via* a regulated power supply, the internal electrochemical conditions may not be maintained throughout as a consequence of the passivating effect of the HAp coating. However, in the case of a three-electrode setup, the applied potential or current density is maintained with respect to the reference electrode thereby mitigating the drawbacks posed by the two-electrode system. The reference electrode utilized is selected on the basis of pH and electrolytic composition employed during electrodeposition.

3.2.2. Potentiostatic and galvanostatic mode. Electrodeposition of HAp can be carried out under either potentiostatic or galvanostatic mode by maintaining constancy in either applied potential or applied current respectively.[71,72] D. J. Blackwood *et al.*[73] performed galvanostatic pulse electrodeposition of HAp onto the Ti metal in a $CaCl_2$ and $NH_4H_2PO_4$ electrolyte at a current density of -0.75 and -6.50 mA cm^{-2}. It was observed that a higher current density resulted in a coating that was thicker but with poor uniformity and low adhesion strength. In addition, upon employing a lower current density, it was possible to achieve a majority crystal growth orientation along the (002) plane. Irrespective of the mode, the electrochemical mechanism encompassing HAp deposition and growth is similar to the mechanism elaborated by Ting-Ting Li *et al.*[54]

4. Mechanism of electrodeposition of HAp

The evolution of the phases of calcium phosphate is mainly driven by cathodic pH, primarily depending on the concentration of liberated OH^- ions.[74,75] The formation of $H_2PO_4^-$, HPO_4^{2-} and PO_4^{3-} is dependent on the relative evolution of OH^- ions. As a result, the concentration of OH^- dictates the distribution of phosphate species near the cathode, thus influencing the phase transformation of the deposited polymorph and can be expressed as

$$10Ca^{2+} + 6PO_4^{3-} + 2OH^- \rightarrow Ca_{10}(PO_4)_6(OH)_2 \text{ (HAp phase)} \quad (1)$$

$$4Ca^{2+} + HPO_4^{2-} + 2PO_4^{3-} \rightarrow Ca_4H(PO_4)_3 \text{ (OCP phase)} \quad (2)$$

$$Ca^{2+} + HPO_4^{2-} + 2H_2O \rightarrow CaHPO_4{\cdot}2H_2O \text{ (DCDP phase)} \quad (3)$$

The formation of HAp (eqn (1)) requires the presence of PO_4^{3-} and OH^- ions. A decrease in either of the anionic species will shift the phase towards OCP and DCDP (eqn (2) and (3)).

Consequently, the rate of electrolytic dissociation of H_2O and generation of OH^- and H^+ dictate the cathodic pH and ultimately the concentration of PO_4^{3-} near the cathode. Each type of calcium phosphate differs in its Ca/P ratio. Alina Vladescu *et al.* deposited HAp under potentiodynamic conditions wherein a potential sweep from −1.4 V to 0 V was applied with a constant sweep rate of 0.2 mV s^{-1}.[76] This study reports on the solubility of calcium phosphate which, being pH dependent, forms the basis of electrodeposition of HAp on conducting substrates under cathodic polarization. The several electrochemical reactions governing OH^- formation and the subsequent increase in alkalinity near a Ti cathode are

$$O_2 + 2H_2O + 4e^- \rightarrow 4(OH)^-_{ads} \quad (4)$$

$$2H^+ + 2e^- \rightarrow H_2 \quad (5)$$

$$2H_2O + 2e^- \rightarrow H_2 + 2(OH)^-_{ads} \quad (6)$$

$$2TiO_2 + 2H_2O + e^- \rightarrow Ti(OH)_3 + (OH)^-_{ads} \quad (7)$$

$$H_2PO_4^- + H_2O + 2e^- \rightarrow H_2PO_3^- + 2(OH)^-_{ads} \quad (8)$$

If higher concentrations of Ca^{2+} ions exist near the working electrode, then precipitation occurs and the recombination of PO_4^{3-} with H^+ (forming HPO_4^{2-}) would not take place. HAp, being soluble in relation to DCDP and OCP, was deposited as a plate-like microstructure at pH 5. However, increasing the pH to 6 witnessed needle-like deposits.[76]

5. Parameters concerning electrochemical deposition of HAp

This section of the review involves the dissemination of electrodeposition parameters reported to control the nucleation rate, crystal growth, orientation of crystal facets and coating characteristics of HAp composites. The various reported electrochemical parameters were classified on the basis of driving and assisting parameters. Driving parameters encompass those factors that initiate HAp formation and influence the rate of nucleation while assisting parameters are segregated based on their influence towards tuning and enhancing the coating characteristics upon their introduction to the electrolytic system. The myriad of parameters reported in relation to HAp electrodeposition and their classification can be seen depicted in Fig. 2.

5.1. Driving parameters

5.1.1. Influence of deposition potential. Applied potential is an important parameter in any electrochemical reaction involving alteration of surface activation and passivation and microstructural modulation. The effect of applied potential modes, *i.e.* potentiostatic or potentiodynamic, on orientation and phase purity of electrocrystallized HAp will be detailed with experimental parameters of select reports tabulated in Table 1.

5.1.1.1. Potentiostatic electrodeposition. T. Mokabber *et al.* investigated a two-electrode approach to electrodeposit HAp wherein a potentiostatic voltage between −1.8 V and −1.4 V was applied with loading times of 1, 2, 3, 5, and 30 min.[71] At an applied potential of −1.4 V, a uniform dense coating with a plate-like morphology is observed while deposition at −1.6 V and −1.8 V resulted in the coating to suffer deterioration with a significant amount of cracks and pore formation due to increased H_2 evolution. It was also determined that at −1.4 V, variation in loading time significantly brought about changes in crystal growth. For a deposition period of 1 to 3 min, the crystal nucleation dominated along the (010) and (030) planes indicating the initial growth being favored along the *a*,*b*-plane resulting in a flake- and plate-like microstructure. However, increased time resulted in the predominance of the acicular morphology with the XRD profile revealing increased intensity for the (002) *c*-plane.

Conversely, a three-electrode potentiostatic mode reported in ref. 77 addresses the growth and electrocrystallization of HAp in dilute solutions under experimental potentials ranging from −1.4 V to −2.2 V. At a lower potential of −1.4 V, it was observed that the coating predominantly comprised of OCP. A higher applied potential of −1.6 V, −1.8 V, −2.0 V, and −2.2 V favors the conversion of OCP to HAp. The XRD profile indicated the preferential crystal growth along the (002) plane with increasing applied potential. Additionally, SEM revealed the formation of vertically oriented hexagonal crystals with the progress in deposition time (shown in Fig. 3). At −1.8 V, an initial deposition time of 10 min resulted in the formation of

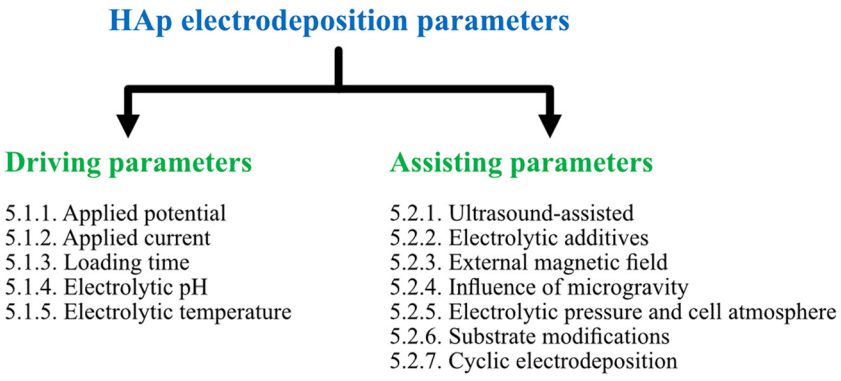

Fig. 2 Classification of various applied parameters, as driving and assisting parameters, reported under the technique of electrodeposition of HAp.

Table 1 Influence of applied potential on the HAp microstructure

S. No.	Cathode	Electrolyte	Potential (V)	Loading time (min)	pH	Temp (°C)	Ca/P ratio	Comments	Ref.
1	Ti	0.042 M $Ca(NO_3)_2$ + 0.025 M $NH_4H_2PO_4$ + 0.1–1.5 wt% H_2O_2	−1.4, −1.6, −1.8	1, 2, 3, 5, 30	4.3	65	1.67	Two-electrode potentiostatic mode	71
2	CoNiCrMo alloy	0.06 mM $Ca(NO_3)_2$ + 0.36 mM $NH_4H_2PO_4$ + 0.1 M $NaNO_3$	−1.4, −1.6, −1.8	10, 20, 60	6.0	80	1.67	Three-electrode configuration	77
3	Ti	0.167 M $CaCl_2$ + 0.1 M $NH_4H_2PO_4$	−1.5	30	6.0	80	—	Needle-like HAp of varying sizes	68
4	Ti_6Al_4V rod	0.61 mM $Ca(NO_3)_2$ + 0.38 mM $NH_4H_2PO_4$	−1.4	120	—	85	1.67	Plate-like HAp using three-electrode setup	253
5	Ti mesh	0.167 M $CaCl_2$ + 0.1 M $NH_4H_2PO_4$ + 0.1 M NaCl	−0.8 −1.5	30	6.0	80	1.57 2.54	Flower-like acicular HAp	254
6	TiN/316L SS	0.03 M $Ca(NO_3)_2$ + 0.018 M $NH_4H_2PO_4$ + 0.15 M $NaNO_3$ + 0–6% H_2O_2	−1.5 to −1.8	30, 45, 60, 75, 90	4.0–5.5	25, 40, 50, 60, 70, 80	—	Change from flakes to spherical particles with applied potential	91
7	Ti_6Al_4V alloy	$Ca(NO_3)_2$ + $NH_4H_2PO_4$	−1.4 to 0 (scan rate = 0.2 mV s^{-1})	120	5.0 and 6.0	75	1.32 @ pH 5, 1.51 @ pH 6	Potentiodynamic electrodeposition. Flakes (pH 5) and needle-like HAp (pH 6)	76
8	Ti_6Al_4V alloy	0.08 mol L^{-1} $Ca(NO_3)_2$ + 0.05 mol L^{-1} K_2HPO_4	2.5, 3.5, 4.5, 5.5	5–45	4.6	67	—	Phase change with variation in applied potential	255
9	Ti disc	0.875–3.5 mM $Ca(NO_3)_2$ + 0.5–2.1 mM $(NH_4)_2HPO_4$	−1.5	60	8.3–8.4	80	1.67	Three-electrode three-step potentiostatic mode	79

flake-like crystals, whereas after 20 min, the microstructure was rod-like (Fig. 3a and b). The initially formed flakes, closest to the substrate, were denser with interspersed pores due to the effects of H_2 bubble formation. Additionally, at the onset of deposition, the nucleation of HAp is horizontal (*i.e.* lateral) to the substrate. An increase in loading time witnessed that the nucleation and growth predominated along the direction perpendicular to the substrate resulting in the gradual formation of hexagonal rods. Furthermore, it was noted that the coatings electrodeposited at −1.8 V displayed enhanced adhesion to the substrate when subjected to sonofragmentation.[78]

A comparative analysis of the potentiostatic mode of electrodeposition of HAp under the two-electrode and three-electrode configuration can be made from ref. 71 and 77 respectively. In a two-electrode arrangement, the maximum working potential for uniform dense growth of HAp was reported as −1.4 V. An increase in applied potential above −1.5 V resulted in the generation of H_2 gas bubbles leading to severely cracked coating with larger pores. Conversely, the three-electrode potentiostatic mode facilitated a maximum working potential of −1.8 V beyond which the coating stability deteriorates. In terms of crystal growth and orientation, the three-electrode arrangement yields hexagonal crystals at −1.8 V (shown in Fig. 3c).

5.1.1.2. Three-step potentiostatic electrodeposition. B.-O. Taranu *et al.* investigated a three-step potentiostatic HAp electrodeposition strategy wherein the procedure comprises the creation of an initial deposit of HAp, followed by a second step of thermal calcination and then completion by performing an additional electrodeposition onto the HAp crystals deposited in the first step.[79] The process was performed under a three-electrode potentiostatic mode at −1.5 V with a loading time of 60 min. This three-step technique proved beneficial in lowering the rate of corrosion. The microstructure revealed spherical clusters of needle-like crystals with each successive deposition step increasing the orientation of growth along the *c*-plane. The overall effect of this technique resulted in the densification of the first layer of coating over the Ti substrate while the additional electrodeposition generated a secondary porous layer of shorter and thicker acicular clusters. An intermediate thermal sintering step facilitated the creation of HAp coating with a variation in porosity gradient. Additionally, the three-step treatment involving electrodeposition, calcination, and electrodeposition showed a reduction in the rate of corrosion to ∼7.7 μm $year^{-1}$ when compared to the single-step electrodeposition.

5.1.1.3. Potentiodynamic electrodeposition. The electrodeposition of HAp under potentiodynamic conditions, as reported by A. Vladescu *et al.*,[76] involved HAp formation wherein deposition was initiated by sweeping the potential from an initial −1.4 V to a final 0 V potential at a sweep rate of 0.2 mV s^{-1}. A three-electrode system setup with Ti_6Al_4V alloy as the working electrode was employed. Further experiments were conducted with variations of pH under acidic conditions of 5 and 6. The morphological observations indicate the formation of HAp as flakes and needles at pH 5 and 6 respectively. The potential sweep ensured the formation of thick coatings with thickness reaching ∼455 nm for flakes and ∼2.27 μm for needles with crystal growth perpendicular to the substrate. In this scenario, the HAp flakes and needles had a Ca/P ratio of 1.32 and 1.51 respectively with the biocorrosion resistance being higher in the case of needle-like HAp when studied in a SBF electrolyte.

5.1.2. Influence of current density. Along with applied potential, current density is another crucial driving parameter in controlling the microstructure, coating thickness and nucleation

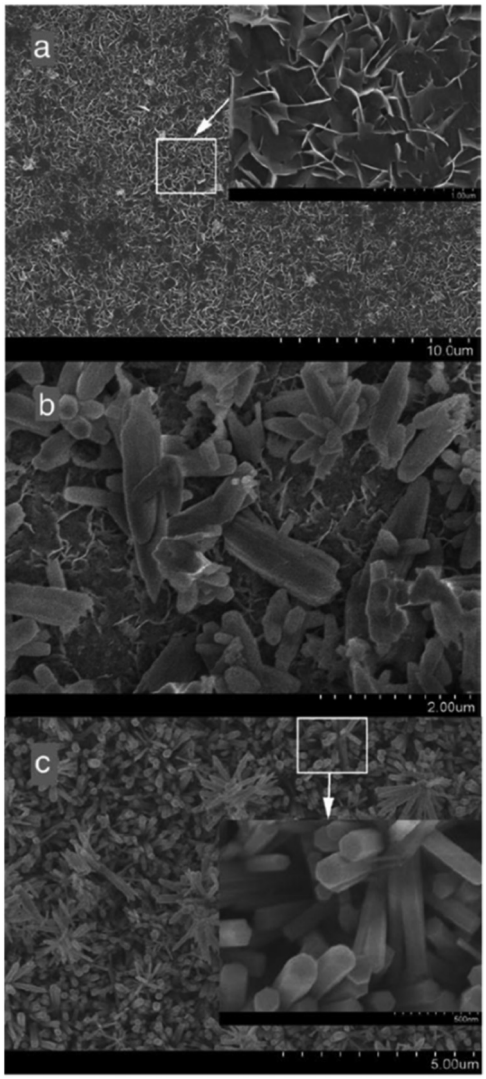

Fig. 3 Microstructural modifications of the coating electrodeposited at −1.8 V over various time intervals of (a) 10 min, (b) 20 min and (c) 60 min. Adapted from ref. 77 with permission from Elsevier.

rate of HAp. The migration of Ca^{2+}, PO_4^{3-} and OH^- ions may be influenced by the manipulation of applied current acting alone and coupled with parameters such as ultrasonication[78] and pulsing of applied current[3] among others. The growth of HAp crystals is accompanied by a simultaneous generation of H_2 bubbles which is proportional to the magnitude of applied current. These gas bubbles tend to interfere with mass transport, and reduce coating adhesive strength resulting in cracks thus making the control of current density crucial. The experimental conditions reported in select papers regarding these variations are presented in Table 2.

5.1.2.1 Galvanostatic electrodeposition. A report on preferentially oriented *c*-axis HAp crystals grown galvanostatically was presented by E. A. dos Santos *et al.*[80] A three-electrode setup with Ti_6Al_4V disc as the working electrode and a galvanostatic current density of 0.318 mA cm^{-2} was employed. This study dictates the fact that the orientation of crystals along the *a*,*b*-axes or *c*-axis is time-dependent under galvanostatic conditions. A 15 min loading time resulted in a haphazard arrangement of plate-like HAp. However, as the loading time increased to 1 h, the plates converted to needle-like with the crystal orientation predominating along the (002) *c*-axis. Additionally, the conversion of the initial flake-like microstructure to an acicular one can be attributed to the lowering of surface free energy during crystallization by reorienting growth in a direction parallel to the electric field, *vis-à-vis* perpendicular to the substrate. This produced acicular microstructures favoring a *c*-axis orientation.

5.1.2.2. Pulse/reverse pulse electrodeposition. Generally, the incorporation of pulses in applied current is a manipulation reported to improve the growth and coating characteristics such as geometry, porosity, surface defects, and crystal orientation.[81,82] Additionally, the inclusion of pulses has been reported to bring out uniformity and compactness with increased adhesive strength in comparison to coatings deposited under a direct continuous current.[83] Pulses in current favor enhancement in nucleation rate over growth assimilation with refinement in grain size and roughness.[84]

The introduction of pulses in direct current can be applied in two ways: a pulse current method (*viz.* unipolar pulse current) wherein the current oscillates between zero and a forward bias, and a reverse pulse current method (*viz.* bipolar pulse current) wherein the current alternates between two non-zero bias voltages. The variations in pulse current modes are depicted in Fig. 4. The factors to be considered while pulsing are the duration of pulse on/off time and the amplitude range of the current density which proves to be crucial for nucleation and phase purity of HAp. Under a direct continuous current, a higher accumulation of H_2 bubbles is witnessed. The consequences of these bubbles include detrimental effects on ion diffusion. However, by employing pulses, one essentially reduces the quantity of bubbles, thereby improving the mass transport between the diffusion layer and the substrate. This proves beneficial in terms of physico-chemical properties of the HAp coating with regard to crystallinity, adhesive strength, and biocorrosion.

The difference between pulse and reverse pulse techniques is that unipolar pulses create an ion vacancy near the cathodic double layer as a result of depletion of ions during the ON cycle (Fig. 4a and b). During the OFF cycle, with applied current being zero, replenishment of ion vacancy takes longer. This can be mitigated by employing a bipolar pulse current wherein the vacancy of ions near the cathode is replenished during the reverse pulse current (*i.e.*, a negative bias). This process ensures maintaining an ionic homogeneity in the diffusion layer (Fig. 4c and d). Furthermore, studies on the effect of pulse duration on homogeneity and microstructure with respect to duration of introduced pulses have been investigated.[85] The manipulation in the duration of pulses is known as the duty cycle and is reported to be a ratio of the active duration to the total duration and is expressed as[86]

$$\text{Duty cycle} = \frac{t_{ON}}{t_{ON} + t_{OFF}} \quad (9)$$

Table 2 Influence of current density on HAp coating characteristics

S. No.	Cathode	Electrolyte	Current density (mA cm^{-2})	Loading time (min)	pH	Temp (°C)	Ca/P ratio	Comments	Ref.
1	Ti_6Al_4V disc	0.61 mol L^{-1} $Ca(NO_3)_2$ + 0.36 mol L^{-1} $NH_4H_2PO_4$	0.318	15, 30, 60, 180	4.5	90	1.67	Galvanostatic electrodeposition with acicular HAp	80
2	Ti	0.42 M $CaCl_2$ + 0.25 M K_2HPO_4 + 2000 ppm H_2O_2	Pulsed between 1.0 and 0	60	—	—	—	Acicular HAp arranged in lotus-like fashion	155
3	Ti_6Al_4V	$Ca(NO_3)_2$ + $NH_4H_2PO_4$	Pulsed between (−0.25) and (−1.25)	30	4–5	37	—	Pulsed electrodeposition with a focus on the duty cycle	86
4	TiO_2 NTs	2.5 mM $CaCl_2$ + 1.67 mM K_2HPO_4 + 0.15 M NaCl	Pulsed between −10 and 0.01 for 100 cycles	~77	7.2	80	1.43	Thick acicular HAp	238
5	NiTi alloy	0.0167 M $Ca(NO_3)_2$ + 0.01 M $NH_4H_2PO_4$ + 0.1 M $NaNO_3$ + 10 mL L^{-1} H_2O_2	0.5	40	6.0	65	—	Flake-like HAp	256
6	Ti	1 g/L SiO_2 + 0.042 M $Ca(NO_3)_2$ + 0.025 M $NH_4H_2PO_4$	0.8	30	4.2	65	—	Needle-like HAp	257
7	AZ32B alloy	0.042 mol L^{-1} $Ca(NO_3)_2$ + 0.025 mol L^{-1} $NH_4H_2PO_4$ + 0.1 mol L^{-1} $NaNO_3$ + 20 mL L^{-1} H_2O_2	3 6 13	120	5.0	23	1.98 2.28 2.31	Plate-like HAp with variation in porosity	258
8	SS316 alloy	0.15 M $CaCl_2$ + 0.1 M $NH_4H_2PO_4$	5 10 20	60	—	25	1.34 1.35 1.45	Current pulsed between 0 and 5, 10, 20	235
9	TiO_2 NTs	8 mM $Ca(NO_3)_2$ + 5 mM $NH_4H_2PO_4$ + 30 mg L^{-1} GO	15 (pulsed duty cycle: 0.1)	65	6.0	65	1.57 (only CaP), 1.63 (CaP + GO)	Flake-like HAp/GO coatings with *a*,*b*-plane preferentiality	87
10	Ti	1.3 mM $CaCl_2$ + 0.84 mM K_2HPO_4 + 138 mM NaCl	12.5	4	7.2	95	—	Rod-like HAp coatings	259

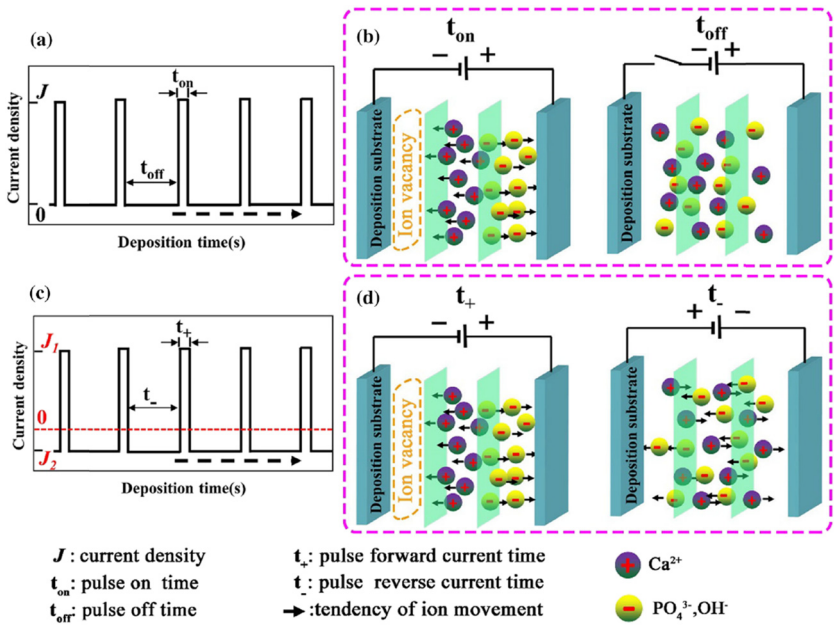

Fig. 4 Schematic representing the (a) and (b) unipolar pulse current method and (c) and (d) the bipolar pulse current mode. Adapted from ref. 54 with permission from Springer.

It was inferred that while maintaining a constant pulse OFF duration of 1 s, formation of HAp flakes was witnessed whereas an increase in the ON cycle duration increased deterioration in the HAp coating. On the other hand, while maintaining an ON time of 1 s, the variation in OFF duration from 1 s to 4 s led to morphological conversion from HAp flakes to spherical particles. This relates to the fact that during longer OFF cycles, a recovery in ionic concentration in the cathode double layer takes place. This may be witnessed by the sharp spike in current density at the start of the next ON cycle. Morphological control was observed with an increase in the size of flakes with the progressive increase in duty cycles applied during pulsed electrodeposition.[86] Additionally, the bipolar pulse current technique is useful in the design of multi-layered composites

like GO–calcium phosphate coatings[87] or polypyrrole–dopamine–HAp nanofilms.[88]

To summarize, the introduction of pulses in applied current witnessed an increase in the adhesive strength of the composite substrate compared to the galvanostatic electrodeposition. Furthermore, variation in duty cycle and magnitude of applied current significantly reduced the accumulation of H_2 bubbles. The unipolar pulse electrodeposition incorporates a relaxation time during the pause (applied current being zero) resulting in a slow rate of recovery of depleted ions. In the case of bipolar pulse electrodeposition, the substrate may be coated with a multi-component layer assembled during each optimized cycle of applied forward or reverse bias. A comparative study of the continuous, pulse, and reverse pulse electrodeposition of HAp and its influence on morphology and electrochemical behavior has been elucidated.[89]

5.1.3. Loading time. Under the influence of applied potential and applied current, the increase in loading time with respect to coating thickness generally witnesses an increased deposition of HAp, mostly influenced by the availability of Ca^{2+} and PO_4^{3-} ions near the vicinity of the electrode. In addition to thickness variation, the crystal orientation, morphology, adhesive strength and porosity can be tuned while further dictating the Ca/P ratio of the electrodeposited crystals to be either HAp, OCP, or DCDP among others. The loading time dramatically influences the nucleation mode and ultimately the predominant exposed facet of HAp. Initially, upon applying potential or current, the migration of ions towards the cathode initiates, followed by the increased formation of nucleation sites across the substrate. At this stage, the initial nucleation and crystal growth occur horizontally covering the substrate. The rate of formation of nucleation sites is higher than the rate of crystal growth. A prolonged loading time results in a drop in the rate of formation of new nucleation sites while favouring the rate of crystal growth. At this stage, crystallization occurs over the already grown thin horizontal coating thereby leading to a vertical growth. In ref. 90, the XRD profiles indicate a variation in crystal orientation with respect to loading time wherein the (200) plane, *i.e.*, the *a*,*b*-plane, shows a plate-like morphology. However, extended loading duration may result in a drop in total mass of the coating which is attributed to the reduction in adhesion strength of weakly nucleated crystals formed over a significantly thicker coating.[91]

5.1.4. Electrolytic pH. The mechanism of formation and electrodeposition of HAp necessitates the presence of OH^- ions near the working electrode. This supply of OH^- is fulfilled from the electrolytic dissociation of H_2O which in turn dictates the rate of conversion of HPO_4^{2-} to PO_4^{3-} *via* proton transfer. Furthermore, the distribution of OH^- and PO_4^{3-} species near the cathode is related to the electrolytic pH.[92] A change in crystallinity is observed in conjunction with pH regulation.[90] When electrodeposition was carried out at −0.8 V (*vs.* SCE) at a constant electrolytic temperature of 55 °C, the electrodeposits were phase-pure HAp. However, both crystallinity and coating thickness were influenced by pH variation. Under pH 2.5, a thin coating was obtained with reduced crystallinity. An increase in pH to 5.5 witnessed the growth of crystalline plate-like microstructures. Additionally, an enhancement in crystallinity was witnessed as pH shifted towards alkalinity. This variation in microstructure and crystallinity with the shifting of pH can be attributed to local supersaturation of OH^- ions at alkaline pH near the electrode thereby increasing the rate of electrodeposition.[90]

Another effect of pH variation can be witnessed in terms of the type of substrate employed during electrodeposition leading to an enhancement in nucleation, as investigated by employing a metal oxide cathode in ref. 93. This investigation revealed that at the TiO_2/solution interface, charge polarization is observed between the positively charged Ti and negatively charged O_2 sites. Due to this, the OH^- groups are effectively adsorbed onto the TiO_2 surface in comparison to the pure Ti metal. This isoelectric point for TiO_2 is reached at an alkaline pH of approximately 5 and 6. Outside this isoelectric pH, if the electrolytic pH is acidic, the surface positive charge gets modified, whereas an alkaline pH alters the net negative charge on the Ti substrate. This variation in surface charge enhances the adsorption of Ca^{2+} and PO_4^{3-} leading to the nucleation and growth of HAp. The progress of loading time significantly alters the Ca/P ratio on the adsorbed substrate. The pH near the vicinity of the cathode can be theoretically calculated from ref. 94 as

$$C = C_0 + \frac{2I\sqrt{\pi Dt}}{nF\pi DS} \quad (10)$$

where C is the concentration of OH^- ions at time t, C_0 is the initial OH^- ion concentration (mol L^{-1}), I the is applied current (A), D is the diffusion coefficient of OH^- ions (5.28×10^{-5} cm^2 s^{-1}), n is the number of electrons transferred, F is Faraday's constant and S is the surface area of the cathode (cm^2). Additionally, the modulation of pH is reported to influence the microstructure of the electrodeposits. An acidic pH favors the formation of plate-like deposits of $CaHPO_4$. Upon increasing the electrolytic pH, the microstructure converts from plate-like to spherical at pH 9 and from spherical to acicular at pH 11. A phase change from $CaHPO_4$ to phase-pure HAp is also witnessed upon reaching pH 9 and 11.[95]

5.1.5. Electrolytic temperature. Typically, electrodeposition of HAp is performed under elevated temperatures around 80 °C. However, compared to the industrially scaled process of plasma spray coating, electrodeposition offers a significant reduction of working temperatures of about ≤100 °C. The coatings deposited on Ti at room temperature displayed stronger adhesion to the substrate than those prepared at elevated temperatures with a shear stress of up to 106.3 MPa.[96] The regulation of electrolytic temperature as an electrodeposition parameter plays a vital role in fluid dynamics, namely, migration and diffusion of ions to electrode surface with the consequential effects observed in topographical changes. The experimental investigations in ref. 95 reveal mixed nanoparticle and nanoplate microstructures at pH 7–9 precipitated at 20 °C. However, at pH 11 (20 °C), clusters of nanoparticles were predominant. Upon increasing the deposition temperature to 40 °C, a reduction in nanoplates was seen at pH 7–9. At pH 11 (40 °C), bundles of needle-like crystals dominated. HAp formation is temperature dependent

with phase-pure HAp forming above pH 9 with the electrolytic temperature above 40 °C. However, it is possible to synthesize phase-pure HAp at 20 °C by maintaining a pH of 11.

C. M. Cotrut *et al.* investigated the influence of deposition temperature on microstructural HAp coating wherein electrodeposition was carried out under a sweeping potential from 0 V to −1.4 V at a scan rate of 0.2 mV s^{-1}.[97] The Ti disc was immersed in a Ca^{2+} and PO_4^{3-} precursor solution at pH 5 with a deposition temperature of 50 °C and 75 °C. The surface morphology of HAp deposited at both temperatures consists of plate-like microstructures with variations in coating density and porosity. However, coatings prepared at 50 °C were less crystalline with a Ca/P ratio of 1.39 as a result of ionic vacancies formed due to lower deposition rate. It can be concluded that electrodeposition temperature showed an influence over coating morphology and the Ca/P ratio. In an investigative work by Nam *et al.*,[91] electrodeposition of HAp onto a TiN/316L SS substrate showed variation in the mass transfer and weight of HAp deposited upon temperature variation. The mass of deposited HAp increased up to a working temperature of 50 °C. However, temperatures nearing 80 °C resulted in diminished HAp deposits. This was witnessed as a flaking phenomenon wherein HAp coating shows decreased adhesion capacity with increased porosity. The microstructural changes observed at 25 °C were plate-like indicating an increase in the *c*-plane surface area. Above 50 °C, the morphology converts to acicular crystals with a dominant *a*,*b*-plane.

5.2. Assisting parameters

5.2.1. Ultrasound-assisted electrodeposition. Ultrasonic assisted electrodeposition of HAp involves subjecting the electrolytic system to irradiation of ultrasonic waves whereby the deposition of HAp witnesses an increased nucleation rate and an improved coating uniformity.[98] This is attributed to the increased formation of OH^- during sonolysis that facilitates the conversion of $H_2PO_4^{2-}$ and HPO_4^- to PO_4^{3-} (eqn (13) and (14)). Additionally, the cavitation effect leads to collapse of cathodic H_2 bubbles which may otherwise generate weakly adhered HAp coatings. The consequence of ultrasonic waves on deposition topography is reflected in reduced growth along the *c*-axis. This is justified by the fracturing capability of ultrasound on weak inconsistent crystallites.[99] Sonofragmentation has an effect on the topographical surface roughness in a 0 W and 60 W ultrasonic environment.[98] AFM results, shown in Fig. 5, indicate reduction in the surface roughness factor for samples electrodeposited under 60 W ultrasonic irradiation (Fig. 5b) in contrast to those deposited in the absence of ultrasonic influence (Fig. 5a) indicating microstructural refinement through ultrasonic fracturing. Consequently, the crystallization of HAp *via* ultrasonic assisted electrodeposition yields smaller and refined crystals with increased crystals orienting along the *a*,*b*-plane whereas the absence of ultrasonic influence results in a preferred vertical *c*-axis growth.

Another effect is a substantial decrease in porosity and an increase in surface smoothness.[100] The microstructure resembled rounded needles in both cases with an increased density of needles with ultrasound exposure in relation to those without ultrasound (in Fig. 6). The effect of ultrasonic treatment and current density on the Ca/P ratio is significant, wherein an increase in current density from 2.5 mA cm^{-2} to 5.0 mA cm^{-2} changed the ratio from 1.53 to 1.58 but witnessed a decrease at higher current. The Ca/P ratios for ultrasonic assisted HAp at current densities of 2.5, 5.0 and 7.5 mA cm^{-2} were 1.69, 1.65 and 1.40 respectively. This may be attributed to the supporting effect of ultrasound facilitating the distribution of ions within the electrolyte. Its effects were noticeable on the crystallinity of deposited HAp. The surface roughness reduced from 7.04 μm to 0.76 μm at 7.5 mA cm^{-2} under 20 W ultrasonic power, indicating a control over surface roughness through control of current density and ultrasonic power. L. Fathyunes *et al.* assessed the effects of ultrasound during pulse electrodeposition of HAp/GO over anodized Ti.[101] Ultrasound aided in the dispersion of GO with a refinement in overall coating. The formation and implosion of microbubbles near the cathode enhanced the migration and the subsequent nucleation process. Furthermore, this

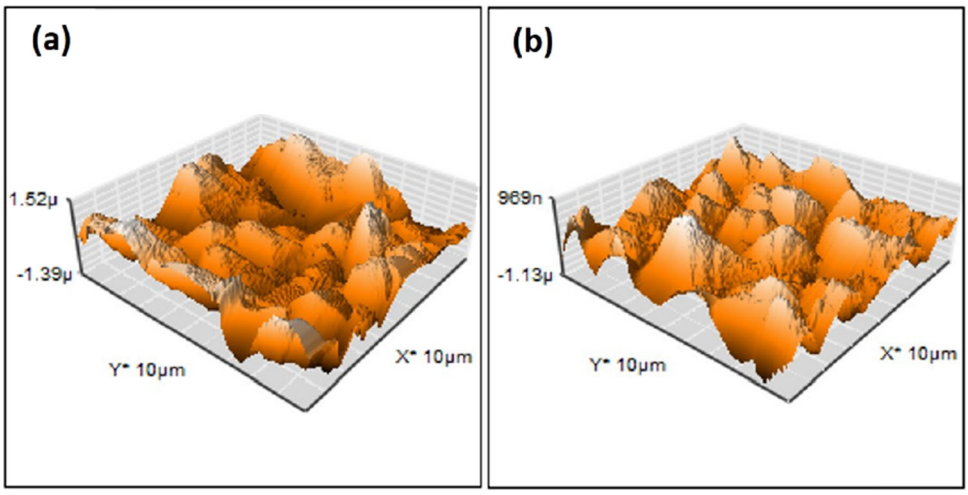

Fig. 5 AFM surface profile of HAp deposited *via* pulse electrodeposition in (a) the absence of ultrasonic irradiation and (b) at 60 W ultrasonic power. Adapted from ref. 98 with permission from Elsevier.

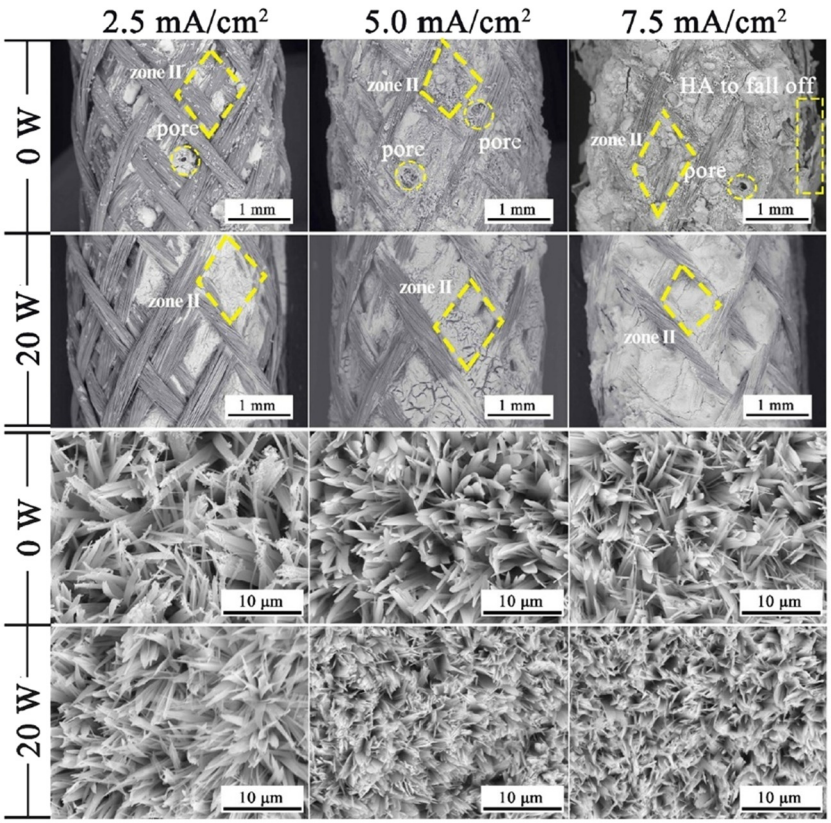

Fig. 6 Variation in microstructure in the presence and absence of ultrasound at different applied current densities. Reproduced from ref. 100 with permission from Elsevier.

ultrasonic agitation contributes to the formation of OH radicals. In addition to the fracturing effects, a plate-like morphology with increased uniformity was witnessed. The effects of ultrasound were also investigated under coupled ultrasound-assisted pulse electrodeposition.[102]

The overall purview of implementing ultrasonics during the process of electrodeposition relates to the microstructural formation of uniform and dense coating with reduced roughness and pore size. Furthermore, the crystal orientation of HAp in an ultrasonic assisted electrodeposition favors horizontal growth of HAp crystals as a result of the fracturing capability of ultrasonic waves.

5.2.2. Electrolytic additives influencing nucleation and growth. A typical HAp precursor electrolyte comprises of Ca^{2+} and PO_4^{3-} inorganic salts. In addition to this, an enhancement in the rate of HAp nucleation on the working electrode has been investigated *via* the chemical addition of additives with a significant change being witnessed in the growth rate and microstructural, crystalline and physical properties of the electrodeposited composite. For instance, an initial immersion of TiO_2 microstructures in NaOH prior to electrodeposition is reported to enhance the nucleation of HAp.[103] Upon treatment of Ti with NaOH, sodium titanate (Ti-ONa) is generated. Subsequent conversion to Ti–OH and exchange with electrolytic Ca^{2+} results in amorphous calcium titanate (Ti-OCa). The increased accumulation of Ca^{2+} creates an increase in positive charge over the substrate facilitating the migration of PO_4^{3-} ions. This nucleation process results in the consequent growth of compact HAp layers.[104]

Other additives such as KNO_3 and $NaNO_3$ promote an increase in the ionic strength of electrolytic species hence increasing conductivity. The NO_3^- ion undergoes electrochemical reduction to NO_2^- with the harnessed generation of OH^- ions.[105,106] An applied potential ranging from −1 V to −1.5 V (*vs.* SCE) facilitates the electroreduction of NO_3^- ions which is expressed as

$$NO_3^- + H_2O + 2e^- \rightarrow NO_2^- + 2OH^- \quad (11)$$

This reduction process increases the pH to ~10.4 at a reduction potential of −1 V (*vs.* SCE) as a result of the formation of OH^- at the vicinity of the cathode.

The incorporation of CNTs in the electrolytic composition led to the formation of HAp crystals preferentially orienting along the *a*,*b*-plane as witnessed from the flake-like crystalline microstructures.[107] The flakes grew perpendicular to the substrate with a thickness of up to 3 μm. Owing to the presence of CNTs, the composite displayed good corrosion resistance with reinforced mechanical strength.

5.2.2.1. Effect of H_2O_2. The reduction in interfacial adhesive strength between HAp and substrate is a cause for concern mainly attributed to the evolution of large amounts of H_2 gas bubbles, a consequential product from the electrolytic dissociation reaction

of H_2O. This dissociation occurs at increased potentials beyond the range of −2 V.[77] A higher potential of −5 V generates crater-like indents with diameters ranging from 40 μm to 250 μm.[94] Furthermore, this disruption in mass transport affects the Ca/P ratio of the deposited crystals resulting in deposition of either phase-pure HAp or other polymorphs of calcium phosphate.[73] The degradative effects of H_2 bubbles on coating properties can be mitigated by altering certain parameters such as current density, modifying the cell atmosphere (later discussed in Section 5.2.5.3), introducing ultrasonic waves[108] and application of pulses with addition of H_2O_2 to the electrolytic medium.[109] Unlike H_2O, the addition of H_2O_2 results in its electrolytic fragmentation generating OH^- ions given as

$$H_2O_2 + 2e^- \rightarrow 2OH^- \quad (12)$$

The incorporation of H_2O_2 resulted in the deposition of HAp with suitable changes in nucleation, phase purity and topography thereby improving adhesion and crystallinity.[110] By varying the volume of H_2O_2, the composition and topological characteristics of the coated calcium phosphate may be altered.[111] Experimental evidence indicates that the inclusion of 6% and 9% H_2O_2 gave a Ca/P ratio of 1.65 and 1.67 respectively with the coatings taking on a needle-like appearance in both cases. At a lower range of 3% H_2O_2, an insufficiency in OH^- near the cathode leads to the formation of β-TCP. This ionic vacancy affects the formation of HAp at H_2O_2 volumes greater than 9% and can be resolved by employing unipolar or bipolar pulsed deposition. The incorporation of pulses drastically reduces the formation of pits and cracks in the coating layer as shown in Fig. 7. Nam *et al.* investigated HAp electrodeposition under a potentiostatic regime of −1.65 V and noticed an increase in current density with the increase in the volume of H_2O_2 from 0% to 6%. The highest volume, *i.e.*, 6% H_2O_2, resulted in precipitation of HAp in the electrolyte as a powder. In the absence of H_2O_2, HAp deposited as a rod-like structure with a preferred *c*-axis growth. A variation in morphology from flake-like (at 2–4% H_2O_2) to a spherical structure at 6% H_2O_2 was witnessed.[91]

D. Gopi *et al.* examined HAp deposition onto 316L SS at a lower current density of 0.5 mA cm^{-2} with the inclusion of unipolar pulses and H_2O_2 as an additive.[112] The absence of H_2O_2 produced DCDP and OCP as the dominant phases. Lower H_2O_2 concentrations of 600 ppm and 1000 ppm resulted in DCDP crystals and trace amounts of HAp. However, H_2O_2 concentrations above 2000 ppm produced phase-pure HAp signifying the threshold levels of H_2O_2 needed to favor HAp crystal growth. This excess in OH^- ions raises the pH to alkaline levels near the cathode thereby generating sufficient growth of HAp. The phase purity was also studied by varying current densities between 1, 2 and 3 mA cm^{-2} revealing that the HAp (002) intensity increased ever so slightly as the magnitude of current density increased at 1000 ppm H_2O_2. Higher current densities were avoided to prevent the coating to turn porous while low currents resulted in a non-uniform flake-like morphology. High concentrations of H_2O_2 (6 or 9 vol%) with 2 min pulse OFF time resulted in acicular crystals while lower concentration (600–2000 ppm) with 2 s pulse OFF time resulted in HAp flakes. The coupling of the H_2O_2 additive with pulse electrodeposition proved effective in improving the crystallinity and orientation along the *c*-plane.

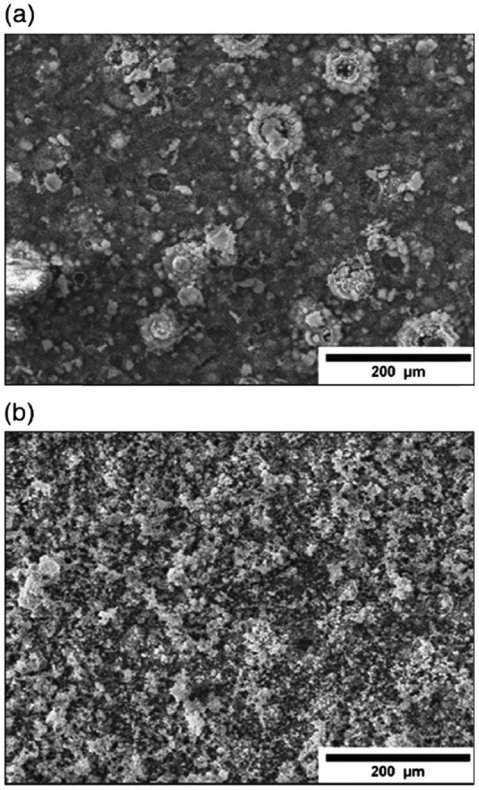

Fig. 7 SEM micrographs depicting electrodeposited HAp in a H_2O_2 electrolytic environment under the (a) direct current method and (b) pulsed current method. Adapted from ref. 111 with permission from Elsevier.

T. Mokabber *et al.* prepared HAp *via* a potentiodynamic process wherein H_2O_2 was added to lower the evolution of H_2 gas bubbles.[71] The presence of H_2O_2 leads to an increase in OH^- formation, which in turn increases the concentrations of HPO_4^{2-} and PO_4^{3-}, according to the following reactions:

$$H_2PO_4^- + OH^- \rightarrow HPO_4^{2-} + H_2O \quad (13)$$

$$HPO_4^{2-} + OH^- \rightarrow PO_4^{3-} + H_2O \quad (14)$$

5.2.2.2. Effect of chelates. The influence of chelating agents on the crystallization of HAp has been reported by D. He *et al.*, specifically the influence of EDTA on HAp deposition *via* the hydrothermal–electrochemical route.[113] With varying concentrations of EDTA, it was determined that the percentage crystallinity and coating thickness can be altered. The coating thickness decreased from 21 μm to ∼13 μm as concentrations increased, while the adhesive strength towards the substrate increased. The topography of the composite displayed increased growth along the *c*-axis in the absence of EDTA whereas the addition of EDTA oriented the microstructure growth along the *a*,*b*-plane. This shift in microstructure is due to the effect of supersaturation of chelated Ca-EDTA. The binding affinity of EDTA towards the ions along the crystal plane is stronger with the (100) facet (*viz.* *a*,*b*-plane) than with the (001) facet (*viz.* *c*-plane)

thereby hindering deposition along the *c*-axis.[114] At reduced levels of EDTA, the supersaturation of the electrolyte is lowered with a consequential increased growth rate along the *c*-axis.[113] The addition of EDTA as an additive takes advantage of the control of crystal orientation more towards the *a*,*b*-axes and can be related to control of the supersaturation of the chelate complex.

Trisodium citrate has been reportedly employed as an organic modifier and complexing additive in electrodeposition.[115] After a 1 h loading time, a gradual increase in citrate ion concentration modified the hexagonal rod-like crystals (at [citrate] = 0) to a tapered acicular cone (at [citrate] > 5). The addition of citrate inhibits the early formation and nucleation of OCP, mainly attributed to an increase in pH near the vicinity of the electrode. Furthermore, the presence of citrate altered the crystal characteristics as a result of its adsorption and complexation with Ca^{2+} thereby arresting crystal growth along the *a*,*b*-axes while promoting *c*-axis growth during electrodeposition.

5.2.2.3. Simultaneous anodization–electrodeposition of HAp. Typically, electrodeposition of HAp is carried out employing ionic electrolytic precursors involving Ca^{2+} and PO_4^{3-} salts. Furthermore, employing dispersed HAp nanoparticles within aqueous electrolytes is typically reported under the electrophoretic deposition technique.[116] However, J.-M. Jang *et al.* investigated the electrodeposition of dispersed HAp nanoparticles onto the TiO_2 NT substrate.[117] The experimental protocol involved a unique simultaneous anodization–electrodeposition technique, shown in Table 3, involving the simultaneous growth of anodized TiO_2 up to 800 nm in length while depositing a HAp coating with thickness up to 100 nm. The dispersed HAp nanoparticles formed a layer onto TiO_2 and grew vertically with a particle size of 13–17 nm. The ultrafine deposited layer assumed a spherical microstructure (shown in Fig. 8) with crystallographic studies revealing the presence of phase-pure HAp. An XPS depth-profiling was carried out after employing an Ar^+ ion sputtering surface treatment for 100, 200 and 300 s revealing varying content of Ca and P. The Ca and P content varied in the range of 0.61–0.90 and 0.58–0.24 respectively upon each successive Ar^+ sputtering time. The reason for the decrease in the content of P with depth was attributed to the low capacity of adsorption and interaction between the nanotubular TiO_2. However, as loading time increases, the quantity of P-sites increases due to the formation of hydrated $Ti(OH)_2$. This facilitates the enhanced adsorption of PO_4^{3-}, HPO_4^{2-} and $H_2PO_4^-$ ions.

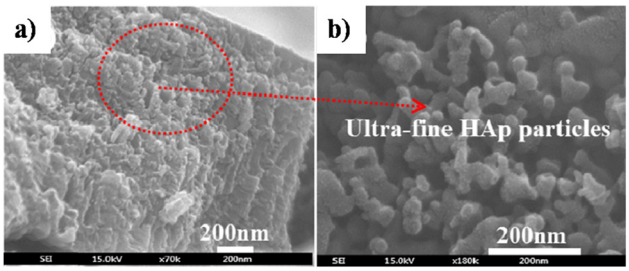

Fig. 8 FESEM of (a) HAp electrodeposited over TiO_2 NTs *via* the simultaneous anodization–electrodeposition technique and (b) the microstructure of the deposited HAp particles. Adapted from ref. 117 with permission from Elsevier.

Similar reports on the simultaneous anodization–electrodeposition technique are reported in ref. 118 and 119 initiated by the anodization of the Ti substrate with simultaneous electrodeposition of HAp from a dispersion of ultra-fine HAp nanoparticles. The electrodeposited HAp nanoparticles displayed an increase in size in addition to an increase in the weight percentage of HAp. Furthermore, the technique of simultaneous anodization–electrodeposition proved effective in the modulation of Ca/P ratios of the deposits, wherein Ca/P ratios were 1.26, 1.53 and 1.65 for the mixed electrolyte containing 0.1, 0.15 and

Table 3 Comparison of the role of additives on HAp coatings

S. No.	Cathode	Electrolyte	Potential (V)	Loading time (min)	Temp (°C)	Additive	Ca/P ratio	Comments	Ref.
1	Ti	0.042 M $Ca(NO_3)_2$ + 0.025 M $NH_4H_2PO_4$ + 0.1–1.5 wt% H_2O_2	−1.4, −1.6, −1.8	1, 2, 3, 5, 30	65	H_2O_2	1.67	Reduction in cathodic H_2 generation	71
2	Ti_6Al_4V	0.025 mol L^{-1} $Ca(NO_3)_2$ + 0.015 mol L^{-1} $NH_4H_2PO_4$ + (0.00025 to 0.001 mol L^{-1}) EDTA-2Na. Current density = 1.25 mA cm^{-2}	—	120	120	EDTA-2Na	—	Chelate assisted electrodeposition of HAp	113
3	Ti	0.042 mol L^{-1} $Ca(NO_3)_2$ + 0.025 mol L^{-1} K_2HPO_4 + 0–2 wt% CNTs (pH: 4.7)	−1.4	60	—	CNTs	—	CNTs promote *a*,*b*-plane preferentiality	107
4	TiO_2 NTs	1.6 M $NH_4H_2PO_4$ + 0.65 M NH_4F + 0.8 wt% HAp	21	∼47	28	HAp nanoparticles	—	Simultaneous anodization–electrodeposition of ultra-fine HAp	117
5	TiO_2 NTs	1.6 M $NH_4H_2PO_4$ + 0.8 M NH_4F + 0.1, 0.15, 0.25 wt% HAp	28	120, 150	—	HAp nanoparticles	1.26, 1.53, 1.65	HAp electrodeposition from dispersed HAp nanoparticles as the precursor	118
6	TiO_2 NTs	1.7 M $NH_4H_2PO_4$ + 0.4 M NH_4F + 0.1 wt% Pd + 0.2 wt% Ag + 0.3 wt% HAp	28	10, 15, 30, 45, 90, 120	—	HAp nanoparticles	1.67	Ultra-fine deposition of spherical HAp particles	119
7	Ti plate	HAp nanoslabs in 1 : 1 H_2O–ethanol mixture. Current density: 1, 3, 5 mA cm^{-2}	—	—	—	HAp nanoslabs	—	Dispersed HAp nanoslabs/nanoplates electrodeposited onto a Ti plate	244

0.25 wt% of dispersed HAp nanoparticles. The technique of simultaneous anodization–electrodeposition revealed that the incorporation of Ca^{2+} and PO_4^{3-} ions is significantly affected by the composition of the substrate.

5.2.2.4. Simultaneous precipitation–electrodeposition of HAp. The technique of simultaneous precipitation–electrodeposition, unlike simultaneous anodization–electrodeposition, involves deposition of HAp crystals without electrochemical modification of the cathodic material like anodization.[120] The method entails drop-wise addition of one precursor (either Ca or P) into an electrolytic cell containing the other precursor, while simultaneously initiating potentiostatic electrodeposition (experimental parameters in Table 3). XRD profiles reveal that when the Ca^{2+} precursor is added to the PO_4^{3-} electrolyte, an enhanced preferential growth along the *c*-axis is witnessed over a loading time of 4 h. There is a significant improvement in the degree of crystallinity from this technique in lieu of conventional HAp electrodeposition. All samples had an initial uniform layer of submicron crystals with the increase in acicular crystals grouped as hemispherical clusters (shown in Fig. 9). The technique proved effective in improving the anti-corrosiveness and adhesion strength of the HAp coating.

5.2.3. Influence of the applied magnetic field. Being a diamagnetic mineral, HAp may be influenced *via* the applied external magnetic field *via* substitution of paramagnetic transition metal species like Mn^{2+}, Co^{2+} and Fe^{2+}.[121] However, the nucleation of pure stoichiometric calcium phosphate may be influenced by an external magnetic field. Depending on the field strength, reports indicate that the magnetic field affects the orientation and assembly of HAp crystals. As a result, a possibility exists for manipulation of the directional growth, with tunable preferentiality either along the *c*-axis or along the *a*,*b*-axes. In order to ascertain the plausible impact of magnetic flux upon the crystallization process one must scrutinize the effect of magnetic flux on crystal nucleation and orientation either in the presence (*i.e.* magnetoelectrodeposition) or in the absence of electrical flux (*i.e.* precipitation in *B* alone). It is to be noted that the studies carried out in the absence of electric flux (*j*) may or may not contain any substrate whatsoever. This section will disseminate both aspects, first, by introducing the process of HAp precipitation in the presence of *B* alone and later moving on to the process of magnetoelectrodeposition of HAp.

H. E. Lundager Madsen reported that phosphates of diamagnetic ions are affected under a magnetic field resulting in variation of phases.[122] The precipitation resulted in the formation of large brushite crystals in the absence of *B*, whereas at 0.27 T, stable HAp crystals persisted. Although the crystal size reduced, the rate of crystallization increased with new nucleation sites leading to smaller but higher number of crystals. The precipitative crystallization of HAp under the influence of a magnetic field was understood *via* a proposed mechanism which includes a proton transfer from a weak acid to H_2O. The rate of transfer of protons is slow in the case of a weak acid. Additionally, the rate of crystallization of HAp increases as the pH of the medium shifts towards alkaline.[123] Although the magnetic field had no effect on the mass transport of the diamagnetic species, the relative increase in the rate of crystal formation was correlated to the rate of proton transfer from the weak acid to water (since proton spin is influenced by *B*) thereby revealing that the precipitation of crystals in a magnetic field can be related to the rate of proton transfer.

Unlike the previous study conducted at a low magnetic field of 0.27 T, slipcasting was carried out in the range of 10–12 T field strength wherein a slurry of HAp was allowed to set in a crucible.[124,125] The magnetic field applied was parallel to the direction of the gravitational field. XRD profiles (shown in Fig. 10) revealed a remarkable effect of the high magnetic field on the orientation of HAp. Horizontal cut cross-section displayed a dominant peak intensity for the exposed *a*,*b*-plane. This is an indication that when a slurry of HAp is slipcast while exposed to an external high magnetic field, the nucleation and the subsequent crystal orientation can be controlled to a great extent. Similar experiments were carried out by employing a surfactant and performing milling before slipcasting[126,127] to primarily prevent the aggregation of HAp particles during slipcasting.

Okido *et al.* reported a magnetic field assisted deposition method, termed the heat substrate method, wherein a similar control over crystal orientation was accomplished.[128] The experiment involved heating the substrate (a strip of Ti foil) with the aid of an electric current to precipitate HAp in the presence of a magnetic flux of 12 T. Note that this technique is not magnetoelectrodeposition since the applied electric current is for heating of the mounted substrate and there is an absence of electric flux (*i.e.*, no cathode and anode). The foil was mounted both parallel and perpendicular to *B*. In the absence

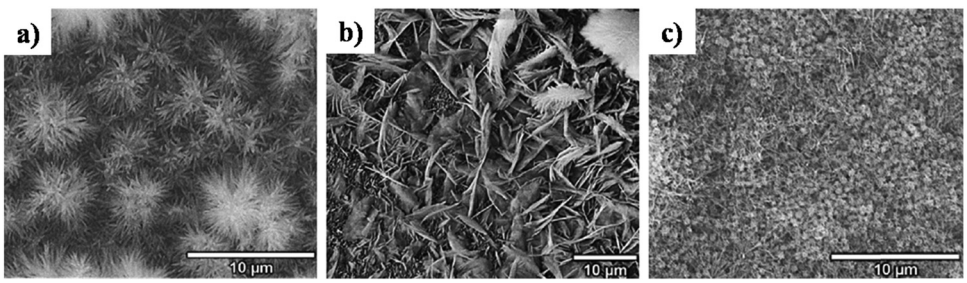

Fig. 9 FESEM of HAp crystals deposited *via* the simultaneous precipitation–electrodeposition technique with dropwise addition of (a) P precursor, (b) Ca precursor and (c) Ca + P precursor. Reproduced from ref. 120 with permission from Elsevier.

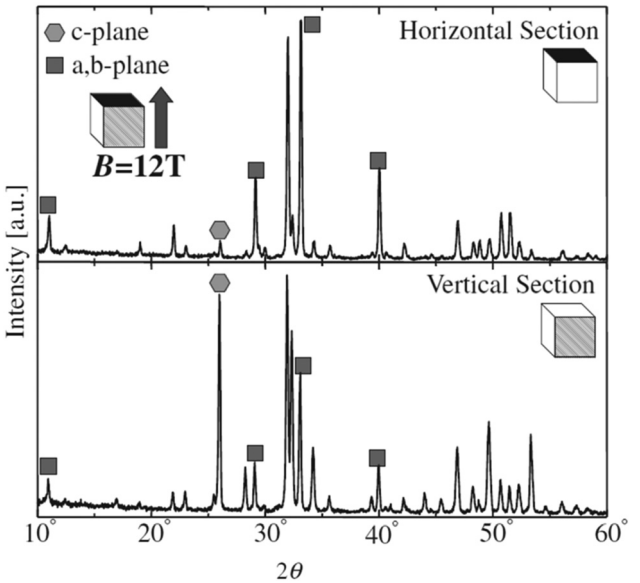

Fig. 10 XRD diffraction indicating the orientation of the crystal facets of slipcast HAp at B = 12 T. Adapted from ref. 124 with permission from The Japan Institute of Metals and Materials.

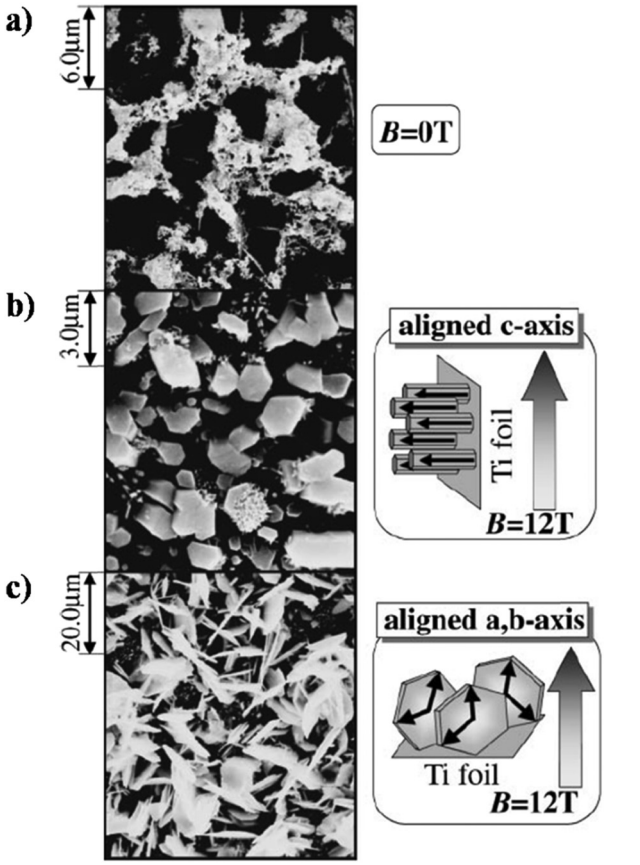

Fig. 11 SEM images of HAp electrodeposited *via* the heat substrate method over Ti foil under a magnetic field strength of (a) B = 0, (b) B = 12 T ($B \perp j$) and (c) B = 12 T ($B \parallel j$). Reproduced from ref. 124 with permission from The Japan Institute of Metals and Materials.

of B = 12 T, the HAp crystals were unoriented (Fig. 11a). At an applied field of 12 T, the resultant HAp crystals were hexagonal pillars when the foil was oriented parallel to B (Fig. 11b) and thin hexagonal flakes when the foil was perpendicular to B (Fig. 11c). For HAp, this would be the *a*,*b*-plane aligning to the direction of B. Additionally, it must be noted that both slipcasting and the heat substrate method, when performed at B = 12 T, resulted in predominant exposure of the *c*-plane when B was parallel to the slurry and Ti foil respectively.

The variation between the heat substrate method and magnetoelectrodeposition is that the latter involves creation of MHD and mass transport of species between two electrodes. In order to determine the sphere of influence of magnetic flux in an electric field, a comprehensive account of its effect over mass transport, electrode kinetics and electrochemical equilibria has been reported by T. Z. Fahidy.[129,130] The phenomenon of magnetoelectrodeposition involves correlating the effects of solution dynamics, termed magnetohydrodynamics (MHD), resulting from the Lorentz force and Kelvin force on the enhancement or suppression of migratory nature of the ionic species. The Lorentz force is the magnetohydrodynamic force (F_B), mathematically expressed as the cross-product of magnetic field strength (B) and current density (j) vectors ($F_B = j \times B$). The vector cross-product is zero when both are parallel or antiparallel in their directional nature and maximum when they are perpendicular to each other. This maximum generates a convective flow within the electrolyte when ($B \perp j$). However, electrodeposition can occur when F_B equals zero which is attributed to the concentration gradient of paramagnetic and diamagnetic species, *i.e.*, the Kelvin force.[131] As electrodeposition transpires in the presence of a magnetic field, the Lorentz force induces a convective flow which is speculated to alter the ionic concentration at the electrode–electrolytic diffusion layer.[132] When the Lorentz force acts in the direction similar to the direction of conventional forces, an increase in current density is witnessed. This enhances the mass transport and size of the crystals.[133]

The effects of a superimposed external magnetic field with electric field (j) on the electrolyte on electrodeposition can be determined by recognizing the various possible combinations wherein magnetic flux (B) can align with respect to j. A schematic depicted in Fig. 12 illustrates the assembly of the electrodes between the poles of the electromagnet. The pole pieces of the electromagnet are kept horizontal to the electrodes. The magnets may be placed vertical to the electrodes; however, the outcome of the vector cross-product yields similar results. From the figure, it may be deduced that there may be five possibilities of interaction between B and j among the three possible electrode orientations while keeping the magnet positions fixed. The alignment in Fig. 12a and b represents B parallel to j ($B \parallel j$) and B perpendicular to j ($B \perp j$) respectively. Fig. 12d has an electrode setup similar to Fig. 12a but the vector alignment of B with j is anti-parallel in nature. Fig. 12c and e exhibits conditions wherein the alignment of B with j is perpendicular in nature but culminates in migration of ions working against the gravitational field (Fig. 12c) and vector

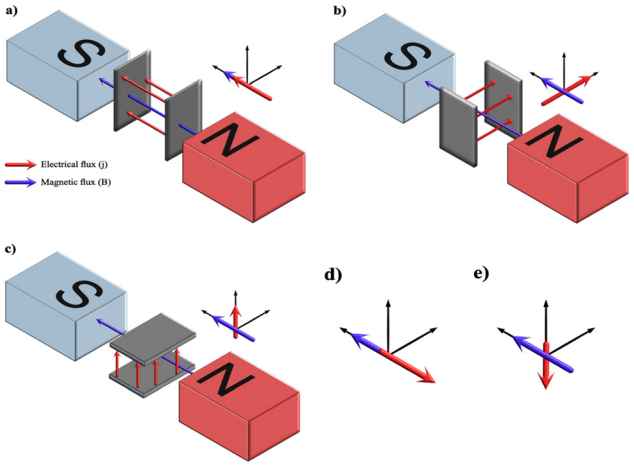

Fig. 12 A schematic of the possibilities of orientation of electrode configuration with respect to the electromagnets and the consequent electrical and magnetic flux directions with its representation indicated as (a) parallel, (b) perpendicular, (c) perpendicular aligned against gravity, (d) antiparallel and (e) perpendicular aligned with gravity.

forces working along the lines of the gravitational field (Fig. 12e) respectively.

For diamagnetic species, in the case of parallel and antiparallel orientation of B and j (cell configuration analogous to Fig. 12a and d respectively) the magnitude of j increases with B. This is attributed to the Kelvin force, *i.e.*, concentration gradient force. The diamagnetic concentration gradient force can be up to three orders of magnitude smaller than the paramagnetic counterpart, yet it is sufficient to induce convection within the electrolyte.[134] In the case of perpendicularity between j and B (Fig. 12b, c and e) the vector magnitude of j is maximum resulting in electrodeposition due to Lorentz force.

The crystal growth of HAp varies significantly as a result of the influence of Lorentz force and Kelvin force. Experimental reports by A. Tian *et al.*[135] and C. Liu *et al.*[136] discuss electrodeposition under a static magnetic field with magnitudes of 0.25 T, 0.5 T and 1.0 T in perpendicular ($B \perp j$) and parallel ($B \parallel j$) orientations. The experimental parameters can be seen in Table 4. The former study employed Ti foil as a substrate whereas the latter employed TiO_2 nanotubular arrays. A zero magnetic flux environment was taken as control, which is analogous to bare electrodeposition. The control yielded a coating of thin flakes of HAp. However, the orientation ($B \parallel j$) produced spherical HAp while the ($B \perp j$) orientation generated needle-like crystals. The formation of spherical and acicular HAp can be explained due to the additional micro-MHD vortices occurring on the cathode surface.[137,138] When ($B \parallel j$), the cathode is oriented perpendicular to both B and j (interpreted from Fig. 12a). In this scenario, the cathode experiences a primary MHD flow along the periphery of the electrode, resulting in additional micro-MHD flow. These micro-MHD forces are reported to suppress the 3D nucleation thereby promoting the lateral growth of spherical particles. However, when ($B \perp j$), the cathode is parallel to B (Fig. 12a and c), thereby resulting in nucleation and crystal growth along the vertical direction consequently yielding acicular HAp.

The control of orientation and morphology of HAp crystals can be achieved through manipulation of mass transfer *via* controlled electric and magnetic fields. P. M. S. Tohidi *et al.* performed electromagnetic assisted deposition of HAp onto a NiTi substrate in a pulsed electrodeposition environment.[139] In addition to variation of vector orientation, the experiments included the study of position of the cathode with respect to the magnetic pole pieces. The cathode may be placed near the north or south pole pieces of the electromagnet. An optimized experimental condition (i3-B||J-m101-t5) resulted in a plate-like microstructure. However, increasing the field strength from 101 mT to 250 mT increased the presence of micro-voids and porosity. Under a constant loading time, current density and field strength, the orientations of ($B \perp j$) and ($B \parallel j$) resulted in acicular and spherical morphology respectively. Furthermore, under ($B \parallel j$) orientation, the positioning of the working electrode closer to either the north or south pole of the electromagnet resulted in the formation of spherical or flake-like crystals respectively.

Table 4 Influence of magnetic field strength on coating microstructure

S. No.	Cathode	Electrolyte	Current density (mA cm^{-2})	Loading time (min)	pH	Temp (°C)	Magnetic field (T)	Comments	Ref.
1	Ti foil	0.3 mM $Ca(H_2PO_4)_2$ + 0.7 mM $CaCl_2$	—	15	7.0	~140	12	Heat substrate method of Ti foil favors *a*,*b*-axes growth along the direction of B	128
2	Ti	0.042 M $Ca(NO_3)_2$ + 0.025 M $NH_4H_2PO_4$	10, 15	40	4.5–5.5	85	0.5, 1.0	($B \perp j$) and ($B \parallel j$) result in *c*-plane and *a*,*b*-plane crystal orientation respectively	135
3	TiO_2 NTs	0.042 M $Ca(NO_3)_2$ + 0.025 M $NH_4H_2PO_4$	10	60	4.5–5.5	85	0.25, 0.5, 1.0	Plate like when B = 0, acicular when $B \perp j$ and granular when $B \parallel j$	136
4	Micro-arc oxidized Mg alloy	0.1 mol L^{-1} $Ca(NO_3)_2$ + 0.04 mol L^{-1} $NaNO_3$ + 0.06 mol L^{-1} $NH_4H_2PO_4$	10	60	6.0	85	1.0	Spherical HAp at 1 T when $B \parallel j$	140
5	NiTi rod	0.0084 M $Ca(NO_3)_2$ + 0.005 M $NH_4H_2PO_4$ + 0.1 M $NaNO_3$ + 0.0588 H_2O_2	3, 5	3, 5, 7, 10, 15	6.0	65	0.08, 0.101, 0.12, 0.25	Variation in the Ca/P ratio depending on applied B	139

Likewise, HAp particles electromagnetically deposited over Mg alloy were spherical with a diameter of ~50 nm.[140] An improvement in the anchoring capability of HAp was witnessed when a micro-arc oxidized substrate was employed. A lowered (002) plane intensity can be ascribed to the formation of spherical particles. The control experiment carried out in the absence of a magnetic field indicated a crystal growth along the (300) plane.

To summarize, the heat substrate method resulted in hexagonal pillars at 12 T, whereas magnetoelectrodeposition produced needle-like crystals when ($B \perp j$) at a lower B of 0.25–1.0 T. Additionally, it was revealed that irrespective of the deposition method, the application of a magnetic field predominantly brought about crystal orientation along the (002) c-plane ($2\theta \approx 26^\circ$) when ($B \perp j$). Similarly, the absence of a magnetic field favored crystal orientation along the a,b-axes. This leads to the revelation that the control and refinement of the crystal size, orientation of specific planes of HAp and control of coating roughness can be engineered by the application of a magnetic field during electrodeposition.

5.2.4. Effect of microgravity on nucleation. The flow and migration of ionic species within an electrolyte behave intriguingly under surface gravity and microgravity. The crystallization of calcium phosphate has been reported to decrease under the effects of microgravity. This may be attributed to the collapse of heterogeneous nucleation kinetics in favor of a more homogeneous nucleation and mineralization. As a consequence, an increased porous structure is obtained due to the drastic decline in effective collision kinetics between ions. In order to create a microgravity environment, one may employ high magnetic fields or it can be simulated in a double jet airplane with a parabolic flight of 20 s.[141]

Y. Ya-Jing *et al.* reported on the microgravity effects over HAp electrodeposition onto Ti_6Al_4V substrates. The substrate was functionalized with negatively charged self-assembled mono layers (SAMs) comprised of –COOH and $-PO_3H$ in order to better facilitate induced growth by modification of substrate surface energy.[142] Microgravity was simulated *via* a high magnetic field inducing superconducting magnet. The applied field strength had a maximum of 16 T. A near 0 G environment arose when the magnetization force F_m balanced the gravitational force F_G in a vertical arrangement wherein the two forces were anti-parallel to each other.[143] The HAp particles took on a spherical microstructure with not much agglomeration due to reduced collision kinetics in this microgravity environment. With HAp having a diamagnetic susceptibility, the ionic species Ca^{2+} and PO_4^{3-} would remain suspended in the microgravity environment due to the drop in convection and solute mass transport. However, the effect of an applied electric field on nucleation (*i.e.* an orientation wherein j and B are anti-parallel and magnetic flux B aligns against gravitational field G) in this simulated microgravity environment has not yet been fully explored. By understanding the mechanics of the piezoelectric nature of HAp acting in synergy with MHD forces in a microgravity environment, one may effectively overcome the predicament of osteoporosis in space.

5.2.5. Influence of electrolytic pressure and the cell atmosphere. Literature sources indicate that the performance of any electrochemical reaction in both high and reduced pressure results in modifications in microstructural topography with an enhancement in adhesive strength towards the substrate, superior uniformity and compactness of coatings, reduction in pits and cracks,[114] refined grains and control over crystal orientation.[144,145] The experimental parameters employed in various reports are indicated in Table 5.

5.2.5.1. Effect of high pressure. S. Ban and J. Hasegawa studied the effect of high pressure on HAp crystal growth by employing a combined hydrothermal-electrodeposition method.[146] A quartz beaker electrochemical cell was sealed in a high pressure autoclave, thereby creating a closed system, wherein morphological modifications were studied with variation of temperature, current density and time. The crystals grown in this high pressure environment were hexagonal needles. A decrease in aspect ratio was observed with increasing temperature and loading time attributed to the decreased nucleation sites at high pressure. Furthermore, a reduction in solubility of crystals was witnessed. This resulted in a subsequent growth on existing crystals thereby increasing the crystal size. During electrodeposition, an increase in liberation of H_2 gas at the cathode was seen due to the increase in current density. However, due to the closed environment, this created a saturation of overall electrolytic pH thereby enabling modulation of Ca^{2+} and PO_4^{3-} sites.

An earlier study by S. Ban *et al.* reported a similar experimental work while varying the cathodic substrates.[147] The growth of HAp on various metal substrates, herein Ti, Zn, Ni, Fe and stainless steel plates, was studied exemplifying the relation between formation of phase-pure HAp crystals and ionic dissolution of the cathode. The study was carried out under temperatures of 100, 150 and 200 °C. This comparative study noted the formation of phase-pure HAp on all substrates only at 100 °C. Temperatures exceeding 100 °C resulted in mixed phases for all substrates with the exception of Ti. Vertically oriented hexagonal HAp crystallized at all temperatures on the Ti plate. An increase in temperature resulted in an increased deposition over the already nucleated crystals thereby making the hexagonal rods thicker. Consequently, an increase in the Ca/P ratio was witnessed in the case of Ti, signifying the preferentiality of (002) crystal orientation with the exposed c-plane.

Hydrothermally assisted electrodeposition of HAp over a Ti mesh substrate was carried out by A. Yuda *et al.*[148] The results presented indicate the formation of a homogeneous coating with variation in morphology as a function of hydrothermal temperature. At 90 °C, plate-like deposits and at 100 °C, a mixture of plate- and needle-like morphology were obtained. A further increase in temperature to 150 °C witnessed a complete shift in morphology to acicular. The dimensions of the needles grown at 100 °C were 7 μm in length and 0.5–1.0 μm in width while those grown at 150 °C were 60–90 μm in length and 2–7 μm in width. The assimilation of the needles was hexagonal with an increase in length dictating an increase in the Ca/P ratio of 1.38 (90 °C), 1.40 (100 °C) and 1.54 (150 °C). This electrodeposition technique

Table 5 Effect of pressure and controlled atmosphere on the morphological outcome during electrodeposition

S. No.	Cathode	Electrolyte	Potential (V)	Current density (mA cm^{-2})	Loading time (min)	pH	Temp (°C)	Pressure (Torr)	Ca/P ratio	Comments	Ref.
1	Ti plate Zn plate Ni plate Fe plate SS plate	2.5 mM $CaCl_2$ + 1.67 mM K_2HPO_4 + 137.8 mM NaCl	—	12.5	60	7.2	100, 150, 200	~12000 @ 200 °C	1.47–1.65 1.59–1.03 1.49–1.45 1.58–1.39 1.45–1.51	Dissolution of metal resulting in mixed phase of calcium phosphate	147,260
2	Ti plate	2.5 mM $CaCl_2$ + 1.67 mM K_2HPO_4 + 137.8 mM NaCl	—	5–25	10–120	7.2	90–200	—	—	High pressure electrodeposition	146
3	Ti mesh	2.5 mM $CaCl_2$ + 1.67 mM K_2HPO_4 + 137.8 mM NaCl	—	12	60	7.2	90, 100, 150	—	1.38 @ 90 °C, 1.40 @ 100 °C, 1.54 @ 150 °C	Microstructure variation from plate-like to needles with the change in autoclave temperature	148
4	Anodized Ti_6Al_4V	0.138 mol L^{-1} NaCl + 0.016 mol L^{-1} K_2HPO_4 + 0.02 mol L^{-1} $CaCl_2$	—	1.25	120	—	120	—	—	Reduction in the (002) plane	261
5	Ti_6Al_4V	0.04 M MCPM	4–10	—	60	~3.0	0–60	80	1.05–1.69	Transition from plate to needle to granular HAp	150
6	Ti_6Al_4V	0.04 M MCPM	4–10	—	20–120	3.0	60	80	1.54	Low pressure electrodeposition	262
7	Ti_6Al_4V	0.04 M MCPM	4–10	—	20–120	~3.0	0–60	80	1.09–1.83	HAp content increases with potential and temperature at 80 Torr	151
8	Ti plate	2.5 mM $Ca(NO_3)_2$ + 1.5 mM $NH_4H_2PO_4$	—	1.0	30, 60	4.2–5.1	80	Ambient pressure	—	Atmosphere controlled deposition	152

of high pressure coupled with high temperature facilitates reduction in the viscosity of the electrolyte.[149] The low viscosity enhances the rate of diffusion of ions, rate of crystal growth and orientation of the HAp crystal along the *c*-axis.

5.2.5.2. Effect of low pressure. Alternatively, the effect of sub-atmospheric pressure on morphology of HAp crystals grown on the electrode is quite a unique one elaborated in two literature reports. The experiments, both carried out by M.-C. Wang *et al.*, were carried out in a reduced pressure environment, specifically 80 Torr. This reduced pressure environment was achieved by placing the electrolytic cell in a vacuum chamber. The first and second study involved the morphological study of the coatings on Ti_6Al_4V alloy with variations in deposition potential[150] and deposition time respectively.[151] With the precursor to be mono-calcium phosphate monohydrate (MCPM) in both studies, the initial stages of electrodeposition generate both MCPM and DCDP as plates. However, variation of potential over a range from 4 V to 10 V resulted in an increase of HAp as the predominant phase. The morphology transitioned from plate-like at 4 V to acicular at 7 V and finally granular at 10 V.

This sub-atmospheric pressure condition proved to be advantageous in terms of mechanical strength of coating. This can be elucidated from the illustration depicted in Fig. 13. It is well known that any electrochemical process carried out in aqueous medium results in the generation of H_2 gas bubbles at the cathode. The interspersed gas bubbles tend to distort the double layer between the electrode and the electrolyte (dotted line shown in Fig. 13a). The bubbles hinder the migration of solvated ions thereby obstructing crystal nucleation and growth

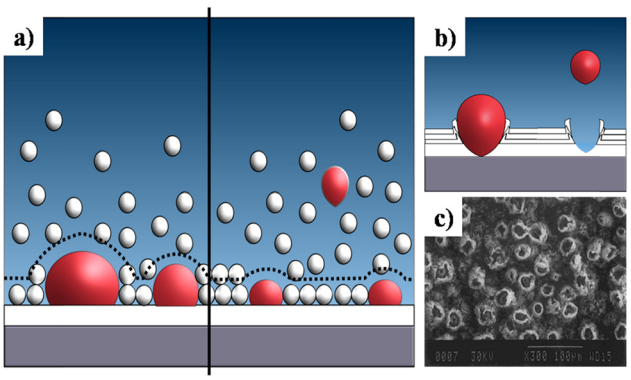

Fig. 13 (a) A schematic representation of the double layer distortion (represented with dotted lines) at ambient pressure (left) and reduced pressure (right) as a result of adhering gas bubbles (in red), (b) an illustration of the formation of volcano-like structures and (c) SEM of DCDP coatings with volcano-like growth under ambient pressure. Image (c) reprinted from ref. 266 with permission from Wiley.

sites. Consequently, this results in an uneven non-compact coating with porous volcano-like microstructures (illustrated in Fig. 13b). Upon lowering of electrolytic cell pressure to sub-atmospheric pressure, the gas bubbles were swiftly removed, accounting for the reduction in volcano-like structures.[151] As a consequence, the minimization of double layer distortion resulted in an improved coating with an enhanced adhesive strength as shown in Fig. 14. The increase in deposition potential coupled with the reduction in pressure enhances mass transport of Ca^{2+} and PO_4^{3-} ions thereby improving crystallinity and phase purity. Additionally, unlike the high pressure environment, this

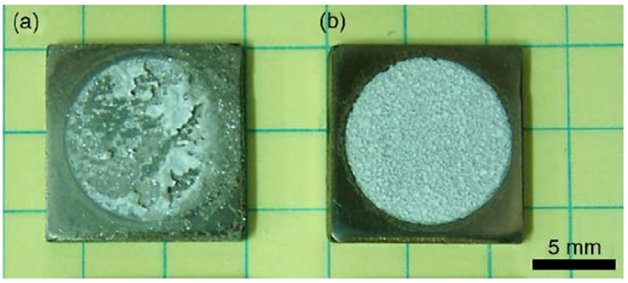

Fig. 14 The enhanced adhesive strength displayed by electrodeposited HAp specimens onto Ti_6Al_4V at (a) ambient pressure and (b) 80 Torr reduced pressure. Adapted from ref. 150 with permission from Elsevier.

experimental sub-atmospheric pressure resulted in enhanced crystal nucleation and growth ensuing uniform HAp coating over the electrodeposited substrate. The tunability of ambient pressure in an electrolytic system noticeably improves the nature of deposition in terms of mechanical stability and bonding strength to the substrate.

5.2.5.3. Effect of controlled atmosphere-assisted electrodeposition. Unlike the previous studies of employing low and high pressure in a closed electrolytic cell, the manipulation of crystal orientation *via* the control of the cell atmosphere has been reported by X. Lu and group.[152] Galvanostatic electrodeposition of HAp was performed on a Ti plate and the electrolytic setup was sealed and equipped for dynamic gas flow. The ambient atmospheres selected for this study were CO_2, N_2 and compressed air (comprising 78.08% N_2, 20.95% O_2 and 0.03% CO_2) with a dynamic flow rate of 1 L min^{-1}.

The controlled atmosphere facilitated manipulation of crystal orientation and phase purity. As shown in Fig. 15, the SEM micrographs indicate the formation of layered deposits of needle-like and plate-like coatings electrodeposited under N_2 and CO_2 atmospheres respectively. In a compressed air environment, comprising N_2 and CO_2, microstructural variations were observed with the progress in loading time with the coatings assuming a needle-like microstructure under a 30 min loading time with a gradual shift to a plate-like appearance beyond 30 min. The compressed air atmosphere resulted in the initial formation of phase-pure HAp needles. However, with the progress in loading time, the HAp gave way to the formation of OCP plates. This resulted in the coatings to be a HAp + OCP mixed phase with a mixed needle + flake microstructure under the controlled atmosphere of compressed air.

The results indicate that the crystal size and growth can be controlled by the ambient atmosphere within the electrolyte cell. Under a constant deposition rate, HAp crystals are much larger when electrodeposited in a CO_2 atmosphere than in a N_2 environment. The role of the cell atmosphere also accounts for pH variation within the electrolyte. The saturation of CO_2 provides for an acidic environment while N_2 gas shifts the pH towards alkalinity. The control over the ambient atmosphere serves as a modulating factor for pH and growth rate along with a consequential influence on the Ca/P ratio, rate of nucleation and topography. A CO_2 atmosphere resulted in crystal orientation along *a*,*b*-axes while a N_2 atmosphere oriented the crystal along the *c*-axis.

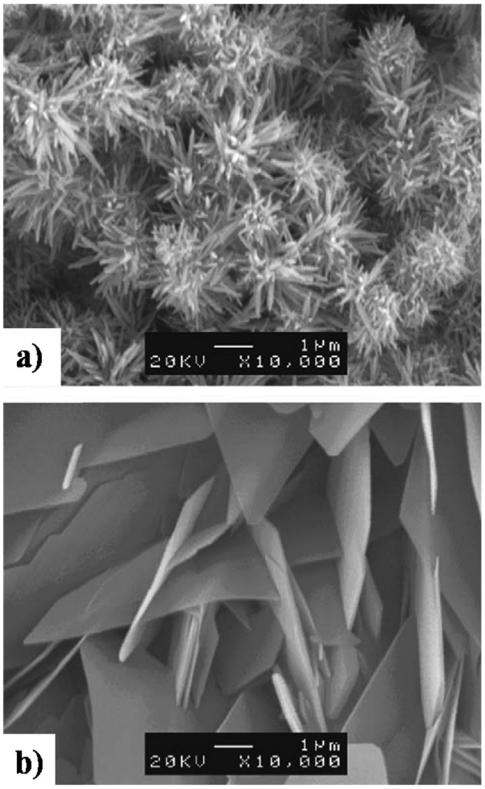

Fig. 15 SEM depicting the formation of (a) needle-like HAp in a N_2 atmosphere and (b) plate-like HAp in a CO_2 atmosphere electrodeposited under galvanostatic conditions. Adapted from ref. 152 with permission from Elsevier.

5.2.6. Influence of substrate modifications on nucleation and growth characteristics

5.2.6.1. Crystallinity of Ti and TiO_2 NT substrates. Electrodeposition of HAp onto Ti alters the growth rate based on the morphology and crystallinity of TiO_2 as investigated by Y. Parcharoen *et al.*[153] Herein, Ti foils were anodized to synthesize TiO_2 NTs of varying tube length. The electrodeposited HAp adhered with different capacities depending on the length of the NTs while larger diameters enhanced the formation and adhesion of the grown crystals. Another investigation by H. Tsuchiya *et al.*[154] considered the influence that the crystalline phase of TiO_2 NTs had on nucleation. An interesting observation is the indication of increased nucleation and formation of HAp over crystalline samples in comparison to amorphous TiO_2 NTs. Furthermore, a reduction in growth was seen for phase-pure anatase TiO_2 NTs in comparison to mixed anatase–rutile phase. This enhancement in nucleation rate for mixed anatase–rutile crystalline TiO_2 NTs may be due to variation in thermodynamic variables.

D. Gopi *et al.* performed a pulse electrodeposition of HAp onto HELCDEB treated Ti in a H_2O_2 environment.[155] The HAp crystals grown on the bare Ti substrate were flake-like while those on the HELCDEB surface treated Ti substrate nucleated as rods in a lotus-like fashion with an indicative lowered (002) plane. F. S. Utku *et al.* studied the effects of pulses and electrolytic temperature on the Ca/P chemistry of HAp deposits

grown over a normal Ti plate and TiO_2 substrates anodized in the presence and absence of F^- ions.[156] The investigation revealed that the deposits were plate-like in the case of the Ti plate with preferred crystal orientation along the (300) plane. However, the anodized TiO_2 NTs both had varying sizes of needle-like crystals depending on the electrolyte temperature with varying magnitudes of the Ca/P ratio. The use of anodized and non-anodized Ti substrates indicated the control over crystal growth and orientation in a bipolar pulsed galvanodynamic mode.

5.2.6.2. Functionalized carbon substrates. HAp has been reported to have been coupled successfully to MWCNTs, graphene and reduced graphene-metallic substrates.[157–159] These serve the purpose of improving mechanical and adhesive strength, as biocompatible fillers with anti-microbial properties and acting as a selective gateway for various ionic species. Additionally, their influence on growth of electrodeposited HAp in terms of porosity, hydrophilicity and morphology is enhanced.

The morphological improvement of electrodeposited HAp, reported in ref. 160, is carried out potentiostatically over anodized TiO_2 NTs (Fig. 16a) with the resulting microstructure resembling flakes with a Ca/P ratio of 1.5 (Fig. 16b). However, the formation of HAp carried out in the presence of –COOH functionalized MWCNTs resulted in a homogeneous foam-like appearance with a Ca/P ratio of 1.6 (shown in Fig. 16c). This foam-like HAp coating grown over the substrate witnessed an increase in porosity which facilitates an enhanced migratory transport of ions within the composite coating *via* its micro- and macro-porous channels. Another relatable improvement can be witnessed in micro-hardness upon incorporation of MWCNTs with a decrease in contact angle signifying the hydrophilic nature of the coatings.

Z. Leilei investigated the galvanostatic electrodeposition of HAp onto a carbon nanotube/nanofiber hybrid template with ultrasound assistance.[161] The carbon nanotubes grew radially to the carbon nanofiber template. Subsequently, this was employed as a template for the deposition process. The carbon nanotubes maintained a straight and porous network (Fig. 17a) with gaps ranging from 1 to 10 μm. The HAp deposited network over carbon nanotubes and carbonated carbon nanofibers can be seen in Fig. 17b and c respectively. The deposits over carbon nanotubes have evolved into a particle shaped HAp while the carbon fibers are coated with a plate-like HAp with size ranging from 20 to 50 μm. The control over microstructure can prove effective in the tunability of the crystal orientation and the microstructure, depending on the electrode modifications employed.

5.2.6.3. Nafion-Ni foam substrate. Q. Zhang *et al.* fabricated a Ni foam/HAp composite by employing Nafion-assisted electrodeposition.[162] Herein, Nafion plays the role of an electrolytic membrane facilitating high proton conductivity and no anion uptake and exhibits excellent physico-chemical durability. The experimental protocol reported involves Nafion being used as a template for electrodeposition of HAp crystals. As shown in Fig. 18a, a bare Ni foam resulted in hexagonal needle-like HAp microstructures with coating thickness ranging from 10 to 15 μm. However, the incorporation of Nafion to the Ni foam substrate stimulated the growth of a 3D morphology comprised of a mixture of needles with agglomerates of spherical HAp (Fig. 18b). Every individual sphere comprised of needle-like nanocrystals 100 nm in length with an overall spherical diameter of 300 nm. An intense (002) peak signifies the favored directional growth along the *c*-axis.

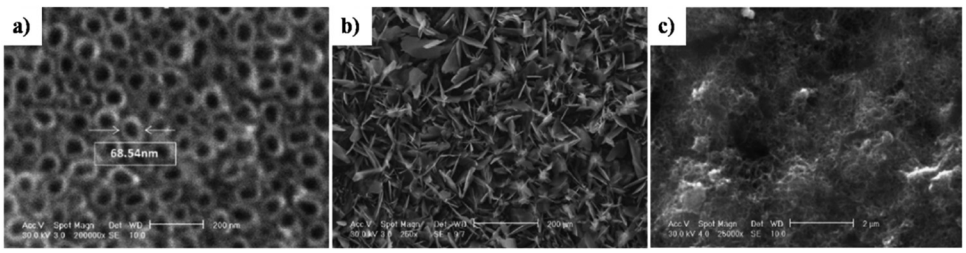

Fig. 16 SEM images depicting the microstructural variation in HAp coating electrodeposited over TiO_2 NT and –COOH functionalized MWCNT/TiO_2 NT substrates: (a) TiO_2 NTs, (b) HAp/TiO_2 NT nanocomposite and (c) HAp/MWCNT/TiO_2 NT nanocomposite. Adapted and rearranged from ref. 160 with permission from Elsevier.

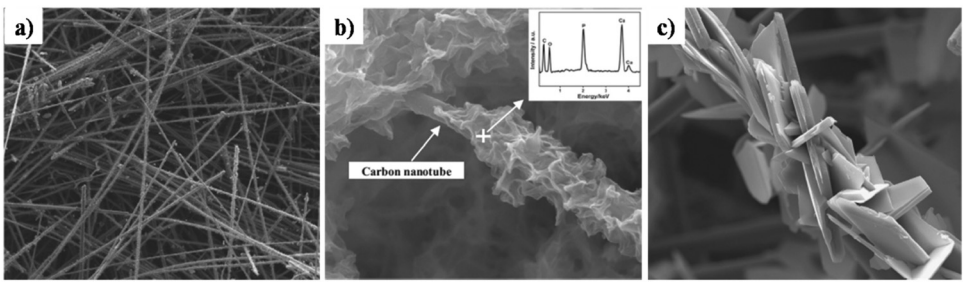

Fig. 17 SEM of (a) carbon nanotubes, (b) carbonated HAp electrodeposited over carbon nanotubes and (c) carbonated HAp deposited over carbon fibers. Adapted from ref. 161 with permission from Elsevier.

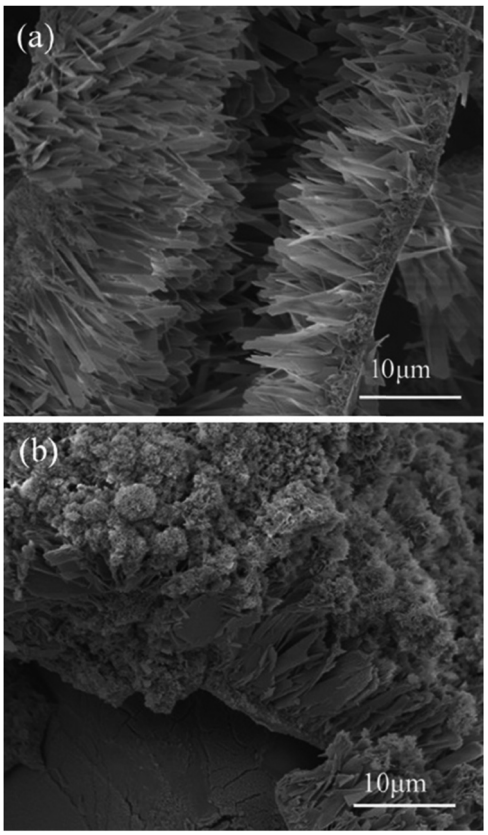

Fig. 18 Cross-sectional SEM of HAp electrodeposited over (a) Ni foam and (b) Nafion coated Ni foam. Adapted from ref. 162 with permission from Elsevier.

The composite witnessed an increase in the degree of crystallinity from 85.27% to 91.57% upon inclusion of Nafion onto the substrate. The Nafion membrane is speculated to facilitate an optimized distribution of OH^- ions near the cathode surface thereby being conducive to the formation of a layered topography with enhanced crystallinity.

5.2.6.4. Cation exchange membrane-assisted electrodeposition. A unique tubular shaped HAp was synthesized *via* the method of cation exchange membrane-assisted electrodeposition.[163,164] The conceptual design of the experiment involves two glass containers separated by a Nafion N-117 membrane, with the Ca^{2+} and PO_4^{3-} precursor in each container. Electrical contact is supplied through two electrodes, one placed in each electrolytic cell. When an applied potential is introduced, the Ca^{2+} ions penetrate through the exchange membrane towards the PO_4^{3-} rich side. The formation of HAp occurs directly on the Nafion membrane. Upon completion, the Nafion membrane is carefully rinsed and dried and the tubular HAp powder is collected from the membrane. The peculiarity of this technique is that the HAp electrodeposition does not occur on any metallic working electrode but instead on the Nafion membrane. Since the driving force for the ions through the membrane is the applied potential, it is coined as cation exchange membrane-assisted electrodeposition. With a phase constitution of HAp,

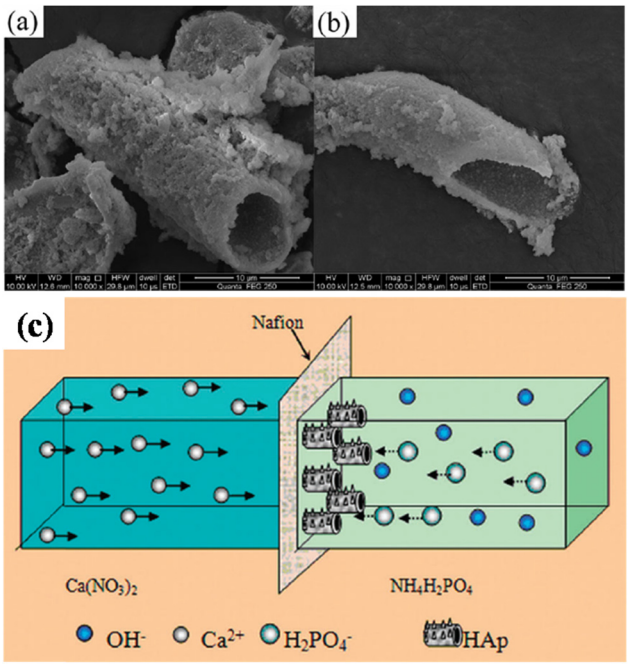

Fig. 19 (a and b) SEM of tubular shaped HAp synthesized *via* the cation exchange membrane-assisted electrodeposition technique and (c) the schematic illustration of the formation of tubular HAp. Images (a) and (b) adapted from ref. 163 and image (c) reproduced from ref. 164 with permission from Royal Society of Chemistry.

the preferred crystal orientation was along the (002) plane, *i.e.* the exposed *c*-axis. The growth mechanism of the tubular structures is reported to occur at the bottom, closer to the exchange membrane, and in some ways, it resembles an extrusion process. The tubular HAp microstructures and schematic regarding the growth of hollow tubular shaped HAp are depicted in Fig. 19. The formation of tubular HAp supports the hypothesis of growth occurring near the Nafion membrane as the Ca^{2+} ions diffuse through. It is speculated that the HAp crystals grow preferentially orienting along the *c*-axis to form nanosheets and then roll up to form tubular HAp to reduce surface energy.

5.2.6.5. Template-assisted electrodeposition. S. Beaufils *et al.* employed a template-assisted electrodeposition approach towards the synthesis of HAp nanotubes and nanowires as powders.[165] Deposition of HAp was performed in a three-electrode setup wherein the working electrode was a track-etched polycarbonate membrane with one side sputtered with 300 nm gold film for conductivity (shown in Fig. 20a). The morphology of the nanotubes and nanowires grown *via* this method can be seen in Fig. 20b and c respectively. The electrodeposition of HAp was examined *via* both potentiostatic and applied pulsed modes. H_2O_2 was added to minimize the formation of H_2 bubbles which may otherwise disrupt the ionic diffusion process and block the pores of the etched polycarbonate template. The template was dissolved in dichloromethane upon completion of electrodeposition. By varying the membrane pore diameter and controlling the deposition parameters, the thickness of the needles and nanotubes can be controlled thereby altering the aspect ratio between 19 and 71 for

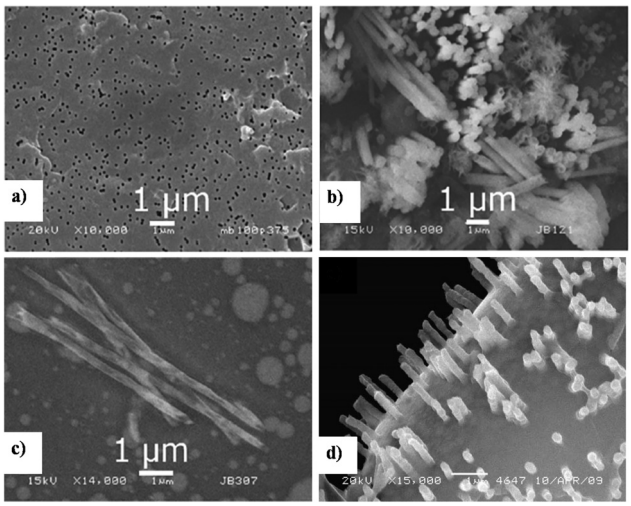

Fig. 20 FESEM of (a) the 100 nm porous polycarbonate membrane template and template-assisted electrodeposited microstructures of (b) HAp nanotubes and nanowires deposited under constant potential and (c) HAp nanowires deposited under pulsed mode. (d) SEM of HAp nanowire nanoarrays electrodeposited onto GCE *via* template-assisted electrodeposition. Images (a), (b), and (c) adapted from ref. 165 and image (d) adapted from ref. 229 with permission from Elsevier.

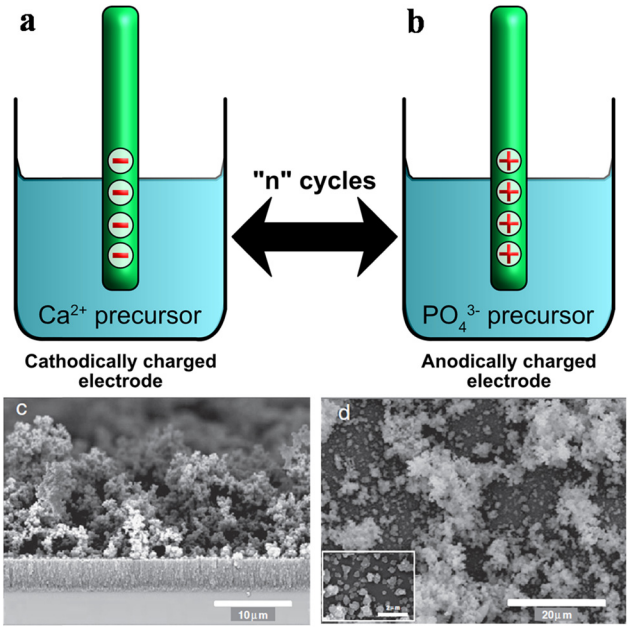

Fig. 21 Schematic representation of the technique of cyclic electrodeposition where the electrode is alternatively immersed in precursor solution under galvanostatic conditions. (c) Cross-sectional and (d) topographical FESEM of agglomerated HAp spheres synthesized *via* cyclic electrodeposition. Images (c) and (d) adapted from ref. 167 with permission from Elsevier.

nanowires. The aspect ratio for HAp nanotubes varied between 9 and 25 with high specific surface area. The Ca/P ratio of the HAp crystals fabricated *via* pulsed template-assisted electrodeposition was ~1.5. The growth orientation of the nanowires and nanoneedles was along the *c*-axis while the predominantly exposed HAp facet indicated an increase in the *a*,*b*-plane during the application of pulses. Compared to the growth of HAp nanotubes *via* the cation exchange membrane-assisted electrodeposition, the approach of template-assisted electrodeposition facilitates the fabrication of HAp nanotubes and nanowires of controlled morphological homogeneity.

5.2.7. Cyclic electrodeposition. Cyclic electrodeposition involves fabrication of coatings of calcium phosphate, wherein the Ca and P species are deposited in alternating cycles. The cyclic electrodeposition method was investigated by J. Hernández-Montelongo *et al.* wherein the technique proved advantageous in the synthesis of specific phases of calcium phosphates with controlled Ca/P ratio.[166,167] The technique of cyclic electrodeposition amalgamates the process of immersion with electrodeposition with the mechanistic principle being analogous to that of atomic layer deposition. The experimental setup involved porous silicon as the working electrode with the Ca and P electrolytic precursors being 0.1 M solutions of $CaCl_2$: EtOH (2 : 1) at pH 5.5 and Na_3PO_4 : EtOH (2 : 1) at pH 7.2 respectively. The working electrode was polarized at 1 mA cm^{-2} of cathodic current density when immersed in the Ca^{2+} electrolytic precursor followed by immersion in PO_4^{3-} solution with an anodic current density of 1 mA cm^{-2} for a total of 20 cycles, 30 s each. Note that this technique does not incorporate a counter electrode. Instead, the polarity of the working electrode is reversed alternatively, wherein the porous silicon substrate is negatively charged when immersed in the Ca^{2+} solution and positively charged when immersed in the PO_4^{3-} precursor (Fig. 21a and b). This alternating cyclic immersion incorporates a cyclic change in overall charge density over the substrate resulting in a heterogeneous coating of electrocrystallized HAp with isolated agglomerates (Fig. 21c and d). The density and size of the HAp clusters over the substrate witnessed an enhancement with the increase in the number of immersion cycles. The agglomerated HAp comprised spherical nanoparticles with a predominant crystal facet along the *a*,*b*-plane.

6. Sensing applications of HAp

Sensors enable the quantification of physical and chemical changes occurring in our environment, ranging from biological and biomedical changes for human health and patient care,[168–170] to chemical quantification of environmental pollutants and their remediation.[171,172] The detection of gaseous components from industrial and manufacturing processes,[173,174] and use as biosensors for glucose, peroxidase and protein estimation[175–178] are some of the incredible applications of sensors. The materials constituting a sensor can include semiconductor metal oxides[179–182] and carbon-based materials[183,184] with functionality ranging from mechanical stimuli[185–191] to environmental monitoring.[192,193]

The quantitative detection and sensing of gaseous pollutants is vital in the industrial and manufacturing arena to safeguard human health. Emission control of hazardous substances can be realized *via* sensors. The detection of gaseous components generally occurs either by chemical interaction with surface active sites or through physisorption onto the sensing material. This interaction results in variations over surface charge distribution

that can be measured electrochemically. Depending on the technique, the detection of the analyte can be resolved *via* change in resistance, impedance, capacitance and amperometry among other measurement systems. Among the myriad detection methods for chemical sensing, resistance-based sensing is the simplest. The common environmental gaseous pollutants that require rapid detection and response include CO, CO_2, SO_2, NH_3, water vapor, NO_x and VOCs, to name a few.

6.1. HAp composites towards detection of gaseous analytes

The unique property of the presence of surface active sites of crystalline HAp, *viz.* *a*,*b*-plane and *c*-plane, facilitates its sensing behavior towards gases and solvated ions. The crystal facets of hexagonal HAp comprise of acidic and basic sites thereby ensuring versatility towards the detection of these gases. The application of HAp in the field of gas sensing can attributed to its porosity, surface groups along the *a*,*b*-plane and *c*-plane and its ion exchange capability. The drawback of phase-pure HAp as a sensing material encompasses a low response time, high operating temperatures and selectivity towards acidic and basic gas molecules. To mitigate this, a sensor is generally activated through the incorporation of dopants resulting in binary and ternary composites so as to provide a framework and serve as a means for recording the variation in charge carrier density occurring from the analyte interaction over the active material. By modifying the physico-chemical properties of HAp with additives, dopants and microstructural and crystalline modifications, one may enhance the interaction of HAp towards ionic species.

The technical detection of any analyte species can be performed in either static or dynamic environments. A dynamic environment takes into consideration the gas flow rate while ensuring the safety protocol involved in venting out the gas after measurement. However, we will limit our discussion to the static mode of gas sensing. The percentage sensitivity of a sensor towards the target gas can be determined *via* resistance-based measurements and is calculated from the relation

$$\%S = \frac{R_a - R_g}{R_a} \times 100 \quad (15)$$

where R_a and R_g denote the resistance offered by the sensor material in carrier gas and target gas respectively. The carrier gas typically used during sensing is an inert gas such as argon. The volume of target gas injected into the test chamber may be quantified by the relation[163]

$$Q = \left(\frac{V \times C \times M}{22.4 \times d \times \rho}\right) \times 10^{-9} \times \frac{(273 + T_R)}{(273 + T_B)} \quad (16)$$

where V is the volume of the test chamber, C is the concentration of target gas in ppm, M is the molecular weight in *g*, d is the density of target gas (g cm^{-3}) and ρ is the purity of target gas. T_R and T_B represent the temperature of the test environment and the test chamber respectively.

Gas sensing depends on the change in resistance induced during adsorption and desorption of the analyte species. Gases with functional groups ($-NH_2$, $-C_6H_5$, $-C{=}O$) exhibit higher response upon interaction with HAp. The mechanism of detection based on HAp can be related to the density and migration of the charge carriers across the surface crystal lattice. At room temperature, it is reported that protons (H^+) are the major charge carriers on HAp.[163] The proton may migrate from one OH^- to the adjacent OH^- or PO_4^{3-} groups on the P-site. If the growth orientation is predominant along the *c*-plane, the amount of ionic channels is enhanced thereby facilitating rapid adsorption and improved conductivity. With H^+ being the charge carrier on HAp at room temperature, an increase in H^+ concentration witnesses an increase in resistance. For a migrating proton between two adjacent OH^- groups, the interaction may be related as

$$2OH^- \rightarrow O^{2-} + H_2O \quad (17)$$

Additionally, the migration or transfer of H^+ can take place between adjacent OH^- and PO_4^{3-} groups. Both cases result in the formation of O^{2-} species.

This section will focus on the aspect of sensing behavior in relation to the exposed and active crystal facet of hexagonal HAp nanocomposites. Additionally, the mechanism involved in the detection of each analyte is presented. The added benefits of porosity and surface acidity/basicity facilitate detection through increased density of active sites. Table 6 outlines the sensor material, its working temperature at maximum % sensitivity, response–recovery time and the predominantly exposed crystal facet.

6.1.1. Detection of NH_3. NH_3 poses a serious health risk as an irritant to the eyes and respiratory tract. The recommended human safety level of the gas is set at a limit of 25 ppm at exposures of about 8 h with a short term exposure being 15 min at 35 ppm.[194] Multiple reports on HAp nanocomposites have reported them to exhibit effective sensing characteristics towards NH_3 gas. Being a reducing gas, NH_3 is electron donating in nature. For its effective sensing *via* resistance-based measurements, the utilization of p-type substrates would better facilitate electrochemical measurements, since the major charge carriers in p-type materials are holes or vacancies.

L. Huixia *et al.* reported the development of an effective NH_3 sensor based on HAp composited with conducting polymers such as PANI and PPy.[194] PANI and PPy polymers are p-type semiconductors. Tubular HAp microstructures were fabricated *via* the cation exchange membrane-assisted electrodeposition technique. The composites were prepared by mechanical mixing, and electrical measurements for gas sensing efficacy were recorded at room temperature under static conditions. As previously discussed (in Section 5.2.6.4), tubular HAp synthesized on the exchange membrane exhibited preferential crystal orientation along the *c*-plane with high specific surface area. The maximum sensitivity was displayed by 5% PPy/HAp and 20% PANI/HAp composites at NH_3 concentrations of 1000 ppm and 500 ppm respectively. When compared to pure HAp, the response/recovery time of PANI and PPy nanocomposites was lower. However, lower detectable limits improved in conducting polymer composites. The selectivity towards NH_3 was determined along with four interfering VOCs and the selectivity coefficient was calculated as

$$K_{A/B} = \frac{S_A}{S_B} \quad (18)$$

Table 6 Reported HAp nanocomposites in the field of gas sensing and their response characteristics

S. No.	Sensor	Analyte gas	Working temperature (°C)	Optimum concentration (ppm)	Sensitivity (%)	Response/ recovery time (s)	Dominant HAp crystal facet	Ref.
1	Tubular HAp	NH_3	RT	2000	84.58	10/180	*c*-Plane	163
2	PANI/tubular HAp	NH_3	RT	500	85.0	—/—	*c*-Plane	194
3	PPy/tubular HAp	NH_3	RT	1000	90.7	—/—	*c*-Plane	194
4	Au/tubular HAp	NH_3	RT	200	86.7	20/25	*c*-Plane	196
5	Graphene doped HAp	NH_3	RT	50	54.0	—/—	*a*,*b*-Plane	195
6	HAp/cellulose nanofiber	NH_3	25	5	575	210/30	—	197
7	Tubular HAp	H_2S	RT	2000	31.2	—/—	*a*,*b*-Plane	200
	Acidithiobacillus ferrooxidans incorporated tubular HAp	H_2S	RT	2000	76.0	—/—	*a*,*b*-Plane	
8	Tubular HAp	Acetone	RT	1000	~60	63/31	*c*-Plane	163
		n-Hexane			~46	25/40		
		Styrene			~50	40/139		
9	Graphene doped HAp	Acetone	RT	500	35.7	—/—	*a*,*b*-Plane	195
		Methanol			41.6	—/—		
		THF			35.5	—/—		
10	CNT doped HAp	Ethanol	RT	100	600	90/120	*c*-Plane	207
11	CNT doped HAp	Methanol	30	100	~600	60/—	*c*-Plane	263
12	HAp-TiO_2	Methanol	33	10	225	50/20	*a*,*b*-Plane	204
		Ethanol	35		190	170/20		
		Propanol	55		192	100/70		
13	Graphite doped HAp	Methanol	30	100	465	90/180	*c*-Plane	205
		Ethanol	30		333	110/200		
		Propanol	60		352	60/—		
14	HAp	CO	195	1000	45	35/25	*c*-Plane	219
	Co-HAp		150		135	~25/~20		
	Fe-HAp		140		91	30/40		
15	SWI HAp	CO	195	1000	210	20/25	*c*-Plane	264
16	SWI Co-HAp	CO	150	1000	220	20/~20	*c*-Plane	218
17	SWI Fe-HAp	CO	140	1000	250	~20/25	*c*-Plane	217
18	HAp-$BaTiO_3$	CO	175	1000	78	—/—	*c*-Plane	219
19	HAp-TiO_2	CO	185	1000	60	—/—	*c*-Plane	219
20	0.05 wt% CNT-HAp	CO	105	20	130	48/62	*a*,*b*-Plane	221
21	HAp	CO_2	165	1000	31	20/15	*a*,*b*-Plane	216
	Co-HAp		135		75	35/45		
22	SWI Co-HAp	CO_2	135	1000	156	25/30	*c*-Plane	218
23	Fe-HAp	CO_2	155	1000	112	30/40	*c*-Plane	215
24	SWI Fe-HAp	CO_2	155	1000	290	15/20	*c*-Plane	217
25	0.1 wt% CNT-HAp	CO_2	70	20	200	70/35	*a*,*b*-Plane	220

where S_A and S_B are sensitivity of the sensor towards target gas A and interference gas B.

Additional reports involving HAp doped with graphene,[195] Au[196] and cellulose nanofibers[197,198] revealed varying levels of sensitivity towards NH_3 with the measured values tabulated in Table 6. Interestingly, the predominant crystal orientation of HAp in most reports was along the *c*-plane with the exception of the report in ref. 195 wherein the graphene doped HAp has its HAp crystals oriented along the *a*,*b*-plane (based on XRD interpretation) resulting in a reduced sensitivity of 54%. The HAp blended cellulose nanofibers exhibited 575% sensitivity towards 5 ppm NH_3, mainly attributed to the content, distribution, specific surface area and pore density of the HAp particles blended with cellulose. The HAp/cellulose nanofibrils formed a dense net-like structure with a HAp Ca/P ratio for all nanocomposites ranging from ~2.35 and 2.66. NH_3, a polar molecule, has a likelihood of interacting with the physisorbed surface H_2O molecules. The cellulose-based composites exhibited enhanced conductivity and sensitivity that can be attributed to the H-bonding affinity between NH_3 and the –OH groups present on the six-membered polysaccharide.

The sensing mechanism of HAp towards NH_3 can be explained in terms of proton exchange and conductivity occurring during the adsorptive interaction between the analyte gas and the adsorbed H_2O molecules. HAp behaves as an n-type semiconductor whose resistance decreases upon exposure to ammonia.[194] Furthermore, HAp is a well-known hydrophilic biopolymer with the H_2O molecules being adsorbed onto the –OH groups present along the *c*-axis. The adsorbed H_2O assists in the formation of a hydrogen bond with the NH_3 molecule.[199] This interaction results in the possible conversion of adsorbed NH_3 to NH_4^+, expressed as

$$NH_{3(g)} + H_2O_{(ads)} \leftrightharpoons NH_4^+{}_{(ads)} + OH^-{}_{(ads)} \quad (19)$$

The proton shift creates a variation in the resistance of the sensor. The response curve increases linearly indicating the formation of a unimolecular layer of adsorbed gas. Due to the room temperature study, the recovery time of the sensor was delayed due to the slow desorption of NH_3 from the active

sites. The capture and dissociation of NH_3 gas can be expressed *via* an alternate mechanism[163] wherein the NH_3 molecule loses a proton to form NH_2^- which in turn converts to NO_x^{n-}.

$$NH_3 \leftrightharpoons NH_2^- + H^+ \quad (20)$$

$$NH_2^- + O_2^- \leftrightharpoons NO_x^{n-} + H_2O \quad (21)$$

In eqn (20), the H^+ liberated increases the overall density of charge carriers over HAp resulting in resistance variation. On the other hand, the formation of NO_x^{n-} may substitute the anionic species in the crystal lattice thereby inducing a change in conductivity. The exposed *c*-plane of HAp has a higher density of OH^- and PO_4^{3-} groups resulting in an effective one-dimensional charge carrier phenomenon along the *c*-axis.[194]

6.1.2. Detection of H_2S. H_2S is a flammable and acidic gas found at toxic levels in coal mines, natural gas production fields and petroleum fields causing extreme environmental and human problems. The safety threshold limit for H_2S is 10 ppm for 8 h, with higher concentration of 250 ppm being hazardous making early detection crucial. Y. Tan *et al.* investigated a sensor comprised of a Gram-negative bacterium, *Acidithiobacillus ferrooxidans*, mixed with HAp to improve its sensitivity towards H_2S gas.[200] The microstructure of HAp was tubular and was fabricated through the cation exchange membrane-assisted electrochemical deposition technique. This was then composited with *Acidithiobacillus ferrooxidans* and coated onto a ceramic tube to prepare the sensor. The tubular microstructure of HAp facilitates an increase in the surface to volume ratio with increased density of active sites for enhanced adsorption of H_2S. The adsorptive interaction involves formation of hydrogen bonding with the existing surface adsorbed H_2O. As discussed, protons are the major charge carriers in HAp. The (002) plane is prone to adsorption of H_2O through hydrogen bonding. The interaction of H_2S with adsorbed H_2O takes place as

$$H_2S_{(g)} + H_2O_{(ads)} \rightarrow HS^- + H_3O^+ \quad (22)$$

The formation of HS^- increases the density of H^+ over the composite attributing to a change in resistance. *Acidithiobacillus ferrooxidans*, known for its oxidative property of converting sulfur compounds into energy, promotes the sensing characteristics even further due to the presence of jarosite (consisting of Fe^{3+} and OH^-).[200] The limit of detection of the biocomposite was significantly enhanced in relation to pure HAp. The highest sensitivity of the composite towards H_2S was 76% at 2000 ppm which is 2.5 times higher than the response from pure HAp. With the major crystal orientation aligning towards the (002) plane, the tubular HAp indicates excellent viability towards H_2S sensing.

6.1.3. Detection of NO_x. A. Mitsionis *et al.* reported on the interaction of the HAp/TiO_2 composite with NO in a controlled photocatalytic NO oxidation application.[201] Herein, biphasic nanocomposite powders of c/TiO_2 were prepared *via* precipitation with varied specific surface area and active site. The selective oxidative capability of the composite towards NO was studied over a two-step oxidation process towards NO_x generation. It has been reported that HAp possesses ~2.6 P–OH groups per nm with selective adsorption towards CO_2, CH_3OH, H_2O, pyridine, acetic acid and *n*-butylamine.[202] It is reported that HAp, when exposed to UV light, generates oxygen vacancies and that the $O_2^{\bullet -}$ radicals are a result of the electrons being trapped within these vacancies. The interaction and subsequent oxidation of NO to NO_2 over the HAp/TiO_2 composite are given as

$$O_2 + e^- \rightarrow O_2^{\bullet -} \quad (23)$$

$$NO + O_2^{\bullet -} \rightarrow NO_2 + O^- \quad (24)$$

$$NO_2 + O^- \rightarrow NO_3^- \quad (25)$$

The electron transfer to the $O_2^{\bullet -}$ radical facilitates a two-step NO oxidation process. When the HAp/TiO_2 ratio increased from 1 to 10, the N_2 adsorption desorption studies revealed an increase in specific surface area from an initial 55.4 $m^2\ g^{-1}$ to 101.1 $m^2\ g^{-1}$. The XRD profiles indicate the predominance of the (002) plane in HAp/TiO_2 with a needle-like microstructure orienting along the (001) direction. This indicates the possibility of modification of the surface area of the *c*-plane towards NO oxidation and may be further extrapolated to sensing and detection of NO_x species.

6.1.4. Detection of VOCs. Alcohol and other VOCs persist in everyday products as organic solvents in dyes, perfumes and in manufacturing sectors. These VOCs, being toxic compounds, affect air quality even at ppb levels.[203] Furthermore, the increasing demand for the fabrication of next generation fuels in fuel production units makes it imperative to maintain a working environment with a focus on human health and safety. Mild concentrations of methanol can be fatal while ethanol is an irritant and a hypnotic.[204] Additionally, the volatility and flammability of VOCs makes it critical to develop VOC sensor materials.[205] HAp has been reported to be employed in the detection of VOCs and its sensing characteristics towards VOCs can be found in Table 6.

As per reports in ref. 163, tubular HAp, synthesized *via* cation exchange membrane-assisted electrodeposition, was employed in VOC sensing. The tubular HAp showed a larger response towards VOCs than hydrothermally prepared HAp. The maximum % sensitivity at room temperature towards 1000 ppm of acetone, *n*-hexane and styrene was 60%, 46% and 50% respectively. As already discussed, the tubular HAp prepared *via* the cation membrane-assisted electrodeposition technique had maximum crystal orientation predominating along the *c*-plane. However, compared to pure HAp, the presence of additives significantly altered the sensitivity levels of the composite towards VOC detection. S. R. Anjum *et al.* developed a graphite doped HAp selective alcohol sensor.[205] The choice of graphite as a dopant lies in its capability of facile sorption/desorption of incoming gas molecules. The ideal adsorption/desorption behavior can be attributed to the weak dispersive forces towards gas molecules. XRD profiles reveal that the HAp crystals were hexagonal both before and after graphitic doping with a maximum intensity along the (002) plane, indicating predominantly *c*-plane oriented crystals. The total pore volume

increased by a factor of ~2 upon addition of graphite, from 0.087 cc g^{-1} (pristine HAp) to 0.201 cc g^{-1} (after doping). The analyte VOCs detected were 100 ppm methanol, ethanol and propanol. The sensitivity of pure HAp was 100%, 92% and 180% towards methanol, ethanol and propanol respectively, whereas 0.5 wt% graphite doped HAp possessed a sensing efficacy up to 465%, 333% and 352% respectively. It was witnessed that as the carbon chain length in the alcohol moiety increased, the adsorptive interaction and subsequent sensing capabilities of the sensor improved with the increase in thermal energy. As reported in ref. 205, sensing of propanol improves at an operating temperature of 60 °C, while for methanol and ethanol, the optimum temperature for maximum % sensitivity is 30 °C (shown in Table 6). Alcohols being reducing species with electron donating properties tend to increase the number of liberated electrons depending on the carbon chain length.[205]

The mechanism describing the interaction of HAp towards VOCs has been detailed in ref. 163 and 205. The exposure of HAp crystals to VOCs results in the adsorption and dissociation of the molecule *via* the loss of H^+.

$$C_xH_yO_z \leftrightharpoons C_xH_{y-n}O^{n-} + nH^+ \quad (26)$$

Upon dissociation, the resultant deprotonated VOC species reacts with the surface O_2^-, O^- and O^{2-} groups to form CO_2 and H_2O. An electron is liberated in the process.

$$C_xH_{y-n}O^{n-} + O^{2-} \leftrightharpoons CO_2 + H_2O + e^- \quad (27)$$

The conversion of methanol to CO_2 is as below:

$$CH_3OH + 3O^{2-} \rightarrow CO_2 + 2H_2O + e^- \quad (28)$$

The generated electron from alcohol dissociation may be harnessed for sensing when HAp is either deposited or doped onto TiO_2, CNTs or graphitic-based substrates. TiO_2 is an n-type semiconductor with electrons as the major charge carrier. By employing TiO_2-HAp composites for VOC sensing, the sensitivity of the sensor towards VOCs is enhanced.[204,206] The use of CNTs in sensing is largely attributed to high surface-to-volume ratio resulting in an increase in the density of active sites. At room temperature, CNTs behave as a p-type semiconductor wherein the π-electronic orbitals facilitate charge transport and conduction through the substrate.[207] The addition of graphite to the sensor increases the response time due to graphite acting as an electron sink.[205] Additionally, the planar structure along with the presence of sp^2 hybridized carbon active sites enhances the applicability of graphite and its derivatives in the field of sensing.

Furthermore, there exists the possibility of interaction of the CO_2 gas with the OH^- surface species along the *c*-plane. This may result in the formation of CO_3^{2-} and its substitution within the lattice groups thus forming carbonated HAp.

$$CO_2 + 2OH^- \leftrightharpoons CO_3^{2-} + H_2O \quad (29)$$

HAp conducts *via* the transfer of a proton at low temperatures. The proton formed *via* VOC dissociation may migrate between two adjacent OH^- or PO_4^{3-} anions. The diffusion pathway of the proton along the *c*-plane is higher than along the *a*,*b*-plane.[208] At elevated temperatures, the electrical conduction in HAp is facilitated by the presence of H^+ and OH^- surface ions. However, at low temperatures, conduction is attributed to the transfer of a proton, either between two neighboring OH^- groups or *via* transfer between adjacent OH^- and PO_4^{3-} ions (eqn (17)). This proton conduction is poor at low temperature and can be augmented with favorable additives such as carbon-based moieties from the graphite family, metal oxides and carbon NTs. These additives enhance the mechanistic pathway for improved sensing through their outstanding structural, chemical, and electrical properties.

6.1.5. Detection of LPG. LPG is an explosive gas comprised of a mixture of hydrocarbons predominantly used as fuel. Vapors of LPG are known to induce breathing and health issues wherein OSHA has recommended an exposure limit to 1000 ppm for 8 h. The calibrated LEL is determined to be 1.8% for butane and 2.1% for propane, both components present in LPG. This lower exposure limit necessitates the rapid detection and response towards prevention of fire accidents. Avinashi *et al.* reported the fabrication of a LPG sensor comprised of the Na-doped HAp/Al_2O_3 composite spin coated over a glass substrate.[209] Pristine Na-doped HAp measured its highest sensitivity at 683.18% (2 vol% LPG) with a delayed response and recovery time of 89 s and 22 s respectively. This prolonged detection is not ideally applicable in the rapid sensing of LPG. The incorporation of Al_2O_3 reduced the response and recovery time to 4 s and 3 s respectively with a sacrifice in sensitivity of 34.27% at 0.5 vol% LPG.

The mechanism involved in the detection of LPG is reported as follows:

$$C_nH_{2n+2} + O_2^- \rightarrow C_nH_{2n}O + H_2O + e^- \quad (30)$$

The aliphatic hydrocarbons of LPG interact with ionic oxygen species over the surface of HAp resulting in oxidized species and a liberated electron. This change in the density of electrons over the sensor substrate is reflected in the variation in resistance thereby enabling the HAp composite to act as a viable LPG sensor for commercial use.

6.1.6. Detection of CO and CO_2. The detection of CO and CO_2 gases with HAp nanocomposites has been explored in multiple reports. The ease of ionic substitution of CO_3^{2-} with the lattice PO_4^{3-} groups has been explained wherein the incorporation of the CO_2^+ ion within the HAp crystal lattice witnesses a decreased intensity of the (002) *c*-plane with peak broadening indicating reduction in crystallinity. This CO_2^+ ion interaction occurs with the surface PO_4^{3-} and OH^- groups found along the (002) plane resulting in the eventual formation of carbonated HAp.[210] Surface P–OH groups serve as active sites for the adsorption of H_2O, CO_2, alcohol and CH_3I. T. Ishikawa *et al.* investigated the adsorption of CO_2 as a function of calcium deficiency.[211] It was determined that the CO_2 gas was irreversibly adsorbed, depending on the non-stoichiometry. The particles were rod-like at 100% Ca-rich HAp and acicular as the Ca^{2+} content decreased. The *a*,*b*-plane is basic in nature from the Ca^{2+} ions. Chlorinated HAp was synthesized *via* the chemical precipitation technique and employed as a CO_2 gas

sensor.[212] The Cl^- anion incorporated within the crystal lattice increased the length of the *a*,*b*-plane thus reducing the strain caused by CO_3^{2-} substitution at lower temperature thus promoting reversible substitution. The substituted particles were spherical. A decrease in current is attributed to the reduction in the density of charge carriers upon exposure to CO_2 gas.[213]

A significantly low response–recovery time towards CO_2 gas was characteristic for pristine HAp with the predominant crystal orientation being the *a*,*b*-plane. The % sensitivity was indicated to be ~31% due to reduced interaction along the exposed (300) facet.[214] In order to mitigate the low levels of sensitivity, metallic dopants such as Fe and Co were added to HAp thereby witnessing a substantial increase in the response of the sensor film.[215,216] In the case of Fe-doped HAp, it was determined that the microstructure of the composite varied from granular to plate-like up to an Fe concentration of 0.01 M. The plate-like composite reverted back to granular at 0.05 M Fe-doped HAp. An increase in Fe within the lattice resulted in an enhancement in surface area and microporous volume resulting in a spike in gas uptake capacity towards CO and CO_2 gas. Co-Doped HAp thick film composites were explored as a viable sensor by M. P. Mahabole *et al.* towards detection of CO and CO_2. The percentage of variation in the Co dopant ranged between 0.008 M and 0.05 M. This variation in the ion-exchanged composite altered the crystal size and porosity. The maximum response to CO_2 was exhibited by the 0.01 M Co-doped HAp composite at 75% at an operating temperature of 135 °C. This is attributed to the reduction in (201) oriented crystal planes as the concentration of Co within the lattice increases.[216]

An extended study on these doped composites was carried out by modifying the surface of the sensor material through the process of swift heavy ion irradiation (SWI). Here, both the Fe-doped and Co-doped HAp screen printed sensor substrates were subjected to Ag^{7+} ion irradiation with an ion fluence ranging between 3×10^{11} ions cm^{-2} and 3×10^{13} ions cm^{-2}, respectively. This process modified the surface by enhancing the pore size and the density of active adsorption sites.[217,218] The response of the ceramic was tested with CO and CO_2 gas at an optimum operating temperature of 140 °C and 155 °C respectively. The response–recovery time significantly improved with CO and CO_2 gas response witnessing a ~2.5 times increase in comparison to pristine HAp crystals. The orientation of HAp crystals in ref. 217–219 was along a predominantly exposed *c*-plane. The variation in % sensitivity between pristine HAp, Fe-doped HAp, Co-doped HAp, SWI-Fe-doped HAp and SWI-Co-doped HAp towards detection of CO gas can be seen in Table 6. With each modification, the response–recovery time of the composite sensor witnesses an improvement. The sensitivity for pure HAp is 45% while Fe-doped HAp and Co-doped HAp are enhanced by a factor of 2 and 3 respectively. On the other hand, SWI-HAp indicated a sensitivity of 210% (4.6 times increase from pure HAp). SWI improved the efficacy of Fe- and Co-doped HAp towards detection of CO gas. Similar trends were observed in the sensing of CO_2 gas.

A carbon-based sensor material was reportedly synthesized by R. S. Khairnar *et al.* by mechanically grinding 0.1 wt% CNTs with 99.9 wt% HAp prepared *via* chemical precipitation.[220,221] The addition of CNTs as a dopant over spherical HAp nanoparticles witnessed an improvement in the gas uptake capacity. Furthermore, the inherent electrical conductivity of CNTs facilitated the detection of 20 ppm of CO and CO_2 gas at a reduced operating temperature of 105 °C and 70 °C respectively. However, the operating temperature for maximum % sensitivity for pure HAp was 175 °C. While the % sensitivity of pure HAp towards CO and CO_2 was 100%, the detection level for CNT doped HAp towards CO and CO_2 was 130% and 200% respectively. Although the spherical CNT doped HAp had a crystal preferentially along the (300) plane rather than (002), the sensitivity was higher due to the increased surface area for adsorption of the analyte gas.

The mechanism of adsorption and quantification of CO and CO_2 gas can be related either through their interaction with the surface OH^- group along the *c*-plane or through their reaction with O^{2-} species.[215] CO, a reducing gas, gets oxidized to CO_2 and subsequently into the CO_3^{2-} anion.[222]

$$2OH^- + CO \rightarrow CO_2 + H_2O \quad (31)$$

$$O^{2-} + CO \rightarrow CO_2 + 2e^- \quad (32)$$

$$O^{2-} + CO_2 \rightarrow CO_3^{2-} \quad (33)$$

The formation of CO_3^{2-} results in its incorporation within the HAp crystal lattice inducing variations in conductivity. Additionally, an alternate mechanism has been reported wherein the O^{2-} ion formed during the proton shift (eqn (17)) may react with CO and CO_2 gas molecules resulting in the formation of CO_2 and CO_3^{2-} respectively. The formation of electrons (eqn (32)) and the migration of protons (eqn (17)) serve as key factors responsible for the variation in resistance, as a consequence resulting in the detection of CO and CO_2 gas analytes.

6.2. HAp nanocomposites towards detection of electrolytic analytes (biosensors)

Most electrolytic biosensors aid in the determination of dissolved analytes *via* employing enzymatic and non-enzymatic substrates. The ease of loading and binding of enzymes to HAp biomaterials makes it feasible towards electrochemical sensing of target molecules. The response characteristics of select HAp biosensors are tabulated in Table 7.

6.2.1. Detection of glucose. Electrolytic detection of glucose extends prominently to the field of biosensing as well as to the catalytic oxidation of glucose in biofuel cells.[223] The assessment of glucose levels in blood *via* electrolytic sensing serves in real-time monitoring of diabetes. The catalytic oxidation of glucose in biosensors is achieved through enzymatic biosensors comprised of the GOx enzyme. In comparison with non-enzymatic biosensors, enzymatic sensors have a drawback with respect to shelf-life due to denaturation of the protein. R. Ma *et al.* reported the fabrication of an electrochemical sensor with immobilized GOx on the HAp/Nafion composite.[224] Studies relating the affinity between the surface Ca^{2+} and PO_4^{3-} moieties and the protein have reported the role of HAp–protein electrostatic interactions. The GOx/HAp/Nafion nanocomposite displayed excellent biosensing capabilities of the quasi-reversible

Table 7 Key response characteristics of HAp-based electrodes towards electrolytic biosensing

S. No.	HAp modified composite	Substrate electrode	Analyte species	Linear range (μM)	Limit of detection (μM)	Sensitivity (μA mM^{-1} cm^{-2})	Ref.
1	HAp/GOx/Nafion	GCE	Glucose	120–2160	20	6.75 mA M^{-1}	224
2	GOx/HAp/TiO_2/MWCNT	GCE	Glucose	10–15 200	2.0	57.0	225
3	PoPD/GA-GOx/HAp/Au	Au foil	Glucose	3–1700	0.34	32.2	226
4	RGO/HAp/GOx	GCE	Glucose	100–11 500	30	16.9	227
5	PANI/HAp	Ni foam	Glucose	1–30 000	0.32	1704.53	228
6	Cyt *c*/FCNFs/HAp	Au	H_2O_2	2–8700	0.3	—	265
7	HAp/chitosan/tyrosinase	Au	Catechol	0.01–7	0.005	2110	230
			Phenol	0.07–5	0.01	1770	
			m-Cresol	0.01–5	0.005	2050	
8	Fe-HAp/tyrosinase	GCE	L-Tyrosine	0.1–11	0.245	—	231
9	Ce-HAp	GCE	NE	0.1–200	0.058	—	232
			UA	0.5–200	0.39	—	
			Tyr	0.1–200	0.072	—	
10	HAp	m-CPE	UA	0.068–50	0.05	—	233

process towards detection of glucose. The oxidative pathway of GOx involved a two electron and two proton pathway:

$$\mathrm{GOx\ (FAD)} + 2e^- + 2H^+ \rightarrow \mathrm{GOx\ (FADH_2)\ (in\ N_2\ saturated\ PBS)} \quad (34)$$

$$\mathrm{GOx\ (FADH_2)} + \mathrm{glucose} + \mathrm{O_2} \rightarrow \mathrm{GOx\ (FAD)} + \mathrm{gluconolactone} + \mathrm{H_2O_2\ (in\ O_2\ saturated\ PBS)} \quad (35)$$

The amperometric electrosensing of glucose is carried out under an O_2 saturated environment wherein the oxidation of glucose over the GOx takes place with the consumption of dissolved O_2. The drop in O_2 levels reflects the reduction in peak current, thus facilitating the quantification of glucose levels towards biosensing. A response time of 6 s was achieved within the concentration range of 0.12–2.16 mM with an estimated detection limit of 0.02 mM. The biosensor was also tested for its anti-interference ability in an environment of co-existing species such as ascorbic acid, uric acid and L-cysteine. L-Cysteine and uric acid had no effect on the amperometric response while ascorbic acid had a very negligible effect as an interfering species, ascribed to its interaction with O_2. The HAp modified GOx/Nafion amperometric sensor displayed stability, exhibiting a current response of up to 94% of its original value even after storing in 0.1 M PBS at 4 °C for 2 weeks with a relative standard deviation of ~6%. Other reported HAp-based enzymatic biosensors include HAp/GOx/TiO_2/MWCNTs with increased storage stability and enzyme durability in the sensor matrix,[225] the PoPD/GA-GOx/HAp/Au electrode with GA crosslinker and PoPD (added to prevent interference from ascorbic acid and uric acid species)[226] and the GOx immobilized RGO/HAp modified GCE.[227]

A non-enzymatic glucose biosensor was fabricated, reported in ref. 228, wherein the sensor composite comprised of HAp/PANI deposited onto a Ni foam substrate. The choice of Ni foam over Ni plate lies in its increased specific surface area. The nucleation and crystal orientation of the HAp crystals were along the *c*-axis resulting in needle-like crystals. The incorporation of PANI facilitated improvement in the conductivity of the biosensor while enhancing the current density required for electrocatalytic oxidation of glucose. The oxidation of glucose over a non-enzymatic HAp-Ni sensor is as follows:

$$\mathrm{NiOOH} + \mathrm{glucose} \rightarrow \mathrm{Ni(OH)_2} + \mathrm{gluconolactone} \quad (36)$$

NiOOH and $Ni(OH)_2$ are redox pairs formed by the exchange of OH^- species in alkaline media.[228] NiOOH extracts a proton from the hydroxyl group of glucose resulting in the formation of oxidized gluconolactone resulting in glucose sensing.

6.2.2. Detection of cyanide. Cyanide (CN^-) in excess can result in hypoxia as a result of its ability and affinity to bind to iron in cytochrome *c* oxidase thus interfering with electron transport. Considering its toxic nature and potential contamination of food and the environment, a reliable and accurate biosensor can be effective towards the detection of CN^- ions. S. Wang *et al.* reported the fabrication of a facile CN^- biosensor by employing HRP/chitosan/HAp as a sensor material.[229] The HAp nanowire array was synthesized *via* the template-assisted electrodeposition technique directly onto the GCE (Fig. 20d) with the aid of a pre-textured polycarbonate template. HRP and chitosan were loaded onto the HAp/GCE for aqueous CN^- sensing. The detection of CN^- species is based on the catalytic interaction between HRP and H_2O_2. A variation in the reduction current is witnessed depending on the concentration of H_2O_2 undergoing catalytic interaction with the HRP enzyme. When CN^- species is introduced into the electrolyte, it binds with the heme iron in HRP resulting in enzyme deactivation, thus resulting in decreased catalytic response of HRP towards H_2O_2. Employment of an aligned HAp nanowire-nanoarray facilitated spatial orientation for effective enzyme loading.

6.2.3. Detection of organics. Electrochemical biosensing of solvated organic compounds is considered to be highly effective *via* amperometric detection by virtue of its high sensitivity and rapid response. HAp derived enzymatic and non-enzymatic biosensors for the monitoring of phenolic compounds, uric acid, and tyrosine have been reported. Immobilized tyrosinase substrates are preferably employed for the detection of phenolics. The study reported in ref. 230 presents the fabrication of the tyrosinase enzyme immobilized onto the HAp/chitosan composite wherein HAp was assimilated as nanorods. The composite

displayed excellent stability of up to 85% after a month at a working pH of 7. The phenol derivatives detected in this study included catechol, phenol and *m*-cresol. The catalytic oxidation of the phenol derivative, in this case, catechol, over the enzyme substrate results in the formation of *o*-quinone given as

$$\text{Catechol} + \text{tyrosinase}\ (O_2) \rightarrow o\text{-quinone} + H_2O \quad (37)$$

The detection and quantification are achieved by monitoring the reduction potential peak of the formed *o*-quinone. P. Kanchana *et al.* developed an Fe-doped HAp/tyrosinase enzymatic biosensor loaded over GCE for the detection of L-tyrosine.[231] The microstructure of HAp was plate-like with increased crystal growth along the *a*,*b*-plane. The optimum working pH was determined to be 7.0 with a detection limit of 245 nM. A Ce-doped HAp non-enzymatic biosensor was constructed on GCE for the simultaneous detection of norepinephrine (NE), UA and tyrosine (Tyr)[232] with HAp assuming a spherical morphology. An uric acid biosensor was reported, detailed in ref. 233, discussing the role of mesoporous volume and density of surface acidic sites of the HAp crystal at a working pH of 7.

7. Discussion

Some of the general advantages in the modification of growth alignment in crystal orientation of hexagonal HAp lie in the fact that (a) the density of acidic and basic sites can be modulated thereby enhancing its applicatory nature, (b) an improvement in proton conductivity with respect to the predominantly exposed crystal facet can be achieved and (c) the physicochemical variables such as adhesion, corrosion resistance and adsorption dynamics can be significantly enhanced with manipulation of HAp crystal growth. In general, the rate of nucleation, growth rate, crystal alignment and Ca/P ratio can be related to parametric modifications encompassing the electrochemical deposition technique. The parameters discussed in the review are categorized as driving parameters that initiate and control the deposition rate of HAp and assisting parameters that work synergistically with the driving parameters so as to enhance the nucleation rate, refinement in crystal orientation and improved coating characteristics. Furthermore, the preference of either two- or three-electrode electrochemical setup has been highlighted. The advantage of the three-electrode setup over the two-electrode counterpart can be attributed to circumventing the IR drop and maintaining a stable potential throughout electrodeposition despite variations in cathode charge density with progressive HAp growth.

The role of applied potential and applied current density, under either static or dynamic conditions, in the microstructural outcome of HAp coating has been elaborated.[80,234] The pulsing of potential or current has a significant effect in ensuring control over dissociation of H_2O and the liberation of H_2 gas at the cathode *via* employing a duty cycle with a shorter ON pulse duration.[235,236] Additionally, the presence of pulses ensures a minimum shift in cathodic pH.[237] The diffusion of phosphate species into a porous TiO_2 surface can be controlled by tuning the pulse duration thereby resulting in variation in the Ca/P ratio[238] and control over HAp crystal orientation.[239] Modifications of the Ca/P ratio, crystal size and coating stability were controlled through electrodeposition parameters such as loading time, electrolyte temperature and pH.

In addition to these driving parameters, variations in assisting parameters reported under electrodeposition of HAp were elaborated in this review. The implementation of ultrasonics during electrodeposition witnesses a reduction in coating roughness and pore size, enhancement in dispersion of ionic species, rapid removal of H_2 bubbles and removal of weakly adhered coatings. Furthermore, the crystal orientation of ultrasonically grown HAp may result in the formation of either plate- or needle-like microstructures depending on the applied current density.[240] The effects of electrolytic additives like KOH and NaOH augment the formation of HAp while addition of $NaNO_3$ witnesses an enhancement in the ionic conductivity of the electrolyte.[241] The presence of chelating agents such as EDTA results in crystal orientation along the *a*,*b*-axes *via* the control of supersaturation of the Ca-EDTA chelate complex. The addition of H_2O_2 to the electrolytic system witnesses an increase in cathodic pH resulting in increased PO_4^{3-} formation. The added advantage of H_2O_2 significantly improves the coating properties as evidenced by the decreased formation of H_2 bubbles. As an alternative to solvated ionic Ca^{2+} and PO_4^{3-} precursors, the possibility of employing dispersed HAp nanoparticles was explored under the simultaneous anodization–electrodeposition technique resulting in nanospherical deposits.[242,243] Furthermore, the deposition of HAp nanoslabs/nanoplates onto a Ti plate is reported wherein HAp nanoslabs were synthesized prior to dispersal in a deposition electrolyte.[244] The technique of simultaneous precipitation–electrodeposition proved fruitful in the preferential *c*-axis growth of acicular HAp with improved crystallinity and uniformity.[120,245] An external applied magnetic field facilitates the growth of hexagonal rods or flakes depending on the orientation of the magnetic flux (B) with respect to electrical flux (j), either in a parallel or in a perpendicular fashion. The morphology, crystal size and orientation witnessed a variation, either as needles or as flakes, under a N_2 or CO_2 cell atmosphere.[152] Employing high pressure during electrodeposition increased the size of deposited crystals. A reduced pressure facilitated removal of H_2 bubbles from the cathode thus circumventing the formation of weak coatings.[246] Substrate modification and pretreatment improved the overall coating characteristics.[247] The rate of growth and adhesion to the substrate increased when TiO_2 NTs were employed.[248] The ease of electrochemically coating HAp over complex substrates such as TiO_2 nanofibers,[249] carbon fiber cloth,[240] transparent MEA chip,[250] foam,[162] mesh[241,251] and Nafion substrates[163] is highlighted. Employing the cation exchange membrane-assisted electrodeposition technique significantly alters HAp formation as hollow tubular microstructures[163,164,196] and the phase evolution of the coating.[252] The technique of cyclic electrodeposition involving the alternative immersion of the substrate in Ca and P precursors under galvanostatic conditions resulted in the formation of HAp crystals with a predominantly exposed *a*,*b*-facet.[166,167]

These driving and assisting parameters, either acting alone or in synergy within a multitude of combinations, are shown to contribute to the morphological outcome of electrodeposited HAp in terms of preferential crystal orientation. The importance of oriented HAp crystals, facilitating the optimized sensing of gaseous and electrolytic analytes, has been indicated through the adsorptive interaction of the analyte species with HAp crystal facets.

8. Correlation in electrodeposited HAp architecture with respect to current density and pH

Among the discussed driving parametric determinants, the influence of both current density and pH on HAp microstructure formation is significant under the galvanostatic electrodeposition method. Relatively, other driving parameters such as loading time and electrolytic temperature serve in enhancing the crystal size and growth of HAp. Additionally, the applied potential plays a role in topography within the limits of under −1.4 V and −1.8 V for the two- and three-electrode system respectively. Beyond this range in applied potential, the coating characteristics and microstructure deteriorate due to electrolytic dissociation of H_2O and the evolution of H_2 gas bubbles on the cathode surface. Additionally, the electrolytic pH is an important parameter in crystal growth due to the consequential solubility of HAp deposits in a highly acidic environment and its formation beyond a particular pH range. It was understood that at acidic pH (<4), DCDP and OCP phases predominate over HAp formation. However, a conversion to the HAp phase is witnessed beyond pH 4 or when the deposits are immersed in an alkaline bath. This preliminary inference reveals that pH plays a role in phase change while applied current density initiates and influences HAp growth and morphology under the galvanostatic mode.

Based on this hypothesis, an analysis has been made in this section, correlating the premise of control in both electrolytic pH and current density and its effects over the microstructural outcome and preferential crystal orientation of the HAp deposits. For our analysis, we collected data on pH and current density from reported literature while maintaining constancy of other experimental parameters. It was ensured that the substrate was Ti-based (like metallic Ti, TiO_2 NTs and Ti_6Al_4V alloys) whereas the electrolyte comprised of $Ca(NO_3)_2$ and $NH_4H_2PO_4$ as precursors. By maintaining this parametric constancy, the collected data were plotted (shown in Fig. 22) while maintaining the pH range between 4.0 and 7.5 and the galvanostatic current density between 0 and 20 mA cm^{-2}. From the figure, it is inferred that within this pH range, the formation of needle-like or flake-like HAp can be controlled with modulation of applied current density. As discussed in this section, pH was selected from above 4.0 due to the formation of HAp *via* phase conversion from DCDP and OCP phases. The formation of needles at pH ∼ 4.5 up to 10 mA cm^{-2} indicates the control of these parameters resulting in preferential *c*-axis growth. However, for an increase above 10 mA cm^{-2} (at pH ∼ 4.5), the microstructure is witnessed to convert to a flake-like *a*,*b*-plane orientation. At pH ≥ 7, the probability of formation of a mixture of rod-like and flake-like HAp is higher. Furthermore, this analysis reveals the correlation of applied current density with pH and the subsequent selective morphological variation resulting in the controlled alignment of the electrochemically deposited HAp crystal facet, *i.e.*, preferential growth either along the *a*,*b*-plane or along the *c*-plane. Current densities higher than the plate-like region (indicated in stripped red in Fig. 22) are speculated to result in the formation of spherical HAp nanoparticles, although data regarding higher current densities are limited for the prerequisites put forth in this correlation.

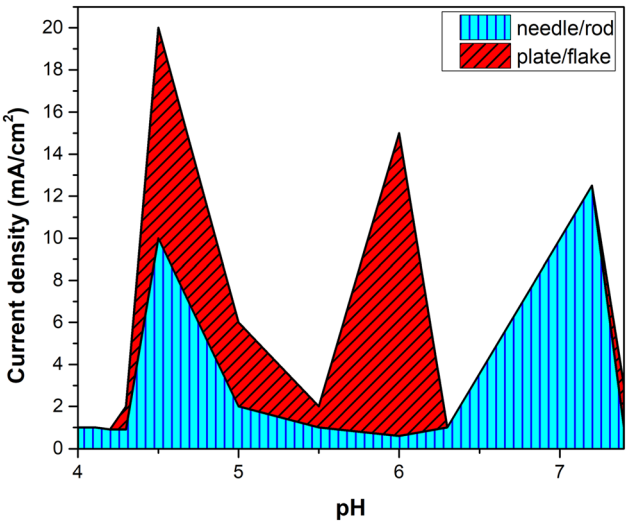

Fig. 22 Correlation of applied current density and pH and the probability range of their influence on the microstructural outcome of needle/flake type HAp crystals.

9. Summary and future perspective

This review encompasses a discussion on the crystal structure of hexagonal HAp, focusing on the two important crystal facets of HAp, namely, the *a*,*b*-facet and the basal *c*-facet. The technique of electrodeposition of HAp and nucleation and crystal growth of HAp are presented. Notably, we highlighted the possibility of controlling the HAp crystal orientation through the variations in each parametric determinant involved under the technique of electrodeposition. Furthermore, by categorization of reported electrochemical parameters under driving and assisting parameters, their influence on the morphology was reviewed. The parameters of applied potential and current density, time, temperature, and pH, the influence of ultrasound assistance and additives, the effect of an external magnetic field and microgravity, electrolytic pressure and controlled atmosphere, and substrate-based electrodeposition of HAp were briefly discussed. Furthermore, this review presents a brief purview on the efficacy of phase pure HAp and its composites as sensor materials towards electrochemical detection of gaseous molecules and electrolytic analytes. The mechanistic interactions of HAp with gases such as NH_3, NO_x, H_2S, CO, CO_2 and VOCs and with

the electrolytic sensing of glucose, CN^- and solvated organics have been discussed. This review highlighted the importance of crystal facet exposure by correlating the predominant crystal orientation to sensitivity. The presence of hexagonal rods or flakes determines the efficacy of the HAp nanocomposite. The correlation of current density and pH indicates the possibility to tune the morphology thereby controlling the density of active sites. The conceptual elucidation discussed in this manuscript can be extrapolated to various substituted HAp composites for furthering the possibility of effective sensors. Additionally, the concept of exposing the favourable crystal facet will prove advantageous while employing HAp in the field of catalysis, ion exchange, and adsorption phenomena. Therefore, extending subsequent research along these lines will encourage future development of environmentally friendly and improved HAp biomaterials.

Author contributions

Priya Ranjan Dev – conceptualization, supervision, formal analysis, writing – original draft, writing – review & editing; Chekkottu Parambil Anand – data curation, writing – editing & proofreading; David Samuvel Michael – data curation, writing – editing & proofreading; and P. Wilson – guidance and supervision.

List of abbreviations

Abbreviations

AFM	Atomic force microscopy
β-TCP	Beta-tricalcium phosphate
CNTs	Carbon nanotubes
Cyt *c*	Cytochrome *c*
DCDP	Dicalciumdiphosphate
j	Electrical flux
EDS	Energy dispersive spectroscopy
FESEM	Field emission scanning electron microscopy
FCNFs	Functionalized carbon nanofibers
GCE	Glassy carbon electrode
F_G	Gravitational force
HELCDEB	High energy low current electron beam
HRP	Horseradish peroxidase
LPG	Liquified petroleum gas
LEL	Lower explosive limit
B	Magnetic flux
F_m	Magnetization force
F_B	Magnetohydrodynamic force
MHD	Magnetohydrodynamics
MEA	Microelectrode array
m-CPE	Modified carbon paste electrode
MCPM	Monocalcium phosphate monohydrate
MWCNT	Multi-walled carbon nanotubes
NTs	Nanotubes
OSHA	Occupational Safety and Health Administration
OCP	Octacalcium phosphate
PBS	Phosphate buffer solution
RT	Room temperature
SCE	Saturated calomel electrode
SBF	Simulated body fluid
SS	Stainless steel
SWI	Swift heavy ion irradiation
UV	Ultraviolet
VOCs	Volatile organic compounds
XRD	X-ray diffraction
XPS	X-ray photoelectron spectroscopy

Chemical name

NH_3	Ammonia
Ar^+	Argon cation
Ca^{2+}	Calcium cation
CO_2	Carbon dioxide
CO	Carbon monoxide
Cl^-	Chloride anion
Co^{2+}	Cobalt cation
CN^-	Cyanide anion
$H_2PO_4^-$	Dihydrogen phosphate anion
EtOH	Ethanol
EDTA	Ethylenediaminetetraacetic acid
FAD	Flavin adenine dinucleotide
F^-	Fluoride anion
GOx	Glucose oxidase
GA	Glutaraldehyde
Au	Gold
GO	Graphene oxide
H_2S	Hydrogen sulfide
H_2	Hydrogen gas
H_2O_2	Hydrogen peroxide
H_3O^+	Hydronium ion
OH^-	Hydroxide ion
Fe^{2+}	Iron cation
Pb^{2+}	Lead cation
LiCl	Lithium chloride
Mg	Magnesium
Mn^{2+}	Manganese cation
HPO_4^{2-}	Monohydrogen phosphate anion
Ni	Nickel
NiOOH	Nickel oxide hydroxide
NO_3^-	Nitrate anion
NO	Nitric oxide
NO_2^-	Nitrite anion
NE	Norepinephrine
PO_4^{3-}	Phosphate anion
Pt	Platinum
PoPD	Poly(*o*-phenylenediamine)
PANI	Polyaniline
PPy	Polypyrrolidine
H^+	Proton
RGO	Reduced graphene oxide
Na^+	Sodium cation
SO_2	Sulfur dioxide
THF	Tetrahydrofuran
TiO_2	Titania
Ti	Titanium

Tyr	Tyrosine
UA	Uric acid

Units and symbols

V	Applied potential
°C	Degree Celsius
cc g^{-1}	Cubic centimeter per gram
e^{-}	Electron
h	Hour
K	Kelvin
L min^{-1}	Liter per minute
MPa	Megapascal
m^2 g^{-1}	Square meter per gram
μA mM^{-1} cm^{-2}	Microampere per millimolar per square centimeter
μm	Micrometer
μm $year^{-1}$	Micrometer per year
μM	Micromolar
μmol dm^{-3}	Micromolar per cubic decimeter
mA cm^{-2}	Milliampere per square centimeter
mg L^{-1}	Milligram per liter
mm	Millimeter
mM	Millimolar
mT	Millitesla
mV s^{-1}	Millivolt per second
min	Minute
mol	Mole
mol L^{-1}	Mole per liter
nm	Nanometer
nM	Nanomolar
ppm	Parts per million
s	Second
T	Tesla
Torr	Torricelli
vol%	Volume percentage
W	Watt
wt%	Weight percentage

Conflicts of interest

There are no conflicts of interest to declare.

Acknowledgements

The authors would like to acknowledge the Science and Engineering Research Board (SERB), India, under the Department of Science and Technology (DST) (Grant No.: EMR/2015/001406). Priya Ranjan Dev would like to thank Pavithra Dev and M. Lilly Mary for their support and motivation while consolidating the present review.

References

1 L. Yan, Y. Xiang, J. Yu, Y. Wang and W. Cui, *ACS Appl. Mater. Interfaces*, 2017, **9**, 5023–5030.
2 H. R. Bakhsheshi-Rad, E. Hamzah, A. F. Ismail, M. Aziz, E. Karamian and N. Iqbal, *Trans. Nonferrous Met. Soc. China*, 2018, **28**, 1553–1562.
3 E. Vidal, J. Buxadera-Palomero, C. Pierre, J. M. Manero, M.-P. Ginebra, S. Cazalbou, C. Combes, E. Rupérez and D. Rodríguez, *Surf. Coat. Technol.*, 2019, **358**, 266–275.
4 J. Kolmas, S. Krukowski, A. Laskus and M. Jurkitewicz, *Ceram. Int.*, 2016, **42**, 2472–2487.
5 H. Wang, C. Wang, B. Xiao, L. Zhao, J. Zhang, Y. Zhu and X. Guo, *Catal. Today*, 2016, **259**, 340–346.
6 A. A. Gandhi, M. Wojtas, B. L. Sidney, A. L. Kholkin and S. A. M. Tofail, *J. Am. Ceram. Soc.*, 2014, **97**, 2867–2872.
7 R. Rodriguez, D. Rangel, G. Fonseca, M. Gonzalez and S. Vargas, *Results Phys.*, 2016, **6**, 925–932.
8 Y. Ding, J. Liu, H. Wang, G. Shen and R. Yu, *Biomaterials*, 2007, **28**, 2147–2154.
9 A. Dehghanghadikolaei and B. Fotovvati, *Materials*, 2019, **12**, 1795.
10 P. Xie, Z. Shi, M. Feng, K. Sun, Y. Liu, K. Yan, C. Liu, T. A. A. Moussa, M. Huang, S. Meng, G. Liang, H. Hou, R. Fan and Z. Guo, *Adv. Compos. Hybrid Mater.*, 2022, **5**, 679–695.
11 P. E. Lokh, e e, V. Kadam, C. Jagatap, U. S. Chavan, R. Udayabhaskar and H. M. Pathan, *ES Mater. Manuf.*, 2022, **17**, 53–56.
12 M. Lian, Y. Huang, Y. Liu, D. Jiang, Z. Wu, B. Li, Q. Xu, V. Murugadoss, Q. Jiang, M. Huang and Z. Guo, *Adv. Compos. Hybrid Mater.*, 2022, DOI: **10.1007/s42114-022-00475-6**.
13 D. K. Shah, D. KC, T.-G. Kim, M. S. Akhtar, C. Y. Kim and O.-B. Yang, *Eng. Sci.*, 2022, **18**, 243–252.
14 Y. Cheng and G. Zhang, *ES Energy Environ.*, 2022, **17**, 1–10.
15 J. Cai, V. Murugadoss, J. Jiang, X. Gao, Z. Lin, M. Huang, J. Guo, S. A. Alsareii, H. Algadi and M. Kathiresan, *Adv. Compos. Hybrid Mater.*, 2022, **5**, 641–650.
16 J. Guo, Z. Chen, Z. M. El-Bahy, H. Liu, H. M. Abo-Dief, W. Abdul, K. M. Abualnaja, A. K. Alanazi, P. Zhang, M. Huang, G. Hu and J. Zhu, *Adv. Compos. Hybrid Mater.*, 2022, **5**, 899–906.
17 J. Chen, Y. Zhu, Z. Guo and A. G. Nasibulin, *Eng. Sci.*, 2020, **12**, 13–22.
18 B. Dai, Y. Ma, F. Dong, J. Yu, M. Ma, H. K. Thabet, S. M. El-Bahy, M. M. Ibrahim, M. Huang, I. Seok, G. Roymahapatra, N. Naik, B. B. Xu, J. Ding and T. Li, *Adv. Compos. Hybrid Mater.*, 2022, **5**, 704–754.
19 X. Sun, D. Zhu, M. Liu, Y. Song and J. Wang, *Eng. Sci.*, 2022, **20**, DOI: **10.30919/es8d715**.
20 S. E. Chavez, H. Ding, B. L. Williams, S. Nam, Z. Hou, D. Zhang and L. Sun, *ES Mater. Manuf.*, 2022, **15**, 72–77.
21 D. Pan, G. Yang, H. M. Abo-Dief, J. Dong, F. Su, C. Liu, Y. Li, B. Bin Xu, V. Murugadoss, N. Naik, S. M. El-Bahy, Z. M. El-Bahy, M. Huang and Z. Guo, *Nano-Micro Lett.*, 2022, **14**, 118.
22 Y. Ma, X. Xie, W. Yang, Z. Yu, X. Sun, Y. Zhang, X. Yang, H. Kimura, C. Hou, Z. Guo and W. Du, *Adv. Compos. Hybrid Mater.*, 2021, **4**, 906–924.

23 C. Dang, Q. Mu, X. Xie, X. Sun, X. Yang, Y. Zhang, S. Maganti, M. Huang, Q. Jiang, I. Seok, W. Du and C. Hou, *Adv. Compos. Hybrid Mater.*, 2022, **5**, 606–626.
24 R. Ma, B. Cui, D. Hu, S. M. El-Bahy, Y. Wang, I. H. E. Azab, A. Y. Elnaggar, H. Gu, G. A. M. Mersal, M. Huang and V. Murugadoss, *Adv. Compos. Hybrid Mater.*, 2022, **5**, 1477–1489.
25 Z. Wang, X. Li, L. Wang, Y. Li, J. Qin, P. Xie, Y. Qu, K. Sun and R. Fan, *Adv. Compos. Hybrid Mater.*, 2020, **3**, 1–7.
26 C. Stephen, B. Shivamurthy, M. Mohan, A.-H. I. Mourad, R. Selvam and B. H. S. Thimmappa, *Eng. Sci.*, 2022, **18**, 75–97.
27 S. M. Shahabaz, S. Sharma, N. Shetty, S. D. Shetty and G. M. C., *Eng. Sci.*, 2021, **16**, 26–46.
28 B. Vinod, S. Suresh and D. Sudhakara, *Adv. Compos. Hybrid Mater.*, 2020, **3**, 194–204.
29 J. C. D. M. Neto, N. R. do Nascimento, R. H. Bello, L. A. de, V. Verçosa, J. E. Neto, J. C. M. da Costa, F. Rol and O. V. Diaz, *Eng. Sci.*, 2022, **17**, 28–44.
30 N. Naik, B. Shivamurthy, B. H. S. Thimmappa, A. Gupta, J. Z. Guo and I. Seok, *Eng. Sci.*, 2022, **20**, DOI: **10.30919/es8d713**.
31 R. S. Pillai, M. Frasnelli and V. M. Sglavo, *Ceram. Int.*, 2018, **44**, 1328–1333.
32 X. Zhang, Y. Wu, Y. Lv, Y. Yu and Z. Dong, *Surf. Coat. Technol.*, 2020, **386**, 125483.
33 T. V. Khamova, O. V. Frank-Kamenetskaya, O. A. Shilova, V. P. Chelibanov, A. M. Marugin, E. A. Yasenko, M. A. Kuz'mina, A. E. Baranchikov and V. K. Ivanov, *Crystallogr. Rep.*, 2018, **63**, 254–260.
34 M. Catauro, F. Papale, L. Sapio and S. Naviglio, *Mater. Sci. Eng., C*, 2016, **65**, 188–193.
35 R. Chen and J. Shen, *Mater. Lett.*, 2020, **259**, 126881.
36 O. Yigit, B. Dikici, T. C. Senocak and N. Ozdemir, *Surf. Coat. Technol.*, 2020, **394**, 125858.
37 X. Sun, H. Lin, C. Zhang, J. Jin and S. Di, *Coatings*, 2019, **9**, 667.
38 R. I. M. Asri, W. S. W. Harun, M. A. Hassan, S. A. C. Ghani and Z. Buyong, *J. Mech. Behav. Biomed. Mater.*, 2016, **57**, 95–108.
39 M. Sadat-Shojai, M.-T. Khorasani, E. Dinpanah-Khoshdargi and A. Jamshidi, *Acta Biomater.*, 2013, **9**, 7591–7621.
40 Y. Lu, W. Dong, J. Ding, W. Wang and A. Wang, *Nanomaterials from Clay Minerals*, Elsevier, 2019, pp. 485–536.
41 Y.-J. Zhu and B.-Q. Lu, *ACS Biomater. Sci. Eng.*, 2019, **5**, 4951–4961.
42 S. Awasthi, S. K. Pandey, E. Arunan and C. Srivastava, *J. Mater. Chem. B*, 2021, **9**, 228–249.
43 M. Prakasam, J. Locs, K. Salma-Ancane, D. Loca, A. Largeteau and L. Berzina-Cimdina, *JFB*, 2015, **6**, 1099–1140.
44 F. Anene, J. Aiza, I. Zainol, A. Hanim and M. T. Suraya, *Proc. Inst. Mech. Eng., Part L*, 2020, **234**, 1450–1460.
45 S. Omar, M. S. Muhamad, L. Te Chuan, T. Hadibarata and Z. C. Teh, *Water, Air, Soil Pollut.*, 2019, **230**, 275.
46 S. Pai, M. S. Kini and R. Selvaraj, *Environ. Sci. Pollut. Res.*, 2021, **28**, 11835–11849.
47 W. S. W. Harun, R. I. M. Asri, J. Alias, F. H. Zulkifli, K. Kadirgama, S. A. C. Ghani and J. H. M. Shariffuddin, *Ceram. Int.*, 2018, **44**, 1250–1268.
48 A. Saxena, M. Pandey and A. K. Dubey, *J. Indian Inst. Sci.*, 2019, **99**, 339–359.
49 A. Das and D. Pamu, *Mater. Sci. Eng., C*, 2019, **101**, 539–563.
50 F. R. Baxter, C. R. Bowen, I. G. Turner and A. C. E. Dent, *Ann. Biomed. Eng.*, 2010, **38**, 2079–2092.
51 A. Fihri, C. Len, R. S. Varma and A. Solhy, *Coord. Chem. Rev.*, 2017, **347**, 48–76.
52 M. Šupová, *Ceram. Int.*, 2015, **41**, 9203–9231.
53 A. Zielinski and M. Bartmanski, *Coatings*, 2020, **10**, 782.
54 T.-T. Li, L. Ling, M.-C. Lin, H.-K. Peng, H.-T. Ren, C.-W. Lou and J.-H. Lin, *J. Mater. Sci.*, 2020, **55**, 6352–6374.
55 G. Ma and X. Y. Liu, *Cryst. Growth Des.*, 2009, **9**, 2991–2994.
56 M. Okada and T. Matsumoto, *Jpn. Dent. Sci. Rev.*, 2015, **51**, 85–95.
57 Z. Zhuang, T. J. Fujimi, M. Nakamura, T. Konishi, H. Yoshimura and M. Aizawa, *Acta Biomater.*, 2013, **9**, 6732–6740.
58 M. Ibrahim, M. Labaki, J.-M. Giraudon and J.-F. Lamonier, *J. Hazard. Mater.*, 2020, **383**, 121139.
59 Z. S. Stojanović, N. Ignjatović, V. Wu, V. Žunič, L. Veselinović, S. Škapin, M. Miljković, V. Uskoković and D. Uskoković, *Mater. Sci. Eng., C*, 2016, **68**, 746–757.
60 N. Mohan, R. Palangadan and H. Varma, *Ceram. Int.*, 2016, **42**, 17259–17268.
61 S. Khanmohammadi, M. Ojaghi-Ilkhchi and M. Farrokhi-Rad, *Ceram. Int.*, 2021, **47**, 1333–1343.
62 A. Janković, S. Eraković, M. Vukašinović-Sekulić, V. Mišković-Stanković, S. J. Park and K. Y. Rhee, *Prog. Org. Coat.*, 2015, **83**, 1–10.
63 S. V. Dorozhkin, *JFB*, 2010, **1**, 22–107.
64 A. Janković, S. Eraković, M. Mitrić, I. Z. Matić, Z. D. Juranić, G. C. P. Tsui, C. Tang, V. Mišković-Stanković, K. Y. Rhee and S. J. Park, *J. Alloys Compd.*, 2015, **624**, 148–157.
65 M. Farrokhi-Rad, *J. Alloys Compd.*, 2018, **741**, 211–222.
66 D. Drdlik, M. Slama, H. Hadraba, K. Drdlikova and J. Cihlar, *Ceram. Int.*, 2016, **42**, 16529–16534.
67 A. Stoch, A. Brożek, G. Kmita, J. Stoch, W. Jastrzębski and A. Rakowska, *J. Mol. Struct.*, 2001, **596**, 191–200.
68 N. N. C. Isa, Y. Mohd and N. Yury, *APCBEE Proc.*, 2012, **3**, 46–52.
69 T. Mokabber, Q. Zhou, A. I. Vakis, P. van Rijn and Y. T. Pei, *Mater. Sci. Eng., C*, 2019, **100**, 475–484.
70 S. Cometa, M. A. Bonifacio, M. Mattioli-Belmonte, L. Sabbatini and E. De Giglio, *Coatings*, 2019, **9**, 268.
71 T. Mokabber, L. Q. Lu, P. van Rijn, A. I. Vakis and Y. T. Pei, *Surf. Coat. Technol.*, 2018, **334**, 526–535.
72 Y. Han, T. Fu, J. Lu and K. Xu, *J. Biomed. Mater. Res.*, 2001, **54**, 96–101.
73 D. J. Blackwood and K. H. W. Seah, *Mater. Sci. Eng., C*, 2010, **30**, 561–565.
74 R. Hu, C. Lin, H. Shi and H. Wang, *Mater. Chem. Phys.*, 2009, **115**, 718–723.
75 S. K. Yen and C. M. Lin, *Mater. Chem. Phys.*, 2003, **77**, 70–76.

76 A. Vladescu, D. M. Vranceanu, S. Kulesza, A. N. Ivanov, M. Bramowicz, A. S. Fedonnikov, M. Braic, I. A. Norkin, A. Koptyug, M. O. Kurtukova, M. Dinu, I. Pana, M. A. Surmeneva, R. A. Surmenev and C. M. Cotrut, *Sci Rep.*, 2017, **7**, 16819.
77 D.-Y. Lin and X.-X. Wang, *Surf. Coat. Technol.*, 2010, **204**, 3205–3213.
78 D.-Y. Lin and X.-X. Wang, *Ceram. Int.*, 2011, **37**, 403–406.
79 B.-O. Taranu, A. I. Bucur and I. Sebarchievici, *J. Coat. Technol. Res.*, 2020, **17**, 1075–1082.
80 E. A. dos Santos, M. S. Moldovan, L. Jacomine, M. Mateescu, J. Werckmann, K. Anselme, P. Mille and H. Pelletier, *Mater. Sci. Eng., B*, 2010, **169**, 138–144.
81 M. Heydari Gharahcheshmeh and M. Heydarzadeh Sohi, *Mater. Chem. Phys.*, 2012, **134**, 1146–1152.
82 P. R. Dev, T. M. David, S. J. Samuel Justin, P. Wilson and A. Palaniappan, *J. Nanopart. Res.*, 2020, **22**, 56.
83 P. Peng, S. Kumar, N. H. Voelcker, E. Szili, R. S. C. Smart and H. J. Griesser, *J. Biomed. Mater. Res.*, 2006, **76A**, 347–355.
84 E. Tóth-Kádár, I. Bakonyi, L. Pogány and Á. Cziráki, *Surf. Coat. Technol.*, 1997, **88**, 57–65.
85 D. Gopi, A. Karthika, S. Nithiya and L. Kavitha, *Mater. Chem. Phys.*, 2014, **144**, 75–85.
86 F. A. Azem, T. K. Delice, G. Ungan and A. Cakir, *Mater. Sci. Eng., C*, 2016, **68**, 681–686.
87 L. Fathyunes, J. Khalil-Allafi and M. Moosavifar, *J. Mech. Behav. Biomed. Mater.*, 2019, **90**, 575–586.
88 T. Zhou, L. Yan, C. Xie, P. Li, L. Jiang, J. Fang, C. Zhao, F. Ren, K. Wang, Y. Wang, H. Zhang, T. Guo and X. Lu, *Small*, 2019, **15**, 1805440.
89 R. Chakraborty and P. Saha, *Surf. Interfaces*, 2018, **12**, 160–167.
90 Z. Zhao, G. Zhang and H. Li, *J. Cent. South Univ. Technol.*, 2004, **11**, 147–151.
91 P. T. Nam, T. D. Lam, H. T. Huong, N. T. Phuong, N. T. Thu Trang, T. Hoang, N. T. Thanh Huong, L. B. Thang, C. Drouet, D. Grossin, E. Kergourlay, G. Bertrand, D. Devilliers and D. T. Mai Thanh, *J. Nanosci. Nanotechnol.*, 2015, **15**, 9991–10001.
92 N. Eliaz and T. M. Sridhar, *Cryst. Growth Des.*, 2008, **8**, 3965–3977.
93 J. Kunze, L. Müller, J. M. Macak, P. Greil, P. Schmuki and F. A. Müller, *Electrochim. Acta*, 2008, **53**, 6995–7003.
94 M. Horynová, M. Remešová, L. Klakurková, K. Dvořák, I. Ročňáková, S. Yan, L. Čelko and G.-L. Song, *J. Am. Ceram. Soc.*, 2019, **102**, 123–135.
95 H. R. Le, K. Y. Chen and C. A. Wang, *J. Sol–Gel Sci. Technol.*, 2012, **61**, 592–599.
96 M. C. Kuo and S. K. Yen, *Mater. Sci. Eng., C*, 2002, **20**, 153–160.
97 C. M. Cotrut, A. Vladescu, M. Dinu and D. M. Vranceanu, *Ceram. Int.*, 2018, **44**, 669–677.
98 L. Fathyunes and J. Khalil-Allafi, *Ultrason. Sonochem.*, 2018, **42**, 293–302.
99 N. Edwin and P. Wilson, *Ultrason. Sonochem.*, 2019, **50**, 188–199.
100 T.-T. Li, L. Ling, M.-C. Lin, Q. Jiang, Q. Lin, C.-W. Lou and J.-H. Lin, *Mater. Sci.*, 2019, **105**, 13.
101 L. Fathyunes, J. Khalil-Allafi, S. O. R. Sheykholeslami and M. Moosavifar, *Mater. Sci. Eng., C*, 2018, **87**, 10–21.
102 L. Fathyunes and J. Khalil-Allafi, *Ceram. Int.*, 2017, **43**, 13885–13894.
103 S. Oh, R. Finones, C. Daraio, L. Chen and S. Jin, *Biomaterials*, 2005, **26**, 4938–4943.
104 T. Kokubo, H.-M. Kim, M. Kawashita and T. Nakamura, *J. Mater. Sci.: Mater. Med.*, 2004, **15**, 99–107.
105 M. Nobial, O. Devos, O. R. Mattos and B. Tribollet, *J. Electroanal. Chem.*, 2007, **600**, 87–94.
106 Y. Yajing, D. Qiongqiong, H. Yong, S. Han and X. Pang, *Appl. Surf. Sci.*, 2014, **305**, 77–85.
107 D. Gopi, E. Shinyjoy, M. Sekar, M. Surendiran, L. Kavitha and T. S. Sampath Kumar, *Corros. Sci.*, 2013, **73**, 321–330.
108 L. Ling, T.-T. Li, M.-C. Lin, Q. Jiang, H.-T. Ren, C.-W. Lou and J.-H. Lin, *Mater. Lett.*, 2020, **261**, 126989.
109 X. Chen, Z. Zhao, A. Chen and H. Li, *Trans. Nonferrous Met. Soc. China*, 2007, **17**, 617–621.
110 D. J. Blackwood and K. H. W. Seah, *Mater. Sci. Eng., C*, 2009, **29**, 1233–1238.
111 R. Drevet, H. Benhayoune, L. Wortham, S. Potiron, J. Douglade and D. Laurent-Maquin, *Mater. Charact.*, 2010, **61**, 786–795.
112 D. Gopi, J. Indira and L. Kavitha, *Surf. Coat. Technol.*, 2012, **206**, 2859–2869.
113 D. He, J. Du, P. Liu, X. Liu, X. Chen, W. Li, K. Zhang and F. Ma, *Surf. Coat. Technol.*, 2019, **365**, 242–247.
114 D. He, X. Zhang, P. Liu, X. Liu, X. Chen, F. Ma, W. Li, K. Zhang and H. Zhou, *Surf. Coat. Technol.*, 2021, **406**, 126656.
115 D.-Y. Lin, X.-X. Wang and Y. Jiang, *J. Biomed. Mater. Res.*, 2011, **96B**, 1–8.
116 N. Karimi, M. Kharaziha and K. Raeissi, *Mater. Sci. Eng., C*, 2019, **98**, 140–152.
117 J.-M. Jang, H.-C. Choe and W. A. Brantley, *Appl. Surf. Sci.*, 2019, **483**, 76–84.
118 S.-J. Park and J.-M. Jang, *J. Nanosci. Nanotechnol.*, 2011, **11**, 7167–7171.
119 J.-M. Jang, S.-W. Chung, H.-C. Choe and W. A. Brantley, *Surf. Coat. Technol.*, 2017, **320**, 383–390.
120 A. I. Bucur, E. Linul and B.-O. Taranu, *Appl. Surf. Sci.*, 2020, **527**, 146820.
121 M. E. Zilm, L. Chen, V. Sharma, A. McDannald, M. Jain, R. Ramprasad and M. Wei, *Phys. Chem. Chem. Phys.*, 2016, **18**, 16457–16465.
122 H. E. L. Madsen, *J. Cryst. Growth*, 1995, **152**, 94–100.
123 J. S. Sørensen and H. E. Lundager Madsen, *J. Cryst. Growth*, 2000, **216**, 399–406.
124 K. Inoue, K. Sassa, Y. Yokogawa, Y. Sakka, M. Okido and S. Asai, *Mater. Trans.*, 2003, **44**, 1133–1137.
125 S. Asai, *Modell. Simul. Mater. Sci. Eng*, 2004, **12**, R1–R12.
126 Y. Sakka, K. Takahashi, T. S. Suzuki, S. Ito and N. Matsuda, *Mater. Sci. Eng., A*, 2008, **475**, 27–33.
127 S. Asai, K. Sassa and M. Tahashi, *Sci. Technol. Adv. Mater.*, 2003, **4**(5), 455–460.

128 M. Okido, K. Kuroda, M. Ishikawa, R. Ichino and O. Takai, *Solid State Ionics*, 2002, **151**, 47–52.
129 T. Z. Fahidy, *J. Appl. Electrochem.*, 1983, **13**, 553–563.
130 T. Z. Fahidy, *Prog. Surf. Sci.*, 2001, **68**, 155–188.
131 L. M. A. Monzon and J. M. D. Coey, *Electrochem. Commun.*, 2014, **42**, 42–45.
132 P. Dunne and J. M. D. Coey, *J. Phys. Chem. C*, 2019, **123**, 24181–24192.
133 A. Bund, A. Ispas and G. Mutschke, *Sci. Technol. Adv. Mater.*, 2008, **9**, 024208.
134 A. Bund and H. H. Kuehnlein, *J. Phys. Chem. B*, 2005, **109**, 19845–19850.
135 A. Tian, X. Xue, C. Liu, J. He and Z. Yang, *Mater. Lett.*, 2010, **64**, 1197–1199.
136 C. Liu, A. Tian, H. Yang, Q. Xu and X. Xue, *Appl. Surf. Sci.*, 2013, **287**, 218–222.
137 R. Morimoto, M. Miura, A. Sugiyama, M. Miura, Y. Oshikiri, I. Mogi, S. Takagi, Y. Yamauchi and R. Aogaki, *J. Electroanal. Chem.*, 2019, **847**, 113255.
138 L. M. A. Monzon and J. M. D. Coey, *Electrochem. Commun.*, 2014, **42**, 38–41.
139 P. Mohammad Salahi Tohidi, M. S. Safavi, M. Etminanfar and J. Khalil-Allafi, *Mater. Chem. Phys.*, 2020, **254**, 123511.
140 Q. Xu, Y. Liu, C. Liu, A. Tian, X. Shi, C. Dong, Y. Zhou and H. Zhou, *RSC Adv.*, 2015, **5**, 14458–14464.
141 X. Y. Liu, *Appl. Phys. Lett.*, 2001, **79**, 3539–3541.
142 Y.-J. Ye, Y.-Y. Liu and D.-C. Yin, *Appl. Surf. Sci.*, 2015, **351**, 594–599.
143 Y. Ya-Jing, Y. Da-Chuan and S. Peng, *Appl. Surf. Sci.*, 2010, **256**, 7535–7539.
144 P. Ming, W. Lv, Y. Li, J. Shang and J. Wang, *Electrochim. Acta*, 2014, **120**, 6–15.
145 J. Du, X. Liu, D. He, P. Liu, F. Ma, Q. Li and N. Feng, *Rare Met. Mater. Eng.*, 2014, **43**, 830–835.
146 S. Ban and J. Hasegawa, *Biomaterials*, 2002, **23**, 2965–2972.
147 S. Ban, K. Matsuo, N. Mizutani and J. Hasegawa, *Dent. Mater. J.*, 1999, **18**, 259–270.
148 A. Yuda, S. Ban and Y. Izumi, *Dent. Mater. J.*, 2005, **24**, 588–595.
149 D. He, P. Liu, X. Liu, F. Ma, X. Chen, W. Li, J. Du, P. Wang and J. Zhao, *J. Alloys Compd.*, 2016, **672**, 336–343.
150 S.-H. Wang, W.-J. Shih, W.-L. Li, M.-H. Hon and M.-C. Wang, *J. Eur. Ceram. Soc.*, 2005, **25**, 3287–3292.
151 M.-C. Wang, W.-J. Shih, K.-M. Chang, S.-H. Wang, W.-L. Li and H.-H. Huang, *J. Non-Cryst. Solids*, 2010, **356**, 1546–1553.
152 X. Lu, Z. Zhao and Y. Leng, *J. Cryst. Growth*, 2005, **284**, 506–516.
153 Y. Parcharoen, P. Kajitvichyanukul, S. Sirivisoot and P. Termsuksawad, *Appl. Surf. Sci.*, 2014, **311**, 54–61.
154 H. Tsuchiya, J. M. Macak, L. Müller, J. Kunze, F. Müller, P. Greil, S. Virtanen and P. Schmuki, *J. Biomed. Mater. Res.*, 2006, **77A**, 534–541.
155 D. Gopi, A. Karthika, M. Sekar, L. Kavitha, R. Pramod and J. Dwivedi, *Mater. Lett.*, 2013, **105**, 216–219.
156 F. S. Utku, E. Seckin, G. Goller, C. Tamerler and M. Urgen, *Ceram. Int.*, 2014, **40**, 15479–15487.
157 D. Lahiri, S. Ghosh and A. Agarwal, *Mater. Sci. Eng., C*, 2012, **32**, 1727–1758.
158 A. Stoch, A. Brożek, S. Błażewicz, W. Jastrzębski, J. Stoch, A. Adamczyk and I. Rój, *J. Mol. Struct.*, 2003, **651–653**, 389–396.
159 M. Li, Q. Liu, Z. Jia, X. Xu, Y. Cheng, Y. Zheng, T. Xi and S. Wei, *Carbon*, 2014, **67**, 185–197.
160 M. Prodana, M. Duta, D. Ionita, D. Bojin, M. S. Stan, A. Dinischiotu and I. Demetrescu, *Ceram. Int.*, 2015, **41**, 6318–6325.
161 Z. Leilei, L. Hejun, L. Kezhi, S. Qiang, F. Qiangang, Z. Yulei and L. Shoujie, *Ceram. Int.*, 2015, **41**, 4930–4935.
162 Q. Zhang, Y. Liu, Y. Zhang, X. Ji, Y. Tan and Q. Liu, *Mater. Lett.*, 2013, **107**, 337–339.
163 L. Huixia, L. Yong, T. Yanni, L. Lanlan, Z. Qing, L. Kun and T. Hanchun, *New J. Chem.*, 2015, **39**, 3865–3874.
164 Y. Zhang, Y. Liu, X. Ji, C. E. Banks and W. Zhang, *Chem. Commun.*, 2011, **47**, 4126.
165 S. Beaufils, T. Rouillon, P. Millet, J. Le Bideau, P. Weiss, J.-P. Chopart and A.-L. Daltin, *Mater. Sci. Eng., C*, 2019, **98**, 333–346.
166 J. Hernández-Montelongo, A. Muñoz-Noval, V. Torres-Costa, R. J. Martín-Palma and M. Manso-Silvan, *Int. J. Electrochem. Sci.*, 2012, **7**, 12.
167 J. Hernandez-Montelongo, D. Gallach, N. Naveas, V. Torres-Costa, A. Climent-Font, J. P. García-Ruiz and M. Manso-Silvan, *Mater. Sci. Eng., C*, 2014, **34**, 245–251.
168 Z. Luo, J. Che, L. Sun, L. Yang, Y. Zu, H. Wang and Y. Zhao, *Eng. Regener.*, 2021, **2**, 257–262.
169 Y. Yu, Q. Wang, C. Wang and L. Shang, *Eng. Regener.*, 2021, **2**, 96–104.
170 A. Balakrishnan, J. Medikonda, P. K. Namboothiri, M. Manik and A. Natarajan, *Eng. Sci.*, 2022, **19**, 5–19.
171 J. Sun, Q. Mu, H. Kimura, V. Murugadoss, M. He, W. Du and C. Hou, *Adv. Compos. Hybrid Mater.*, 2022, **5**, 627–640.
172 D. Rohilla, S. Chaudhary and A. Umar, *Eng. Sci.*, 2021, **16**, 47–70.
173 T. M. David, K. I. Gnanasekar, P. Wilson, P. Sagayaraj and T. Mathews, *ACS Omega*, 2020, **5**, 11352–11360.
174 T. M. David, P. Sagayaraj, P. Wilson, C. Ramesh, N. Murugesan, E. Prabhu, A. S. R. Murthy and S. Annapoorani, *J. Electrochem. Soc.*, 2016, **163**, B15–B18.
175 C. Tian, L. Wang, F. Luan and X. Zhuang, *Talanta*, 2019, **191**, 103–108.
176 X. Huo, P. Liu, J. Zhu, X. Liu and H. Ju, *Biosens. Bioelectron.*, 2016, **85**, 698–706.
177 L. Cai, D. Xu, H. Chen, L. Wang and Y. Zhao, *Eng. Regener.*, 2021, **2**, 109–115.
178 X. Wang, X. Xia, X. Zhang, W. Meng, C. Yuan and M. Guo, *Mater. Sci. Eng., C*, 2017, **80**, 174–179.
179 G. G. Mandayo, F. González, I. Rivas, I. Ayerdi and J. Herrán, *Sens. Actuators, B*, 2006, **118**, 305–310.
180 T. M. David, P. Wilson, C. Ramesh, N. Murugesan and P. Sagayaraj, *Mater. Res. Express*, 2018, **6**, 015006.
181 T. M. David, P. Wilson, R. Mahesh, C. Ramesh and P. Sagayaraj, *Mater. Res. Express*, 2019, **6**, 095065.

182 T. M. David, P. R. Dev, P. Wilson, P. Sagayaraj and T. Mathews, *Electrochem. Sci. Adv.*, 2022, **2**, e202100083.
183 U. Rajaji, R. Arumugam, S.-M. Chen, T.-W. Chen, T.-W. Tseng, S. Chinnapaiyan, S.-Y. Lee and W.-H. Chang, *Int. J. Electrochem. Sci.*, 2018, **13**, 6643–6654.
184 C. Feng, G. Xu, H. Liu, J. Lv, Z. Zheng and Y. Wu, *J. Electrochem. Soc.*, 2014, **161**, B1–B8.
185 Y. Wu, J. Liu, S. Lin, K. Huang, E. Chen, K. Huang and M. Lei, *Eng. Sci.*, 2022, **18**, 105–112.
186 M. Fan, L. Wu, Y. Hu, M. Qu, S. Yang, P. Tang, L. Pan, H. Wang and Y. Bin, *Adv. Compos. Hybrid Mater.*, 2021, **4**, 1039–1047.
187 Y. He, M. Zhou, M. H. H. Mahmoud, X. Lu, G. He, L. Zhang, M. Huang, A. Y. Elnaggar, Q. Lei, H. Liu, C. Liu and I. H. E. Azab, *Adv. Compos. Hybrid Mater.*, 2022, DOI: 10.1007/s42114-022-00525-z.
188 K. H. M. and R. Dilli, *Eng. Sci.*, 2022, **19**, 186–197.
189 D. Kong, Z. M. El-Bahy, H. Algadi, T. Li, S. M. El-Bahy, M. A. Nassan, J. Li, A. A. Faheim, A. Li, C. Xu, M. Huang, D. Cui and H. Wei, *Adv. Compos. Hybrid Mater.*, 2022, DOI: 10.1007/s42114-022-00531-1.
190 Y. Wu, E. Chen, X. Weng, Z. He, G. Chang, X. Pan, J. Liu, K. Huang, K. Huang and M. Lei, *Eng. Sci.*, 2022, **18**, 113–120.
191 M. Cao, D. D. An Sun, H. Li, D. Lou, F. Yang, P. Du, D. Xu and S. Wang, *ES Mater. Manuf.*, 2022, DOI: 10.30919/esmm5f727.
192 R. Kumar, A. Umar, R. Kumar, M. S. Chauhan, G. Kumar and S. Chauhan, *Eng. Sci.*, 2021, **16**, 288–300.
193 S. Mishra, P. Chaudhary, B. C. Yadav, A. Umar, P. Lohia and D. K. Dwivedi, *Eng. Sci.*, 2021, **15**, 138–147.
194 L. Huixia, L. Yong, L. Lanlan, T. Yanni, Z. Qing and L. Kun, *Mater. Sci. Eng., C*, 2016, **59**, 438–444.
195 Q. Zhang, Y. Liu, Y. Zhang, H. Li, Y. Tan, L. Luo, J. Duan, K. Li and C. E. Banks, *Analyst*, 2015, **140**, 5235–5242.
196 L. Luo, Y. Liu, Y. Tan, H. Li, Q. Zhang and K. Li, *J. Cent. South Univ*, 2016, **23**, 18–26.
197 V. N. Narwade, S. R. Anjum, V. Kokol and R. S. Khairnar, *Cellulose*, 2019, **26**, 3325–3337.
198 V. N. Narwade, K. A. Bogle and V. Kokol, *Emergent Mater.*, 2022, **5**(2), 445–454.
199 M. Sun, Z. Li, Y. Gu, S. Wu and X. Wang, *Mater. Res. Express*, 2019, **6**, 106401.
200 Y. Tan, H. Li, Y. Liu, J. Xie, J. He and J. Pan, *RSC Adv.*, 2016, **6**, 76874–76878.
201 A. Mitsionis, T. Vaimakis, C. Trapalis, N. Todorova, D. Bahnemann and R. Dillert, *Appl. Catal., B*, 2011, **106**, 398–404.
202 H. Tanaka, T. Watanabe and M. Chikazawa, *Faraday Trans.*, 1997, **93**, 4377–4381.
203 A. G. Kontos, A. Katsanaki, T. Maggos, V. Likodimos, A. Ghicov, D. Kim, J. Kunze, C. Vasilakos, P. Schmuki and P. Falaras, *Chem. Phys. Lett.*, 2010, **490**, 58–62.
204 S. Taha, S. Begum, V. N. Narwade, D. I. Halge, J. W. Dadge, M. P. Mahabole, R. S. Khairnar and K. A. Bogle, *Mater. Chem. Phys.*, 2020, **240**, 122228.
205 S. R. Anjum, V. N. Narwade, K. A. Bogle and R. S. Khairnar, *Nano-Struct. Nano-Objects*, 2018, **14**, 98–105.
206 S. Taha, S. Begum, V. N. Narwade, D. I. Halge, J. W. Dadge, M. P. Mahabole, R. S. Khairnar and K. A. Bogle, *Appl. Phys. A*, 2021, **127**, 514.
207 S. R. Anjum and R. S. Khairnar, *Sens Imaging*, 2016, **17**, 18.
208 M. Yashima, N. Kubo, K. Omoto, H. Fujimori, K. Fujii and K. Ohoyama, *J. Phys. Chem. C*, 2014, **118**, 5180–5187.
209 S. K. Avinashi, A. Hussain, K. Kumar, B. C. Yadav and C. Gautam, *Oxford Open Mater. Sci.*, 2020, **1**, itab006.
210 A. Noori, F. Ziaie and M. Shafaei, *J. Nanomed. Nanotechnol.*, 2016, **7**(4), DOI: 10.4172/2157-7439.1000389.
211 T. Ishikawa, H. Saito, A. Yasukawa and K. Kandori, *J. Chem. Soc., Faraday Trans.*, 1993, **89**, 3821–3825.
212 M. Nagai, T. Saeki and T. Nishino, *J. Am. Ceram. Soc.*, 1990, **73**, 1456–1460.
213 M. Nagai, T. Nishino and T. Saeki, *Sens. Actuators*, 1988, **15**, 145–151.
214 R. U. Mene, M. P. Mahabole, R. C. Aiyer and R. S. Khairnar, *Open Appl. Phys. J.*, 2010, **3**, 10–16.
215 R. U. Mene, M. P. Mahabole, K. C. Mohite and R. S. Khairnar, *Mater. Res. Bull.*, 2014, **50**, 227–234.
216 M. P. Mahabole, R. U. Mene and R. S. Khairnar, *AML*, 2013, **4**, 46–52.
217 R. U. Mene, M. P. Mahabole, K. C. Mohite and R. S. Khairnar, *J. Alloys Compd.*, 2014, **584**, 487–493.
218 R. U. Mene, M. P. Mahabole and R. S. Khairnar, *Proceedings IMCS 2012*, AMA Service GmbH, Von-Münchhausen-Str. 49, 31515 Wunstorf, Germany, Nürnberg/Nuremberg, Germany, 2012, pp. 1180–1183.
219 R. S. Khairnar, R. U. Mene, S. G. Munde and M. P. Mahabole, *AIP Conference Proceedings*, Bali, (Indonesia), 2011, pp. 189–192.
220 R. S. Khairnar, S. R. Anjum and M. P. Mahabole, *Int. J. Eng. Sci. Innovative Technol.*, 2014, **3**, 9.
221 R. S. Khairnar, S. R. Anjum, V. Kokol and M. P. Mahabole, *Int. J. Mod. Commun. Technol. Res.*, 2014, **2**, 7.
222 M. P. Mahabole, R. C. Aiyer, C. V. Ramakrishna, B. Sreedhar and R. S. Khairnar, *Bull. Mater. Sci.*, 2005, **28**, 535–545.
223 H. Y. Zhao, H. M. Zhou, J. X. Zhang, W. Zheng and Y. F. Zheng, *Biosens. Bioelectron.*, 2009, **25**, 463–468.
224 R. Ma, B. Wang, Y. Liu, J. Li, Q. Zhao, G. Wang, W. Jia and H. Wang, *Sci. China, Ser. B: Chem.*, 2009, **52**, 2013–2019.
225 J. Li, D. Kuang, Y. Feng, F. Zhang and M. Liu, *Microchim. Acta*, 2012, **176**, 73–80.
226 Q. Zhang, C. Chen, Q. Xie and P. Liu, *Microchim. Acta*, 2009, **165**, 223–229.
227 G. Bharath, R. Madhu, S.-M. Chen, V. Veeramani, A. Balamurugan, D. Mangalaraj, C. Viswanathan and N. Ponpandian, *J. Mater. Chem. B*, 2015, **3**, 1360–1370.
228 L. Jia, X. Wei, L. Lv, X. Zhang, X. Duan, Y. Xu, K. Liu and J. Wang, *Electrochim. Acta*, 2018, **280**, 315–322.
229 S. Wang, Y. Lei, Y. Zhang, J. Tang, G. Shen and R. Yu, *Anal. Biochem.*, 2010, **398**, 191–197.
230 L. Lu, L. Zhang, X. Zhang, S. Huan, G. Shen and R. Yu, *Anal. Chim. Acta*, 2010, **665**, 146–151.

231 P. Kanchana, N. Lavanya and C. Sekar, *Mater. Sci. Eng., C*, 2014, **35**, 85–91.
232 P. Kanchana, M. Navaneethan and C. Sekar, *Mater. Sci. Eng., B*, 2017, **226**, 132–140.
233 E. Iyyappan, S. J. Samuel Justin, P. Wilson and A. Palaniappan, *ACS Appl. Nano Mater.*, 2020, **3**, 7761–7773.
234 D. T. M. Thanh, P. T. Nam, N. T. Phuong, L. X. Que, N. V. Anh, T. Hoang and T. D. Lam, *Mater. Sci. Eng., C*, 2013, **33**, 2037–2045.
235 R. Chakraborty, S. Sengupta, P. Saha, K. Das and S. Das, *Mater. Sci. Eng., C*, 2016, **69**, 875–883.
236 M. R. Etminanfar, J. Khalil-Allafi and A. B. Parsa, *J. Alloys Compd.*, 2016, **678**, 549–555.
237 M. Furko, Z. May, V. Havasi, Z. Kónya, A. Grünewald, R. Detsch, A. R. Boccaccini and C. Balázsi, *J. Solid State Electrochem.*, 2018, **22**, 555–566.
238 F. S. Utku, E. Seckin, G. Goller, C. Tamerler and M. Urgen, *Appl. Surf. Sci.*, 2015, **350**, 62–68.
239 N. Aboudzadeh, C. Dehghanian and M. A. Shokrgozar, *Surf. Coat. Technol.*, 2019, **375**, 341–351.
240 F. Olivier, Q. Picard, S. Delpeux-Ouldriane, J. Chancolon, F. Warmont, V. Sarou-Kanian, F. Fayon and S. Bonnamy, *Surf. Coat. Technol.*, 2020, **389**, 125507.
241 J. Xue, A. Farris, Y. Wang, W. Yeh, C. Romany, J. K. Guest, W. L. Grayson, A. S. Hall and T. P. Weihs, *Coatings*, 2020, **10**, 715.
242 J.-M. Jang, T.-E. Park, S.-D. Kim and H.-C. Choe, *J. Nanosci. Nanotechnol.*, 2018, **18**, 2058–2062.
243 J.-M. Jang and H.-C. Choe, *Appl. Surf. Sci.*, 2019, **477**, 271–279.
244 M. Sharma, R. Nagar, V. K. Meena and S. Singh, *RSC Adv.*, 2019, **9**, 11170–11178.
245 B.-O. Taranu, P. Ianasi, S. F. Rus and A. I. Bucur, *Coatings*, 2022, **12**, 288.
246 H.-T. Chen, M.-C. Wang, K.-M. Chang, S.-H. Wang, W.-J. Shih and W.-L. Li, *Metall. Mater. Trans. A*, 2014, **45**, 2260–2269.
247 V. Huynh, N. K. Ngo and T. D. Golden, *Int. J. Biomater.*, 2019, 1–21.
248 Y. Wang, J. Tao, L. Wang, P. He and T. Wang, *Trans. Nonferrous Met. Soc. China*, 2008, **18**, 631–635.
249 L. Chetibi, D. Hamana and S. Achour, *Mater. Chem. Phys.*, 2014, **144**, 301–309.
250 F. Zhang, L.-X. Lin, G.-W. Wang, R. Hu, C.-J. Lin and Y. Chen, *Electrochim. Acta*, 2012, **85**, 152–161.
251 T.-T. Li, L. Ling, M.-C. Lin, Q. Jiang, Q. Lin, J.-H. Lin and C.-W. Lou, *Nanomaterials*, 2019, **9**, 679.
252 S. Sun, Q. Chen and Q. Song, *CrystEngComm*, 2020, **22**, 8243–8250.
253 H. Wang, N. Eliaz and L. W. Hobbs, *Mater. Lett.*, 2011, **65**, 2455–2457.
254 N. N. C. Isa, Y. Mohd and N. Yury, *2012 IEEE Colloquium on Humanities, Science and Engineering (CHUSER)*, IEEE, Kota Kinabalu, Sabah, Malaysia, 2012, pp. 771–775.
255 H. San, J. Hu, Y. Zhang, J. Han and S. Tang, *J. Appl. Electrochem.*, 2019, **49**, 485–501.
256 D. Qiu, L. Yang, Y. Yin and A. Wang, *Surf. Coat. Technol.*, 2011, **205**, 3280–3284.
257 Y. Huang, S. Han, X. Pang, Q. Ding and Y. Yan, *Appl. Surf. Sci.*, 2013, **271**, 299–302.
258 M. Uddin, C. Hall and V. Santos, *Surf. Coat. Technol.*, 2020, **385**, 125363.
259 X. Zhang and M. Z. Yates, *Surf. Coat. Technol.*, 2018, **351**, 60–67.
260 S. Ban and S. Maruno, *J. Biomed. Mater. Res.*, 1998, **42**, 387–395.
261 D. He, P. Wang, P. Liu, X. Liu, F. Ma, W. Li, X. Chen, J. Zhao and H. Ye, *J. Wuhan Univ. Technol., Mater. Sci. Ed.*, 2016, **31**, 461–467.
262 W.-J. Shih, M.-C. Wang, K.-M. Chang, C.-L. Wang, S.-H. Wang, W.-L. Li and H.-H. Huang, *Metall. Mater. Trans. A*, 2010, **41**, 3509–3516.
263 S. R. Anjum and R. S. Khairnar, *SENSORDEVICES 2016: The Seventh International Conference on Sensor Device Technologies and Applications*, 2016, pp. 48–52.
264 R. U. Mene, M. P. Mahabole, R. Sharma and R. S. Khairnar, *Vacuum*, 2011, **86**, 66–71.
265 K. Cui, Y. Song, Q. Guo, F. Xu, Y. Zhang, Y. Shi, L. Wang, H. Hou and Z. Li, *Sens. Actuators, B*, 2011, **160**, 435–440.
266 M. Kumar, H. Dasarathy and C. Riley, *J. Biomed. Mater. Res.*, 1999, **45**, 9.